



TAMPEREEN TEKNILLINEN YLIOPISTO
TAMPERE UNIVERSITY OF TECHNOLOGY

CALEB C. E. STETSON
X-RAY PHOTOELECTRON SPECTROSCOPY FOR CHEMICAL
STATE IMAGING OF SURFACE MICRO- AND NANOSTRUC-
TURES

Master of Science thesis

Examiner: prof. Mika Valden
Examiner and topic approved by the
Faculty Council of the Faculty of
Natural Sciences
on 4th November 2015

ABSTRACT

CALEB STETSON: X-Ray Photoelectron Spectroscopy for Chemical State Imaging of Surface Micro- and Nanostructures

Tampere University of Technology

Master of Science Thesis, 60 pages, 14 Appendix pages

November 2015

Master's Degree Programme in Science and Bioengineering

Major: Nanotechnology

Examiner: Professor Mika Valden

Keywords: Surface Science, XPS, imaging, PEC, IDE, electrodeposition, chemical state imaging

X-Ray Photoelectron Spectroscopy (XPS) is an established surface analysis technique that is unique for its ability to discern the element and chemical state of surface species. This thesis examines copper deposition on an interdigitated microelectrode sample, and focuses upon chemical state imaging of its surface using XPS.

Prior to chemical state imaging measurements, a preliminary objective of this work was to assess the capabilities of the analysis system quantitatively. Measurements of silver foil references were conducted using different apertures, magnifications, and analyzer pass energies. Similarly, a knife-edge sample was measured to quantify the resolution of the analyzer's deflector lens system.

The interdigitated electrode sample was prepared with a thin copper electrodeposited layer. Initial XPS measurement verified the thickness of the deposition layer, and then images were measured of the sample surface.

Initial results provided information regarding the energy resolution, lateral resolution, and analysis spot size for the analyzer. Results exceeded expectations set by technical manuals. Processed images demonstrated the imaging capabilities of the analyzer.

Lastly, conclusions were drawn from these measurements to direct future measurements. Parameter optimization was presented for imaging and line scans. Furthermore, a theoretical technique was devised to detect and quantify surface features whose dimensions are below the resolution limit of the analyzer.

PREFACE

I would like to thank all the members of Surf.Sci. for welcoming me so quickly to the group; it is with sadness that I must say my farewells to Tampere and Finland.

I am grateful to Kimmo Lahtonen and Markku Hannula for their patience and persistence over the past year. I leave appreciative and humble having worked under such brilliant physicists. Special thanks go to Harri Ali-Löytty for teaching me about electro-deposition, synchrotron radiation, and of course, MAX-lab work ethic.

I would also like to extend my most heartfelt thanks and appreciation to Marietta, Yago, Noel, Ida, Georgie, Gaius, Alja, and Santiago for their friendship throughout my time in Finland.

Tampere, 25.11.2015

Caleb C. E. Stetson

CONTENTS

1.	INTRODUCTION	1
2.	IMAGING IN SURFACE SCIENCE	2
2.1	Surface Science Imaging Techniques	2
3.	X-RAY PHOTOELECTRON SPECTROSCOPY	8
3.1	Scientific Origins.....	8
3.2	The Photoelectric Effect.....	8
3.3	Photoemission and Relaxation Processes.....	9
3.4	The Auger Process	10
3.5	Surface Sensitivity of XPS Measurements.....	10
3.6	Interpretation of XPS Spectra	11
4.	SURFACE ANALYSIS SYSTEM	13
4.1	Electrostatic Input Lens System.....	15
4.2	Hemispherical Analyzer	18
4.3	X-Ray Source	20
4.4	Vacuum Pumps	21
4.5	Ion Bombardment Gun.....	24
5.	MATERIALS AND METHODS	25
5.1	Choice of Samples.....	25
5.2	Preparation of Samples.....	25
5.3	Sample Mounting	32
5.4	Sample Loading.....	33
5.5	Sample Transfer within the System	34
5.6	Spectral Measurements	35
5.7	Imaging.....	37
5.8	Line Scan Measurements	38
5.9	Data Processing	38
6.	RESULTS AND DISCUSSION	39
6.1	Studies of the Analyzer	39
6.2	Interdigitated Electrode with Copper Deposition.....	45
6.3	Imaging Parameter Optimization	56
6.4	Line Scan Parameter Optimization	56
6.5	Quantification of Minuscule Surface Features.....	56
7.	CONCLUSIONS.....	57
	REFERENCES.....	58
	APPENDIX A: SAMPLE LOADING PROTOCOL.....	61
	APPENDIX B: SAMPLE CLEANING VIA ION BOMBARDMENT	65
	APPENDIX C: SAMPLE CLEANING VIA ANNEALING	66
	APPENDIX D: COPPER DEPOSITION CALCULATIONS.....	67
	APPENDIX E: OPTIMIZING IMAGING PARAMETERS.....	68

APPENDIX F: OPTIMIZING LINESCAN PARAMETERS70
APPENDIX G: QUANTIFICATION OF MINUSCULE SURFACE FEATURES72

LIST OF SYMBOLS AND ABBREVIATIONS

a	surface area
A	atomic weight
Al	aluminum
Ar	argon
AFM	Atomic Force Microscopy
C	carbon
CAE	Constant Analyzer Energy
Cu	copper
d	distance
δ	charge of species
E	energy
E_b	binding energy
E_k	kinetic energy
E_p	analyzer pass energy
EDS	Energy-Dispersive X-ray Spectroscopy
ESCA	Electron Spectroscopy for Chemical Analysis (ESCA)
F	Faraday's constant
FEAL	Fast Entry Air Lock
FRR	Fixed Retard Ratio
FWHM	Full Width at Half Maximum
h	Planck's constant (6.626×10^{-34} J s)
I	current
IDE	Interdigitated Electrode
I_0	intensity at surface
I_z	intensity at depth z
λ , $IMFP$	Inelastic Mean Free Path
LEED	Low Energy Electron Diffraction
LRPPR	Lateral Resolution: Point-to-Point Ratio
LRPSLR	Lateral Resolution: Pixel Side Length Ratio
m	mass
M	molarity
MCP	secondary electron multiplication device
MFP	Mean Free Path
MSI	Mass Spectrometry Imaging
n	number of electrons
N	nitrogen
ν	frequency
NSOM	Near-field Scanning Optical Microscopy
O	oxygen
PEC	Photoelectrochemical Cell
PEEM	Photoelectron Emission Microscopy
Φ	work function
Pt	platinum
Q	net charge
ρ	density
RR	Retard Ratio

ζ	deposition thickness
SAM	Scanning Auger Microscopy
SEM	Scanning Electron Microscopy
STM	Scanning Tunneling Microscopy
STS	Scanning Tunneling Spectroscopy
t	time
Ta	tantalum
TEM	Transmission Electron Microscopy
θ	take-off angle
Ti	titanium
UHV	Ultra-high Vacuum
V	voltage
XPS	X-ray Photoelectron Spectroscopy
$-z$	depth
Z	atomic number

.

1. INTRODUCTION

Surfaces are of particular interest to materials scientists, as material performance is greatly dependent upon surface chemistry. For example, corrosion, catalysis, and adhesion are all surface-specific phenomena.

X-Ray Photoelectron Spectroscopy (XPS) is an established surface analysis technique that is unique for its ability to discern the element and chemical state of surface species. As advancements were made in analyzer instrumentation, it became possible to restrict the analysis area to a defined area, and thus create images from XPS measurements. Regardless of the system's approach to imaging, they have in common that an image is composed of pixels, each of which comprises a spectrum sampled at its coordinates. Thus, a recorded image contains a vast amount of data that can be processed to elicit the maximum amount of information concerning the sample surface. This thesis will first introduce other surface science imaging techniques in order to put into context the role of XPS for surface imaging.

A main objective of this thesis work is to quantitatively assess the analyzer's capabilities. First, this is carried out by measuring uniform reference samples to quantify the analyzer's energy resolution, which determines to what extent the system is capable of recognizing chemical shifts. Furthermore, the lateral resolution and analysis spot size of the imaging mode must be quantified to evaluate the suitability of future samples for imaging measurements.

Lastly, the analyzer must be employed in the study of an archetypal sample. One of the most pressing issues in the world today is the demand for clean fuels. Much research has been done in the field of photoelectrochemical cells (PECs), which are able to absorb sunlight and convert this energy to fuel by splitting water molecules and releasing its components as oxygen and hydrogen gases. An interdigitated microelectrode sample was chosen in order to experiment with the metal deposition techniques that are common in this field. This sample will be prepared with copper electrodeposition and studied via XPS to evaluate the analyzer's capabilities. The lessons drawn from the results will direct future studies of electrodeposited surfaces.

2. IMAGING IN SURFACE SCIENCE

Imaging techniques are critical to the field of surface science, and allow for quantitative studies to be realized visually. The result facilitates an integrated understanding of the surface.

When viewed from an external perspective, it may seem that the choice of analysis technique is a simple selection based on what information the scientist wishes to acquire. However, there are many more factors which influence the choice of one imaging technique over another.

There are various concerns that determine which analysis technique is most relevant to the sample, including how much information is already known regarding the sample, type of material, crystallinity, conductivity, hardness, and elemental composition.

2.1 Surface Science Imaging Techniques

The following table illustrates many of the imaging techniques with applications in surface science. The techniques may be used, yet are not restricted to use in surface analysis. This table aims to briefly characterize the techniques by identifying the excitation source, analyzed species, contrast visible, type of sample to generally be studied, as well as lateral resolution and sampling depth.

Table 1: Surface Science Imaging Techniques Summarized [1][2][3][4][5][13][14][15]

<i>Technique</i>	<i>Excitation Source</i>	<i>Analyzed Species</i>	<i>Contrast</i>	<i>Samples</i>	<i>Lateral Resolution</i>	<i>Sampling Depth</i>
MSI - Mass Spectrometry Imaging	Ions (primary ion beam)	Ions (secondary ions)	Mass of emitted ions	oxides/carbons biological	5 - 50 μm	12 - 50 μm
NSOM – Near-field Scanning Optical Microscopy	Light	Light	topography	hard surfaces	25 nm	< 5 nm
AFM – Atomic Force Microscopy	Movement	Force	light diffraction at analysis site	hard, non-conductive	10 - 50 nm	0.1 - 1 nm
STM - Scanning Tunneling Microscopy	Voltage Bias (applied at tip)	Electrons (current)	surface response to voltage	semiconductors, metals	0.1 nm	0.01 nm
STS – Scanning Tunneling Spectroscopy			surface density of states	semiconductors, metals	0.1 nm	0.01 nm
LEED - Low Energy Electron Diffraction	Electrons (low energy)	Electrons (Elastically Scattered)	diffraction pattern	crystals	> 100 μm (beam width)	< 10 nm
EDS – Energy-Dispersive X-ray Spectroscopy	Electrons (high energy)	X-rays	atomic number	elements $Z \geq 5$	0.5 μm	< 10 μm
SAM - Scanning Auger Microscopy	Electrons (focused beam)	Electrons (Auger)	Element, chemical state	elements $Z \geq 3$	1 μm	< 4 nm
SEM - Scanning Electron Microscopy		Topography, atomic number,	all types	0.5 - 20 nm	10-100 nm	
TEM - Transmission Electron Microscopy		Bright field, phase, diffraction, E loss	all types	0.05 - 1 nm	sample thickness	
PEEM - Photoelectron Emission Microscopy		X-rays	Element, chemical state	all types	40 μm (<i>this system</i>)	3-10 nm

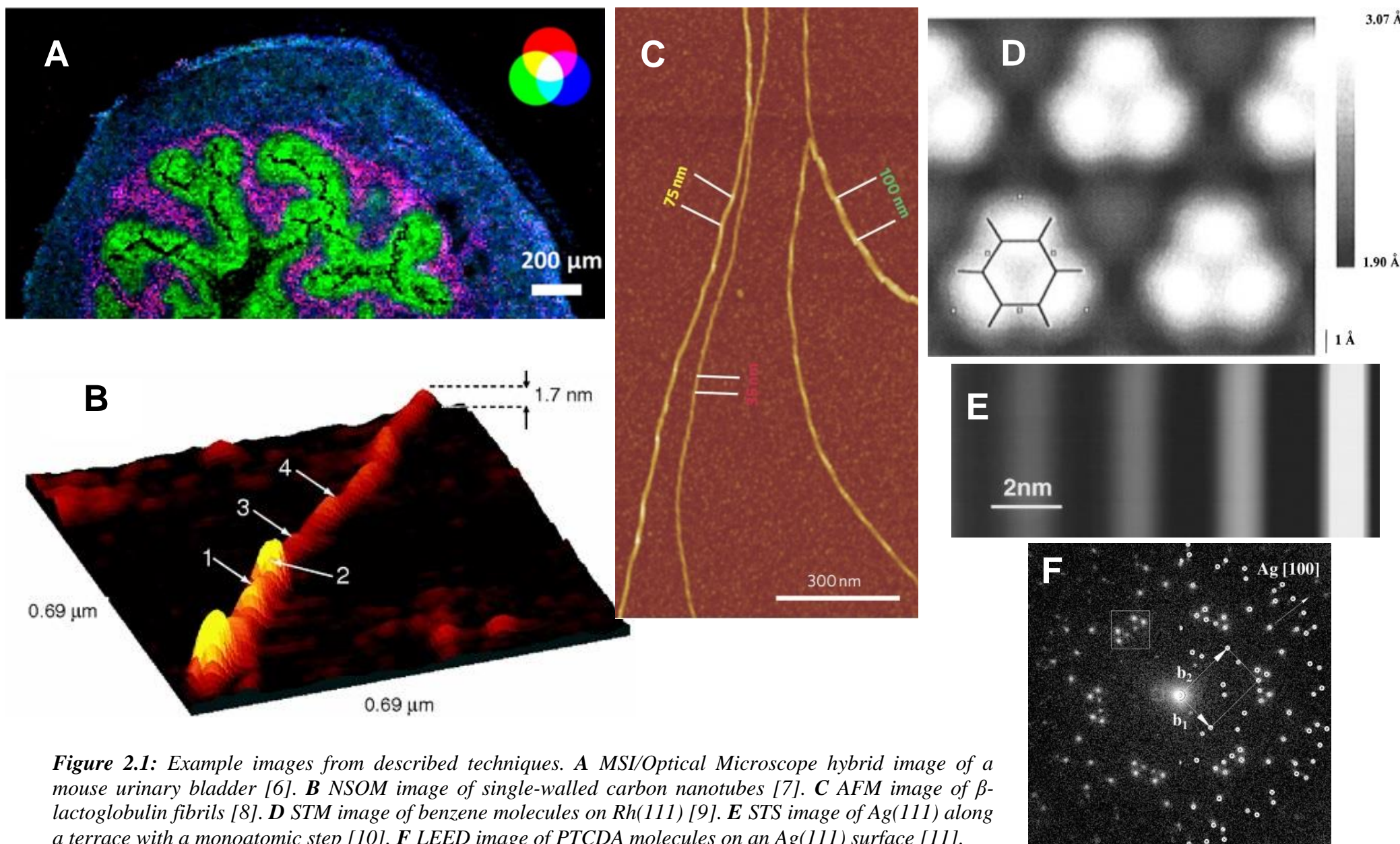


Figure 2.1: Example images from described techniques. **A** MSI/Optical Microscope hybrid image of a mouse urinary bladder [6]. **B** NSOM image of single-walled carbon nanotubes [7]. **C** AFM image of β -lactoglobulin fibrils [8]. **D** STM image of benzene molecules on Rh(111) [9]. **E** STS image of Ag(111) along a terrace with a monoatomic step [10]. **F** LEED image of PTCDA molecules on an Ag(111) surface [11].

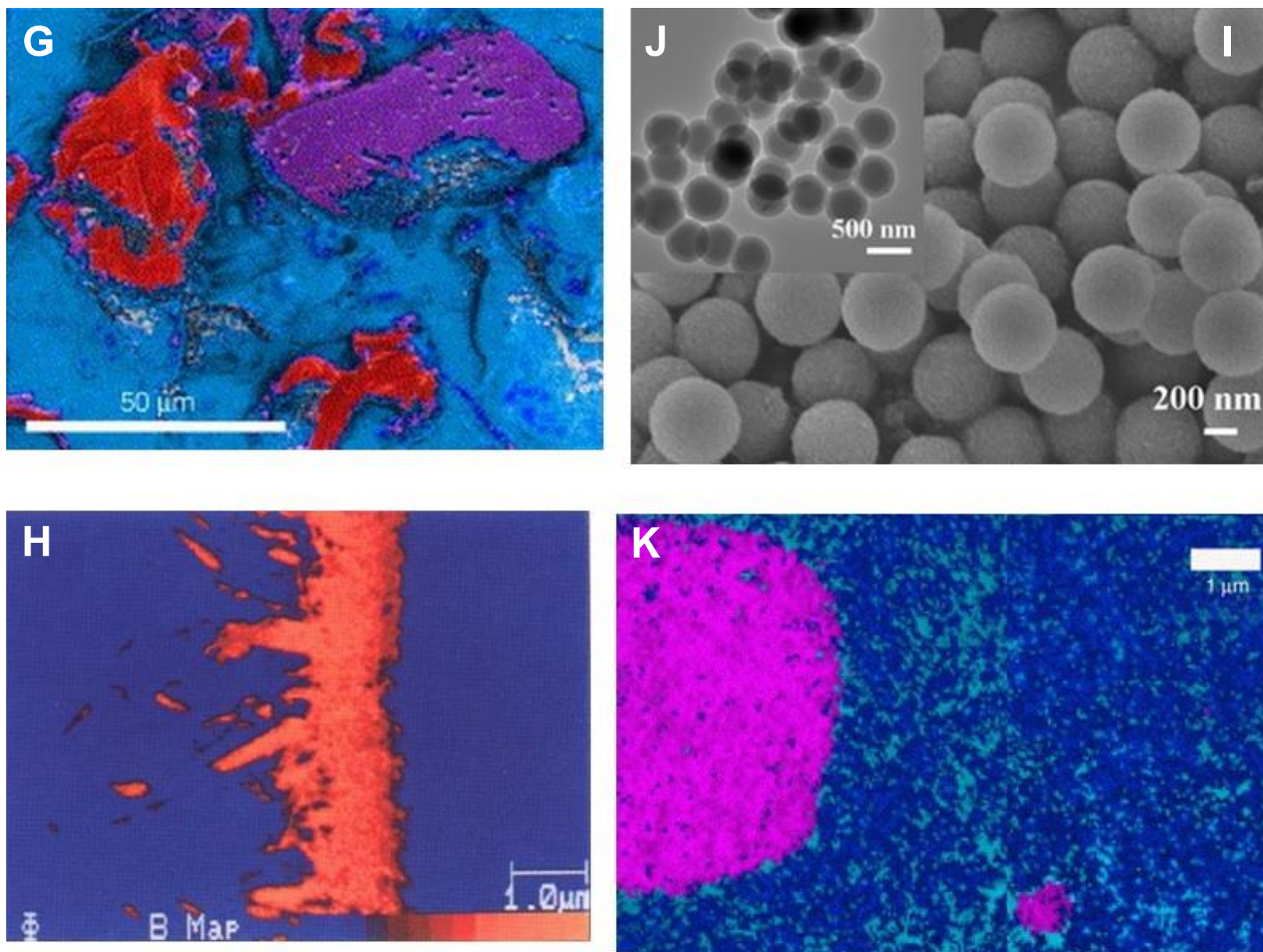


Figure 2.2: Example images from described techniques. **G** EDS/SEM hybrid image of black carbon particles, (red=C, blue=O) [12]. **H** SAM Boron image at a TiB_2 coating interface [13]. **I** SEM image of carbon nanotube covered spheres [17]. **J** TEM image of carbon nanotube covered spheres [17]. **K** PEEM image showing distribution of quartz(magenta) and zircon(blue) [16].

2.1.1 Mass Spectrometry Imaging (MSI) (via Secondary Ion Mass Spectrometry (SIMS))

An ion beam is used to excite secondary ions from the sample, whose mass is studied. The lateral resolution of this technique is in the range of 5-50 μm , and the sampling depth is 5-50 μm . This technique is useful for studying varied materials containing oxides and carbons and widely used studying biological samples [3][4].

2.1.2 Near-field Scanning Optical Microscopy (NSOM)

The microscope is brought within nanometers of the sample surface by a piezoelectric instrument. At these distances in the near field, less than the wavelength of the illuminating light, very high resolution images can be recorded by scanning the NSOM probe across the sample surface [3].

2.1.3 Atomic Force Microscopy (AFM)

Piezoelectric instrumentation allows very small movements of a sharp probe across the sample surface. Feedback prevents the probe from puncturing the surface while keeping it at contact with the surface. The position of the probe is recorded to create a three-dimensional map of the surface [1][3][5].

2.1.4 Scanning Tunneling Microscopy (STM)

As with AFM, STM uses piezoelectric elements to maintain a sharp probe at the surface of the sample. Voltage is applied at the tip, causing electrons to tunnel from the surface to the probe tip. The measured current as the probe is scanned across the surface generates an image indicative of the atomic organization at the surface [1][3][5].

The system discussed in this thesis is capable of measuring STM images.

2.1.5 Scanning Tunneling Spectroscopy (STS)

STS uses the same experimental setup as STM, yet is applied to measure the local density of states and band gap of the surface [1][3][5].

2.1.6 Low-energy Electron Diffraction (LEED)

LEED bombards a crystal with a beam of low-energy electrons; the characteristic pattern of elastically scattered electrons is recorded. From this diffraction pattern, the three dimensional crystal structure of the sample surface can be deduced [5].

The system discussed in this thesis is capable of measuring LEED diffraction patterns.

2.1.7 Energy-dispersive X-ray spectroscopy (EDS)

EDS uses a high energy electron beam to excite core electrons; outer shell electrons drop to fill the core hole, causing an X-ray of a characteristic energy to be emitted. The analyzer measures the energy of these X-rays and can identify elements on a surface. EDS is often paired with SEM [2][3][5].

2.1.8 Scanning Auger Microscopy (SAM)

SAM relies on an emission phenomenon similar to the one which produces X-ray emission in EDS; however, for lighter elements, it's more probable that an Auger electron is produced than X-ray fluorescence. The Auger process is described in depth in the next section [5].

2.1.9 Scanning Electron Microscopy (SEM)

SEM, like SAM, utilizes a focused electron beam to probe a sample. The secondary electrons and backscattered electrons are analyzed and an image is created from the results. SEM is often not as surface sensitive as other techniques, but it is useful when paired with a more surface-sensitive technique in order to create hybrid images [13].

2.1.10 Transmission Electron Microscopy (TEM)

In TEM, a focused electron beam transmits electrons through a very thin sample. This allows for images of the sample to be obtained with very high resolution, but since the electrons are transmitted through the sample, this is not a surface sensitive technique unless it is paired with another technique such as EDS [14].

2.1.11 Photoelectron Emission Microscopy (PEEM)

PEEM is a versatile technique with applications in the study of many types of materials and surfaces. Imaging XPS, which lies within the field of PEEM, will be the subject investigated in this thesis.

3. X-RAY PHOTOELECTRON SPECTROSCOPY

This section will present the physical principles behind X-Ray photoelectron spectroscopy.

3.1 Scientific Origins

X-ray photoelectron spectroscopy (XPS) relies upon several important 19th and 20th century developments in physics. Heinrich Hertz observed the effect of light-matter interaction in 1887, after conducting experiments on the electromagnetic discharge of metals when exposed to ultraviolet radiation. In 1905, Albert Einstein expanded upon Max Planck's research in black-body radiation to formally describe the photoelectric effect. This development in physics made Einstein a Nobel Laureate in Physics in 1921. Pierre Auger continued studies of the photoelectric effect using X-rays in 1923, resulting in the discovery of an additional electron emission process, known as the Auger process. In the subsequent decades, advances in X-ray technology paved the way for Kai Siegbahn's development of XPS as an analytical tool, which published with the title Electron Spectroscopy for Chemical Analysis (ESCA) in 1967. Siegbahn assisted in the development of the first commercial XPS instrument in 1969; he was recognized for his contributions with the Nobel Prize for Physics in 1981 [18][19][20][21].

3.2 The Photoelectric Effect

The photoelectric effect described by Einstein utilized Planck's equation to describe energy quanta for energy photons:

$$E = h\nu \quad (3.1)$$

where E is energy, h is Planck's constant (6.626×10^{-34} J s), and ν is frequency (1/s). Einstein observed that only light of a certain frequency, or photons of a certain energy, could cause photoemission, and thus devised an equation which took this into account:

$$E_k = h\nu - E_b - \phi \quad (3.2)$$

where E_k is photoelectron kinetic energy, $h\nu$ is the photon energy of the X-ray, E_b is the binding energy of the electron when bound to the atom, and Φ is the work function for the material. In summary, an incident X-ray photon can only excite an electron from the material only if the energy $h\nu$ is greater than the E_b , with the excess energy being converted to the E_k of the photoelectron. The electron density as a function of binding ener-

gy is characteristic for each element, which forms the basis of mapping spectra for the elements using a monochromatic source. Furthermore, the binding energy can vary slightly based on the strength or weakness of atom's bonding, causing a chemical shift in the measured peak. This allows XPS to recognize the chemical states of elements being measured [20].

3.3 Photoemission and Relaxation Processes

The photoemission process can be described by the following diagram.

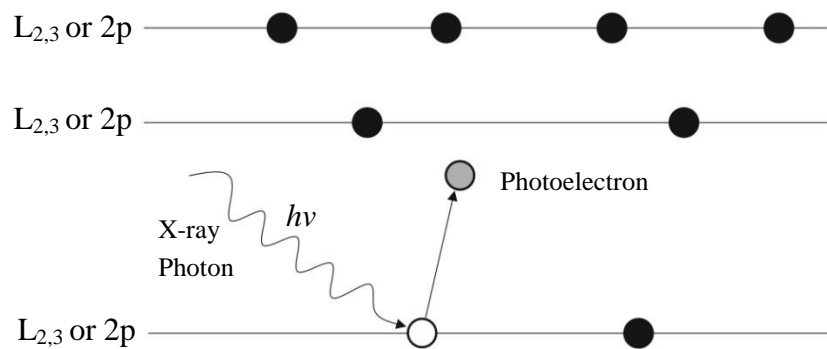


Figure 3.1: Photoelectron emission process for a model atom. An X-ray photon arrives to the atom, ejecting a photoelectron. Adapted from [22].

As shown in the previous figure, an X-ray photon strikes an inner electron, ejecting it from the shell. This photoelectron escapes the electron, leaving a core hole in the atom. With the core hole, the atom is in an excited state, and must undergo a relaxation process to reach its final state.

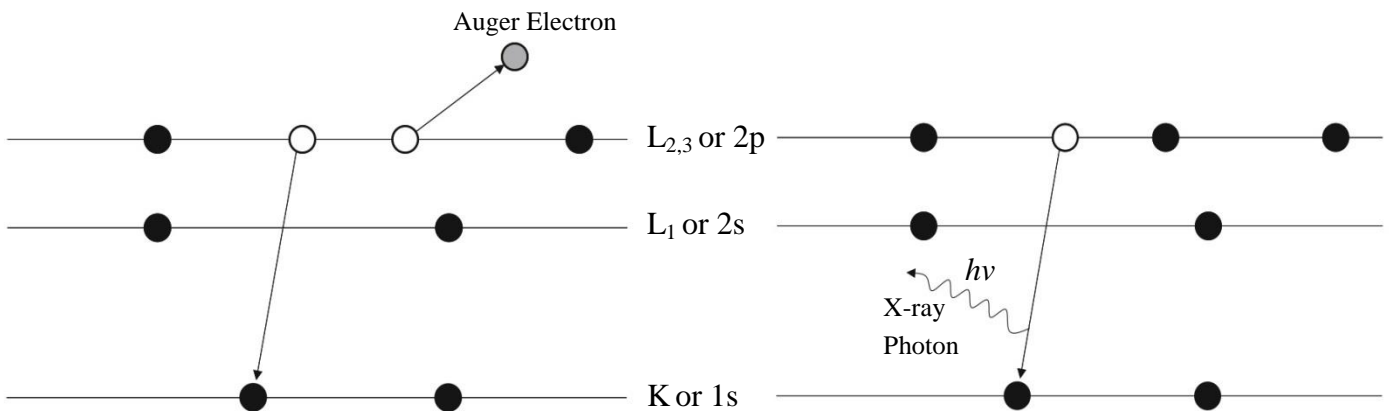


Figure 3.2: Relaxation process for a model atom following photoelectron emission. Two outcomes are possible: either an Auger electron is emitted, or a fluorescent X-ray photon is emitted. Adapted from [22].

The figure above presents the two relaxation processes available to the atom once a core hole has formed. With higher atomic number elements, a greater energy difference between the core hole and the outer shell (which loses an electron to fill the hole) exists. As a result of this, Auger electrons are more common than X-ray fluorescence for lower atomic number elements.

3.4 The Auger Process

The Auger process is unique because the energies of the Auger electrons emitted depend on the internal conditions of the atom; thus, their energies are constant regardless of the energy of the photon source. The Koopman binding energies provide a crude estimate for the kinetic energies of Auger electrons [20]:

$$E_k = E_{initial} - E_{final} \approx E_{b\ initial} - E_{b\ final1} - E_{b\ final2} \quad (3.3)$$

where E_k is the initial E_b minus the final E_b (s). Auger Electron Spectroscopy (AES) is not the focus of this thesis; however, Auger peaks appear in XPS spectra and thus must be identified to avoid misinterpretation.

3.5 Surface Sensitivity of XPS Measurements

Surface science requires that analytical methods are sensitive to the surface layer of the material. Photoelectrons are a useful species to study, since they incur energy losses as they travel through a medium, limiting the depth from which electrons can emerge from an illuminated sample.

A useful term that quantifies this phenomenon is the Inelastic Mean Free Path (IMFP). If inelastic scattering is the only factor which attenuates photoelectrons, IMFP obeys the Beer-Lambert law [21]:

$$I_z = I_0 e^{-z/\lambda \sin\theta} \quad (3.4)$$

Where I_z is the intensity originating from the atoms at depth z , I_0 is the intensity originating from atoms on the surface, and θ is the take-off angle with respect to the surface plane. In this equation, λ denotes the IMFP.

IMFP has been measured experimentally for many materials, and the results show an important trend between electron energy and IMFP. The result of these measurements has been called the universal curve, which is shown below.

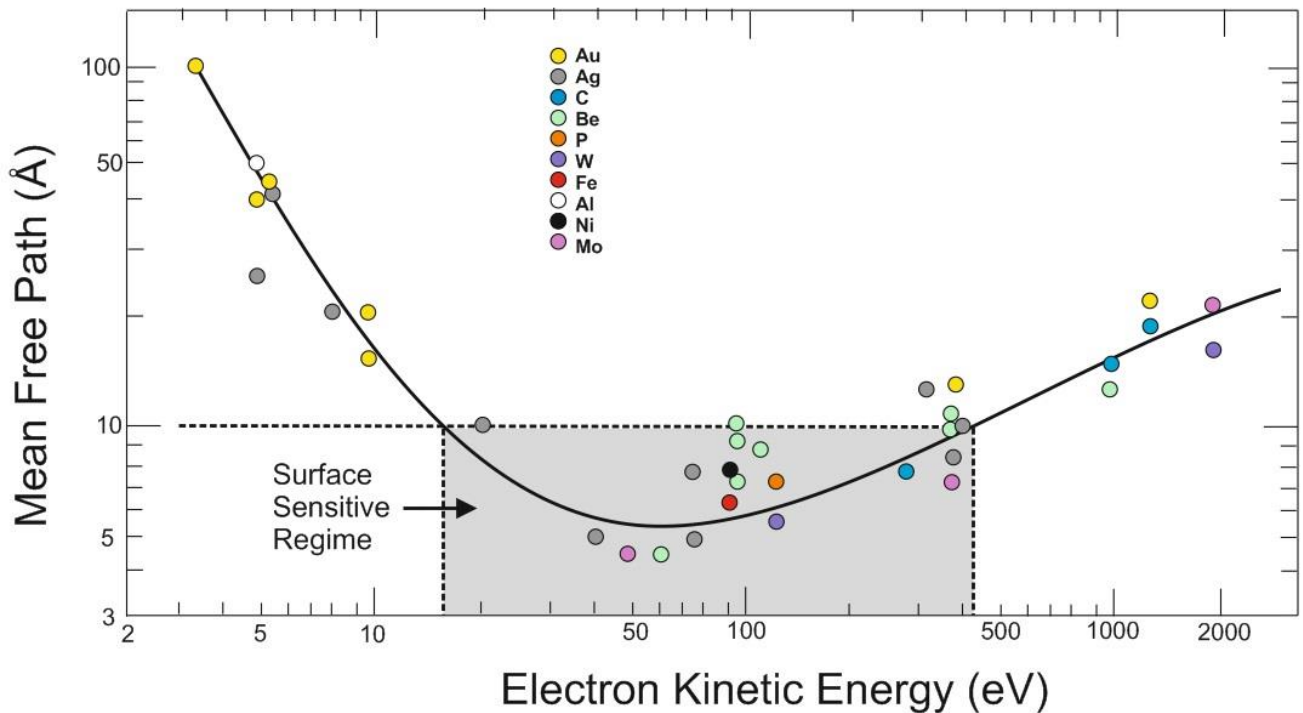


Figure 3.3: Universal electron curve, displaying the mean free path as it varies according to electron kinetic energy. The surface sensitive energy regime is labeled on the curve, indicating the regime for which mean free path is lowest for photoelectrons. Adapted from [20].

As seen in the figure, the IMFP increases rapidly for very small kinetic energies, finds a minimum at around 50 eV, then increases for higher energies. The energy regime for which the IMFP is less than 10 Ångstroms (1 nm) can be called the surface sensitive energy regime, as labeled in the figure.

3.6 Interpretation of XPS Spectra

Now that the theory behind XPS has been presented, the interpretation of spectral results can be discussed. A typical survey spectrum of Cu(100) will be discussed, where the source is $\text{Al}_{K\alpha}$ X-ray radiation. Normal transitions, as well as Auger transitions, and satellite peaks are present on the spectrum.

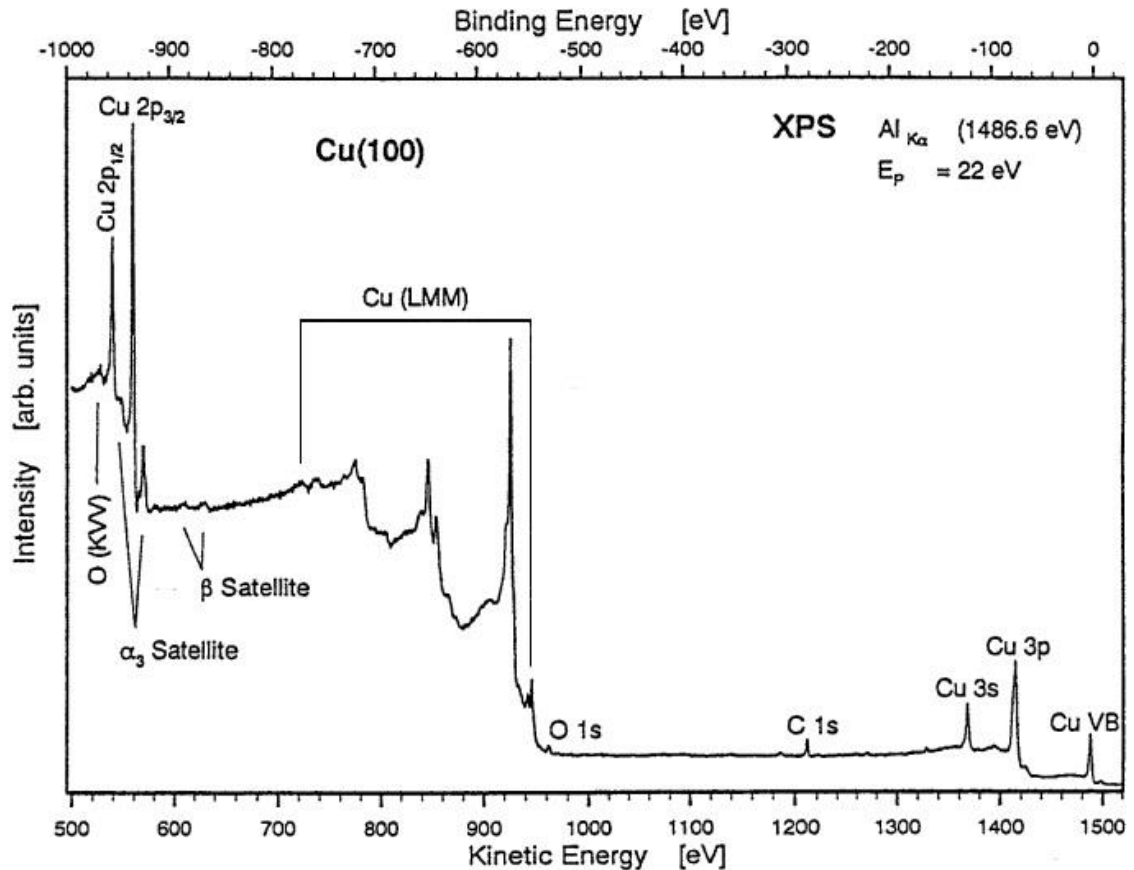


Figure 3.4: XPS spectrum of a Cu(100) surface, showing features typical in XPS spectra [20].

The energy scale of the spectrum is presented in terms of the received E_k of electrons. Moving from right to left, or from lower binding energy to higher binding energy, the first signal is the valence band. This is followed by the Cu 3p line and the Cu 3s line. After these lines, C 1s and O 1s lines appear, representing some surface contamination, which is common even in a sample that has been cleaned and kept in an ultrahigh vacuum (UHV). Auger lines (Cu (LMM)) follow on the spectrum. β and α_3 satellite peaks appear next, indicative of a non-monochromatic X-ray spectrum; they represent the same high intensity peaks from the spectra, but with photoelectrons excited by X-ray photons with energies other than the 1486.6 eV $Al_{K\alpha}$ X-ray line. Next on the spectrum are the Cu $2p_{3/2}$ and Cu $2p_{1/2}$ lines. Unlike the Cu 3p and Cu 3s lines, spin-orbit splitting is easily observed for this transition, which separates the lines by approximately 20 eV. Splitting occurs for all subshells that have an angular momentum greater than zero. Thus, only lines caused by the excitation of s electrons do not result in splitting. Lastly, the Auger O KVV line appears, also indicative of oxidation on the surface of the sample. However, given the low intensity of the O 1s peak, the Auger lines probably do not have enough intensity to be easily distinguished from spectral noise. When analyzing XPS spectra, software allows features to be fitted and quantified to make quantitative conclusions regarding the sample [20].

4. SURFACE ANALYSIS SYSTEM

The surface analysis system will be described in this section. Analyzer components, X-ray source, pumps to maintain the vacuum and the sputtering gun used for sample cleaning will be presented.

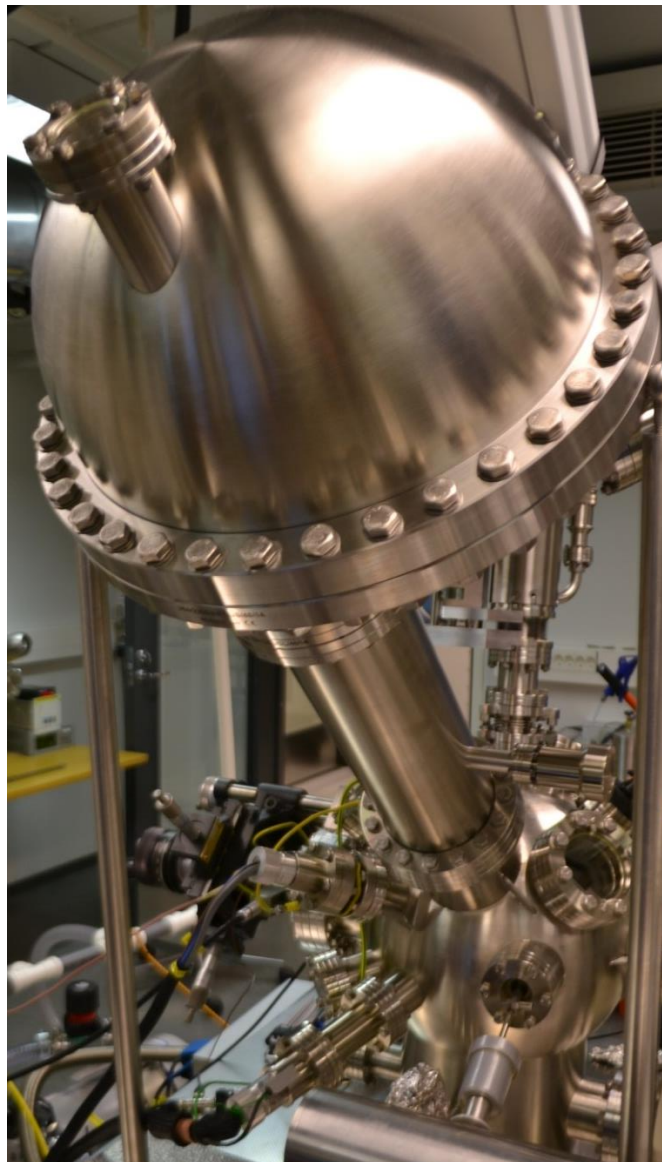


Figure 4.1: Energy analyzer, mounted above the system's analysis chamber

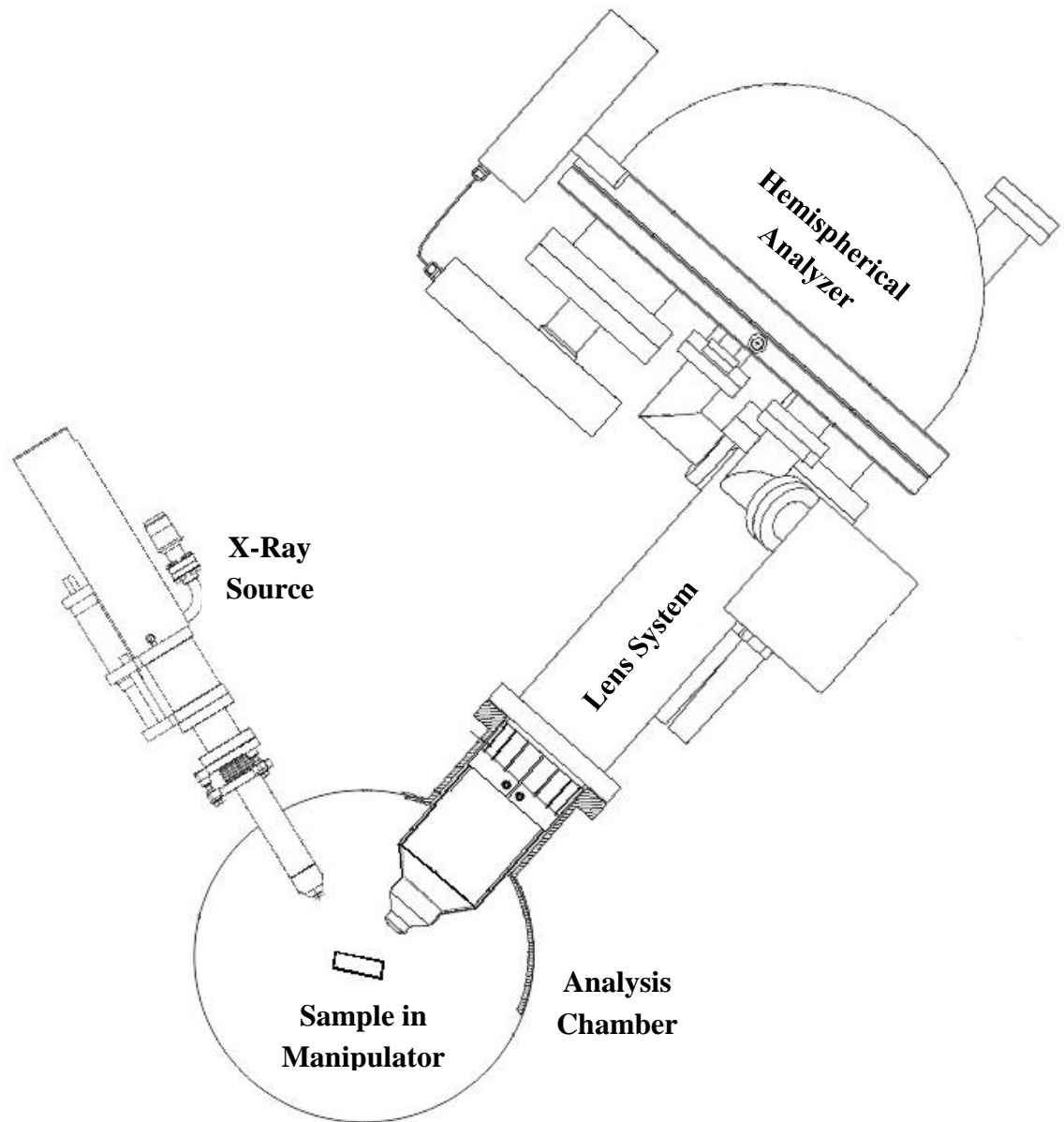


Figure 3.2: Diagram showing the orientation of the X-Ray source, analysis chamber, lens system, and hemispherical analyzer as they are mounted to the analysis chamber. Figure was created from separate schematics [23][24].

The figure above depicts how the different elements are oriented in the analysis system. The basic premise of such a system requires that a sample can be moved to an Ultra-high Vacuum (UHV) analysis chamber, where an excitation source can be directed at the sample surface. The radiation produced by the source excites electrons from the surface of the sample, which travel through the lens system to the hemispherical analyzer, which then counts the electrons reaching the detector.

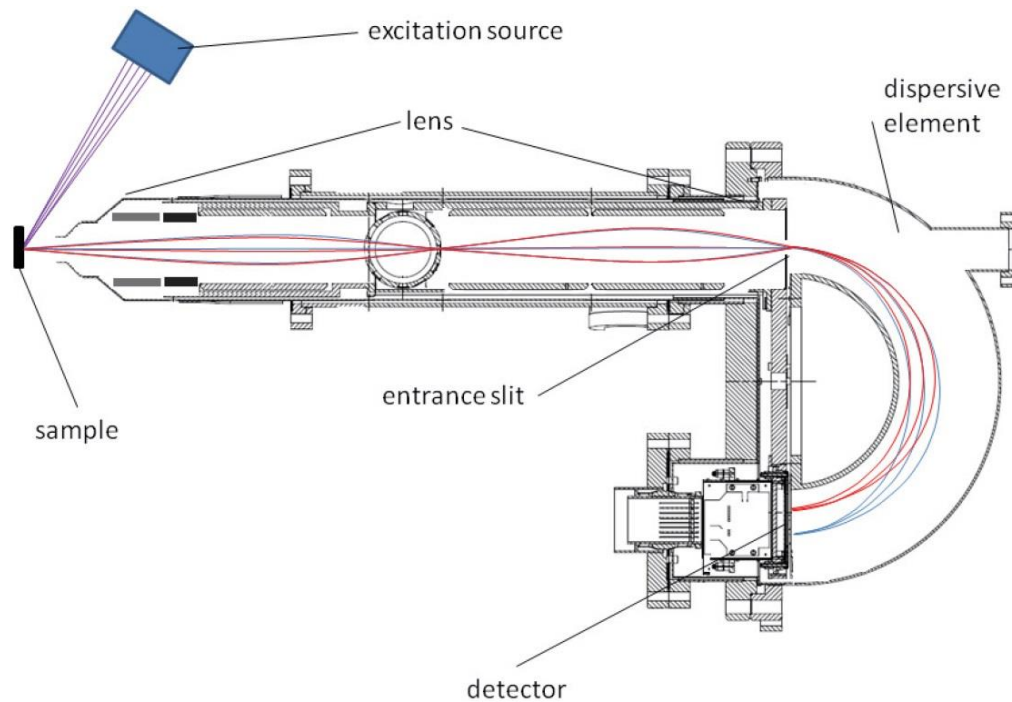


Figure 4.3: Diagram showing the path of electrons excited from the sample by the X-Ray source [23].

The figure above illustrates the path of electrons as they are excited from the sample surface. After being excited from the sample, the electrons are focused in the transfer lens to pass through the lens aperture. They then enter the retard lens where their kinetic energy is changed to match the pass energy of the analyzer, after which they pass through the analyzer entrance slit. The dispersive element ensures that only electrons with a kinetic energy within a limited interval (known as the band pass) are able to reach the electron detector. Thus, slower electrons (lower E_k , depicted in red in the figure) arrive to the detector at locations closer to the hemisphere's center, while faster electrons (higher E_k , depicted in blue in the figure) arrive to the outside of the detector. Thus, the band pass is the energy difference between the most energetic and least energetic electrons that are counted at the electron detector.

4.1 Electrostatic Input Lens System

The electrostatic input lens system includes a multi-element electrostatic lens with a working distance of 30 mm. Additionally, the system contains an in-lens deflector to scan the focal point of the lens across the sample and an in-lens aperture to define the sample analysis area. First, electrons pass through the Transfer Lens then pass to the Retard Lens before entering the energy analyzer [23].

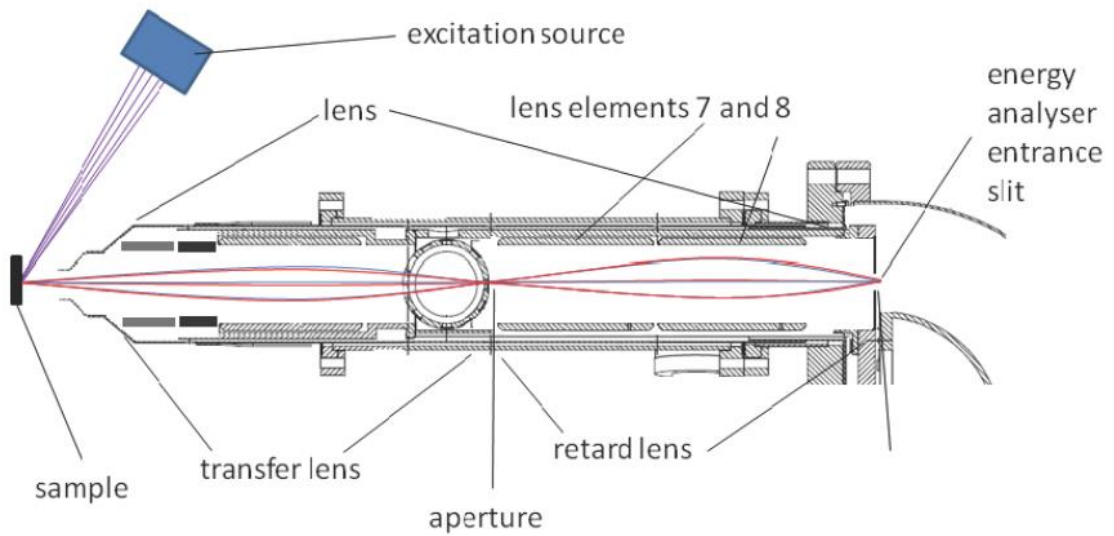


Figure 4.4: Electrostatic Input Lens System Schematic [23]

4.1.1 Transfer Lens (First Lens Section)

The transfer lens has four main functions: transferring electrons without changing their energy (i.e. behaving as an Einzel lens), magnification, selection of analysis area and acceptance angle for electrons, and scanning the analysis area across the sample.

The Einzel lens operation is achieved by maintaining constant magnification throughout the entire energy range, with voltages proportional to the kinetic energy of the photoelectron. The voltage supply determines the magnification which occurs in the transfer lens, and operates the in High, Medium, or Low magnification modes. The deflector assembly contained within the transfer lens also allows the analysis area to be moved across the sample, which permits imaging of a sample surface. This is achieved by applying specific voltages to the deflector electrodes, depending on the kinetic energy of the studied transition, according to the equations [23]:

$$V_x = fact(mag) \times d_x \times E_k, \quad V_y = fact(mag) \times d_y \times E_k$$

where $fact(mag)$ is a constant depending on the magnification setting, V_x/V_y are voltages applied, E_k is kinetic energy, and d_x/d_y are distances moved for the analysis (4.1)(4.2)

The acceptance angle determines the angular spread of electrons originating from the center of the analysis chamber which are able to pass through the lens. The chosen aperture and the magnification settings determine the analysis area. When magnification is lowered, the analysis area is increased and the acceptance angle decreases.

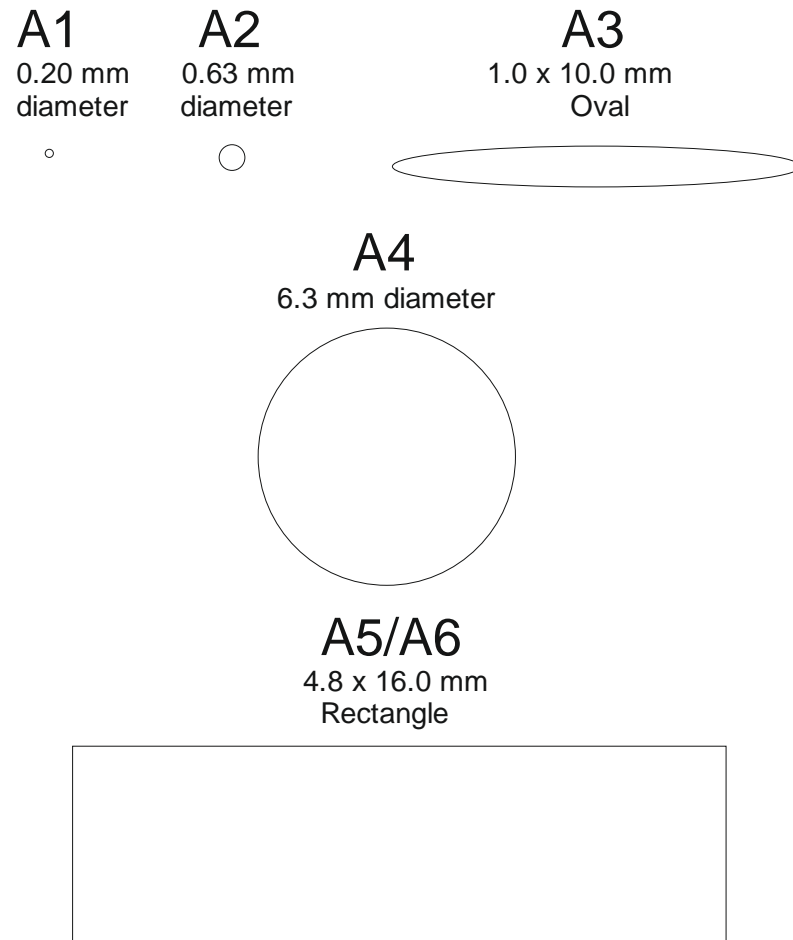


Figure 4.5: Lens Apertures drawn to relative scale.

Table 4.1: Full width at Half Maximum (FWHM) of analysis area, acceptance half angles for apertures and magnifications. [23].

Aperture	FWHM of analysis area (mm)			Acceptance Half Angle (°)		
	High	Medium	Low	High	Medium	Low
A1	0.066	0.106	0.189	±3.8	±2.5	±1.1
A2	0.198	0.278	0.657	±7.0	±4.6	±1.6
A3	0.311	0.405		±3.1	±2.7	±1.2
	3.22*	4.83				
A4	1.93	2.78	6.86	±9.4	±6.6	±2.5
A5	1.54			±9.6	±6.7	±2.5
	4.09*					
A6	1.23			±9.8	±9.3	±1.9
	4.66*					

*in non-dispersive direction

4.1.2 Retard Lens (Second Lens Section)

The retard lens has the role of transferring an image from the aperture plane to the plane which contains the entrance slit of the energy analyzer, changing the E_k of the electrons to match the E_p of the analyzer. The term Retard Ratio (RR) is the ratio between these energies, represented by the equation:

$$RR = E_k/E_p \quad (4.3)$$

The analyzer can operate under Constant Analyzer Energy (CAE) mode, or Fixed Retard Ratio (FRR) mode. In CAE mode the analyzer's pass energy (E_p) is constant for the measurement, while in FRR mode the E_p is varied according to the energy of the E_k of the measured electron.

4.2 Hemispherical Analyzer

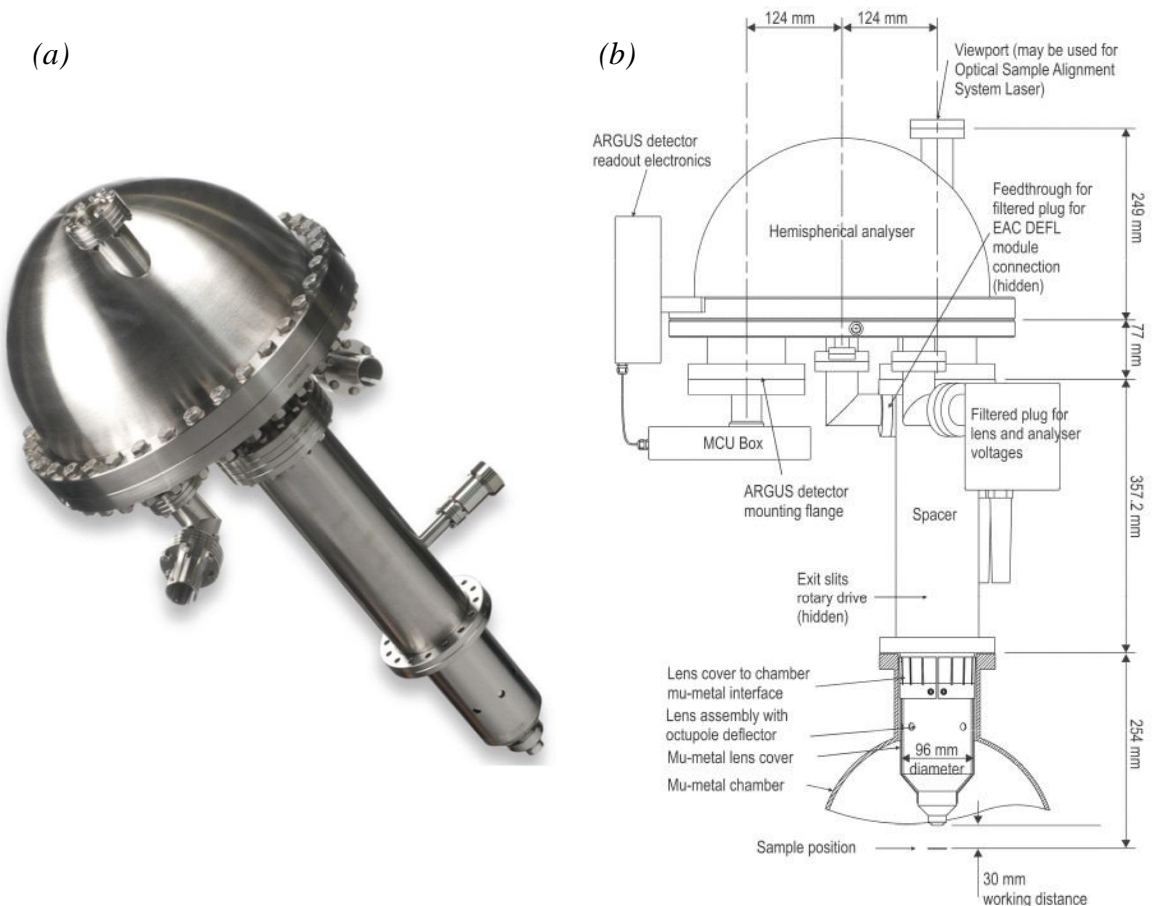


Figure 4.6: (a) Photograph and (b) schematic depicting the Omicron NanoTechnology ARGUS Spectrometer [23].

The Argus Spectrometer contains a 124 mm mean radius electrostatic hemispherical dispersive energy analyzer formed from two concentric hemispheres. The outer hemi-

sphere has a 146 mm radius, while the inner hemisphere has a 102 mm radius, which focuses electrons in both angular directions from the entrance slit onto the exit plane. The orientation of the hemispheres is visible in Figure 3. The space between the hemispheres is called the analyzer gap, for which an applied gap voltage creates an electric field. This gap voltage is proportional to E_p [23].

After passing through the slit, some electrons are able to pass through the gap following an elliptical trajectory without striking the hemispheres. This is possible for electrons of kinetic energies between $0.93E_p$ and $1.07E_p$ if they enter the slit with an appropriate starting angle. This behavior can be summarized by the following equation, which relates the E_k of the range of electrons detected to the E_k of electrons reaching the center of the detector [23]:

$$E_k = E_{k \text{ center}} \pm 0.07E_p \quad (4.4)$$

Thus, larger pass energies increase the electron count rate at the expense of spectral resolution.

The Argus detector has 128 parallel energy channels, each containing a secondary electron multiplication device (MCP) which is followed by an electronics amplifier, discriminator, and counter. The detector collects a fraction of the electrons arriving at the detector, since to be counted the electron must trigger an electron avalanche. The probability for this analyzer generally lies between 60% and 90% [23].

The snapshot mode relies on the fact that faster electrons arrive to the outer edge of the detector while slower electrons arrive to the inner edge of the detector (as depicted in figure 3); this property defines an energy window of 128 discrete energies, determined by the E_p used during measurement. Snapshot mode is used for imaging, whereby a longer dwell time for the energy window is substituted for shorter dwell times for defined energy steps through a set spectral energy range. Analyzer operation is controlled via MATRIX software, whose measurement results are viewed and exported using Vernissage software.

4.3 X-Ray Source

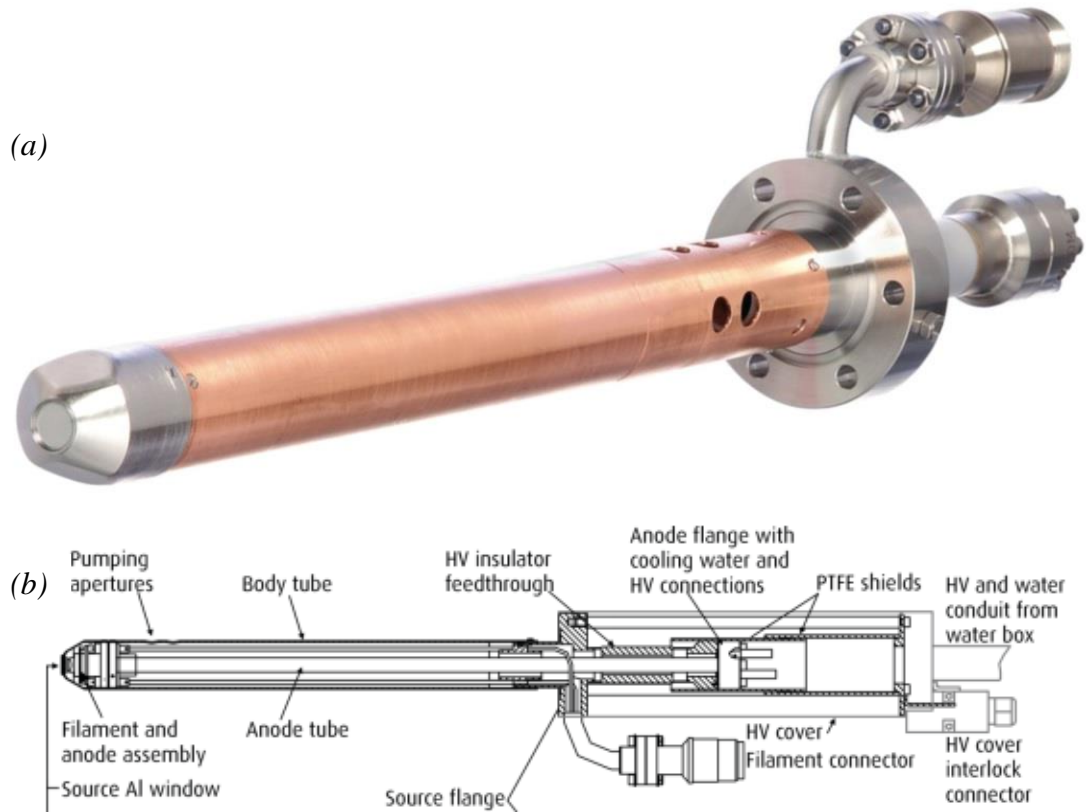


Figure 4.7: (a) Photograph and (b) schematic depicting the Oxford Instruments® DAR400 X-Ray Source [24].

The X-ray source is specifically designed for XPS, and contains Mg $K\alpha$ (1253.6 eV) and Al $K\alpha$ (1486.6 eV) anodes. The operational parameters and anode are selected via X-ray 558 Source Control software [24].

During operation, a heated filament produces electrons which bombard the surface anode (Mg or Al) at high positive potential, which causes characteristic X-ray emission lines to be produced from the anode. Water cooling prevents the anode materials from evaporating [22][24].

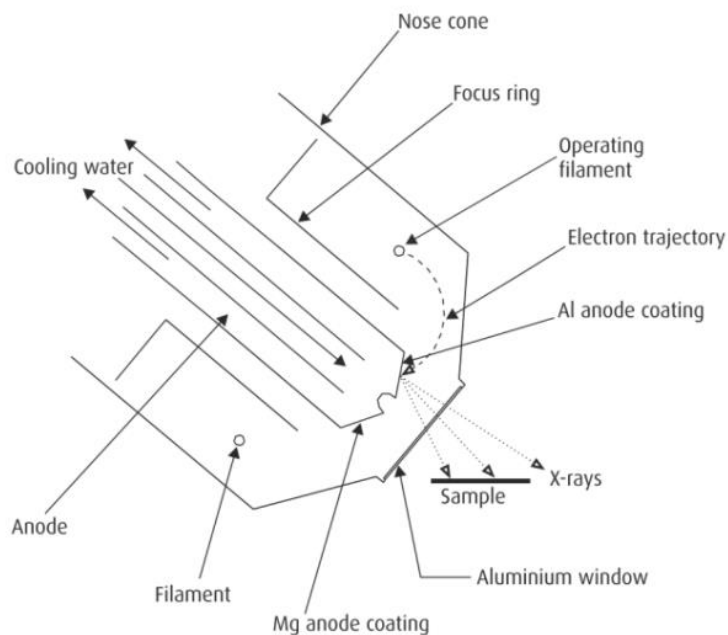


Figure 4.8: X-ray source operation [24].

The source can be mechanically positioned, such that the source can be brought as close to the sample as possible to maximize X-ray flux [24].

4.4 Vacuum Pumps

An ultra-high vacuum (UHV) can be characterized as pressure at or below 10^{-9} mbar. XPS measurements generally require UHV conditions to prevent surface contamination; oxides and other impurities both change the chemical character of the surface and attenuate measured XPS peaks. Moreover, UHV guarantees that the Mean Free Path (MFP) of molecules in the system is high enough that gas molecules only collide with the sample wall, preventing surface adsorption during measurement. Similarly, a high MFP also ensures that the incidence of photoelectron collision with gas molecules very low. Such collisions would prevent the photoelectron from reaching the analyzer, or alter its energy inducing signal noise [5].

Several types of pumps are required to maintain the UHV. These include displacement pumps (in this system, scroll pumps), mass transfer pumps (in this system, turbomolecular pumps), and entrapment pumps (in this system, ion pumps) [5].

Maintaining UHV in a surface analysis system requires frequent monitoring of pressures and occasional maintenance and replacement of vacuum pumps.

4.4.1 Scroll Pumps

The class of vacuum pump suitable for use with atmospheric pressures is the displacement pump. In this system, scroll pumps are used. Since they are capable of moving the highest quantities of gas, they are required on the back end of turbo-molecular pumps to minimize the pressure at the turbo-molecular pump inlet. This type of pump is known as a backing pump, because it is located at the exhaust of the mass transfer pump. In summary, these pumps are used to bring system pressure down to the operational pressures of the next class of pumps [5].



Figure 4.9: Scroll Pump Operation [28]

Scroll pumps include a fixed scroll and an orbiting scroll; the orbiting scroll is controlled by a motor. When operating, crescent shaped volumes in the pump are compressed by the movement of the orbiting scroll, and drawn to the center of the fixed scroll; this compressed gas is exhausted from the pump, which forms the mechanism of the vacuum pumping within a scroll pump. The performance of scroll pumps includes a pressure range from 1000 mbar (~ 1 atmosphere) down to below 0.1 mbar [5][25].

4.4.2 Turbo-molecular Pumps

The next class in vacuum pumps is the mass transfer pump. In this system, turbo-molecular pumps represent this class. Turbo-molecular pumps have a much lower throughput when compared to scroll pumps, and thus require a backing pump to function within the system [5].

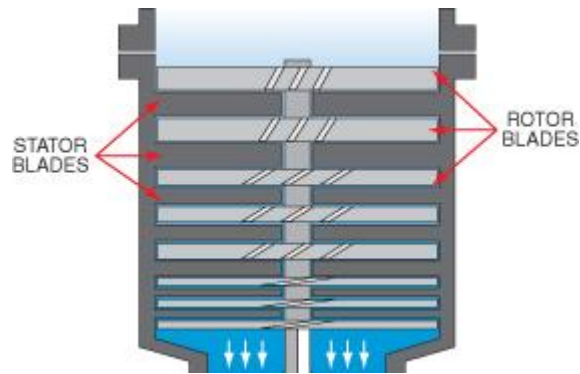


Figure 4.10: Turbo-Molecular Pump Operation [28]

The turbo-molecular pump contains a high performance 3-phase electric motor which operates a turbine at high speeds (up to 80,000 rpm). It contains multiple bladed stages of varying blade angles, rotating counter-clockwise when viewed from the high vacuum end. These pumps function mechanically similarly to jet engines and are especially well suited for pumping noble gases, heavier molecules, and nitrogen. Turbo-molecular pumps require a cooling fan to prevent overheating [5][26].

4.4.3 Ion Pumps

The final class in vacuum pumps is the entrapment pump. In this system, ion pumps are used. Ion pumps are capable of reaching UHV on the order of 10^{-11} mbar through ionization of gases and utilization of Ti sublimation [5].

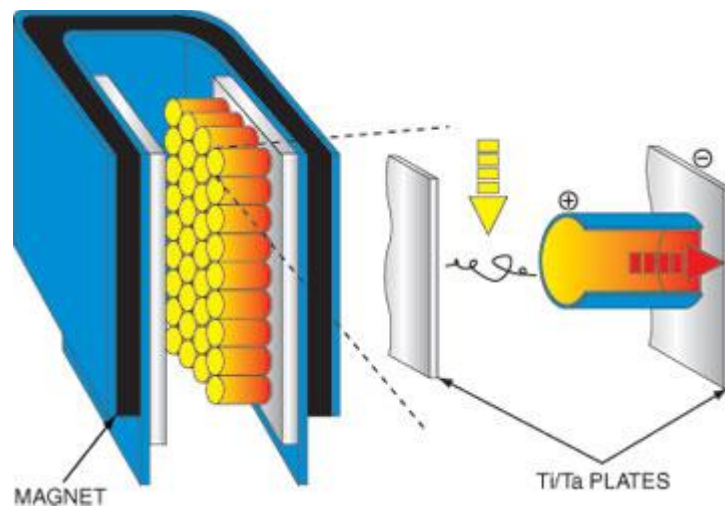


Figure 4.11: Ion Pump Operation [28]

A strong magnetic field within the ion pump is combined with high voltage to break molecular bonds and strip electrons from the atoms, resulting in positively charged ions. The Ti filaments within the ion pump are periodically sublimated to coat the interior with Ti, a substance that is especially reactive towards these positively charged ions. This irreversible absorption of ions is called gettering. The distinct method of lowering pressures in the ion pump is not coordinated through backpumping, so ion pumps can be connected directly to the analysis chamber, isolated from turbo-molecular pumps and scroll pumps as long as the pressure is already in the UHV realm. Operating below UHV pressures dramatically reduces the lifetime of the ion pump, as their lifetime is linearly increased by decreased operational pressure; an ion pump may operate for 50,000 hours at 1×10^{-6} mbar but many years at 1×10^{-9} mbar. Ion pumps, unlike turbo-molecular pumps, are better suited for pumping lighter molecules, since they actively attract and entrap the molecules rather than waiting for them to drift into the pump. Thus, these two types of vacuum pump form a natural combination for achieving and maintaining UHV [5][27].

4.5 Ion Bombardment Gun

The surface analysis system also includes an ion bombardment gun contained within a separate preparation chamber for cleaning and depth profiling of samples. The gun contains an electron impact ionization source and an electrostatic lens system in order to

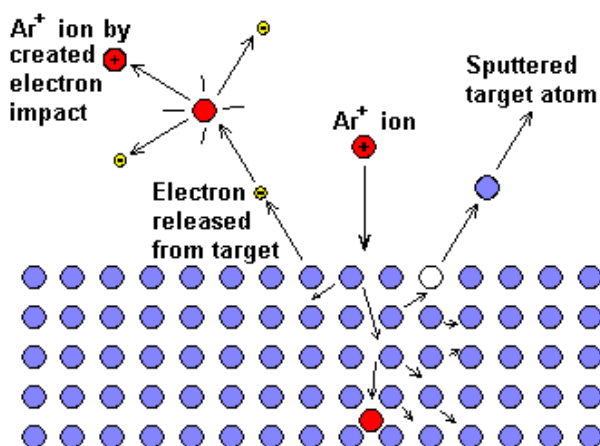


Figure 4.12: Sputtering to clean a surface with Argon [30]

accelerate, focus, and deflect the ion beam. Electrons emitted from a filament are accelerated into an inert gas (in this case Argon), producing ions which can then be accelerated into the focusing lens. This focused ion beam strikes the surface of a sample and the collisions between atoms eject atoms from the surface of the sample, thus sputtering, or cleaning the surface. Such a cleaning technique is valuable for removing surface oxides and carbons [29].

5. MATERIALS AND METHODS

This section will describe analyzed samples and the utilized preparation techniques.

5.1 Choice of Samples

There are four categories of samples that were studied: uniform metallic references to study the analyzer's spectra with varied parameters (silver, copper, and tantalum), samples to quantify spatial resolution of the analyzer (tantalum knife edge), references to plan preparation of the final case study (platinum foil), and the case study itself to employ the analyzer's imaging mode (Interdigitated Electrode).

5.2 Preparation of Samples

Here the preparation process for each sample will be described.

5.2.1 Preparation Techniques

The following sample cleaning techniques were used in the preparation of multiple samples.

Sample Cleaning via Ion Sputtering

When uniform samples contain surface contamination and a clean surface is critical, ion sputtering is used. Clean Ar gas is pumped to the ion bombardment gun where it is ionized. The Ar atoms are accelerated to bombard the sample. This removes surface oxides and other contaminants, yet leaves the surface pitted with some Ar contamination. In order to smooth the pitted surface, an annealing cycle often follows a sputtering cycle. More specific details regarding ion bombardment protocol are available in the appendices (Appendix B).

Sample Cleaning via Annealing

Annealing can be achieved at low temperatures using radiative heating, and at high temperatures using an electron beam. More specific details regarding annealing protocol are available in the appendices (Appendix C).

5.2.2 Metal Foil Samples

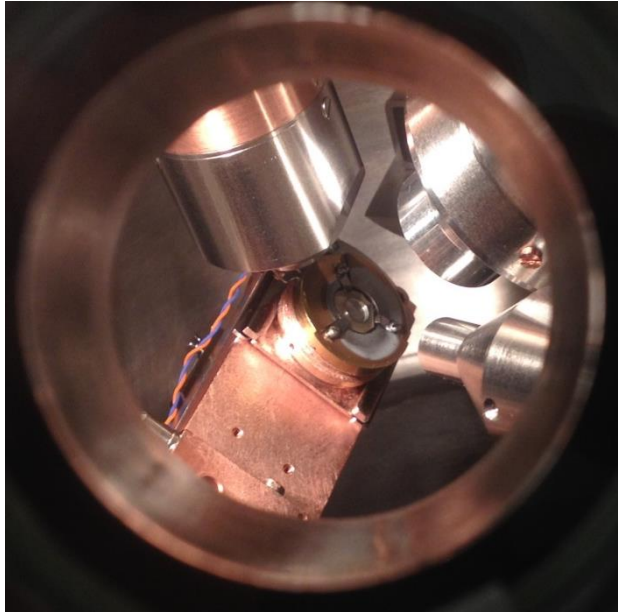


Figure 5.1: Ag reference sample during analysis.

Metal foil samples were chosen to study the effects of measurement parameters on spectra. Silver (Polycrystalline Ag), copper (Cu(100)) and tantalum (polycrystalline Ta) samples were cleaned by sputtering at 1.00 keV beam energy for 5 minutes. They were then annealed for 20 minutes at 700-800 °C.

5.2.3 Tantalum Knife Edge

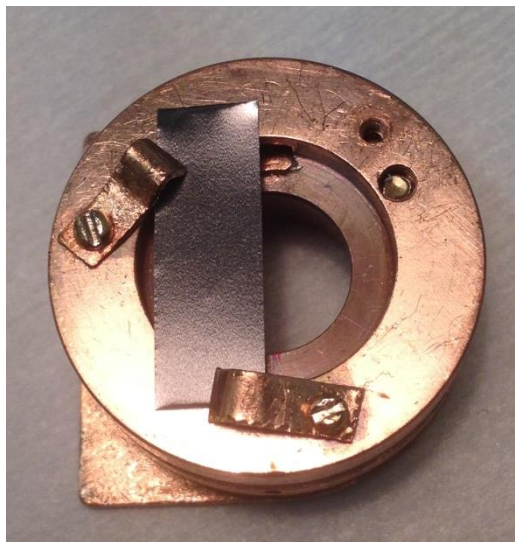


Figure 5.2: Ta foil knife edge mounted on a hollow Cu sample holder.

In order to study the spatial resolution of the analyzer lens system, a knife edge was prepared. Based on the technical specifications of the analyzer system, a factory cut edge was deemed sufficiently sharp for measurements of lateral resolution. Tantalum

foil of 0.009 mm thickness was mounted on two separate Cu sample holders, one hollow and one solid. Samples were sputtered at 1.00 keV beam energy for 5 minutes to ensure a clean surface to maximize peak intensity and signal to noise ratio.

5.2.4 Platinum Foil with Copper Deposition

In order to test different copper electrodeposition parameters, platinum foil was used.

Polycrystalline Pt foil was trimmed into four 6 mm x 13 mm rectangular strips. A copper electrodeposition solution was prepared by mixing 1 mM CuSO_4 (99.999%, 203165 Aldrich) de-aerated electrolyte in 0.1 M H_2SO_4 . An Ag/AgCl reference electrode was used for the electrodeposition. The solution was flushed with N_2 to remove O_2 from the solution, thus limiting oxidation during the deposition process.

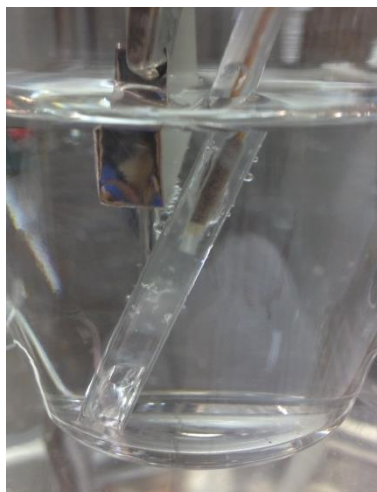


Figure 5.3: Electrodeposition experimental setup, with visible Cu bulk deposition on Pt foil shown.

Prior to the electrodeposition process, all samples were pretreated according to the same procedure. Final treatment differed for each sample.

1. Pre-cleaning the sample by rinsing in deionized water and sonicating in ethanol
2. Cathodic pre-treatment to reduce native oxides: 5 cycles from -0.3 V to +0.4 V at 50 mV/s
3. Cyclic voltammogram: 5 cycles from -0.2 V to +0.7 V at 5 mV/s to bulk deposit Cu with no Pt oxidation
4. Cyclic voltammogram: 5 cycles from +0.2 V to +0.7 V at 5 mV/s to underpotential deposit Cu
5. 10 minutes holding at rest potential of +0.7 V
6. Final treatment
 - a. Underpotential deposition of Cu: rest potential at +0.2 V for 10 minutes
 - b. Bulk deposition of Cu: rest potential at -0.2 V for 10 minutes
 - c. Deposition-free treatment: rest potential at +0.7 V for 10 minutes

- d. Immersion in electrolyte solution for 10 minutes without voltage

All four Pt foil samples were mounted to a sample holder and analyzed with XPS. Results were used to plan for further electrodeposition treatments at fixed current.

5.2.5 Planar Interdigitated Electrode (IDE)

Two planar interdigitated electrodes were purchased from Synkera Technologies, Inc. Factory specifications describe the sample as 5 platinum electrode pairs deposited on a 0.635 cm (0.25 inches, imperial units are listed in the data sheet) square aluminum oxide (Al_2O_3) substrate with a thickness of 0.0254 (0.01 in). Fingers are listed as 0.254 cm (0.1 in) long, and 0.01 cm (0.004 in) thick. Spacing between electrode fingers is listed as equal to their width. Contact pads are located at diagonal corners to allow for easy connection to electrodes [31].

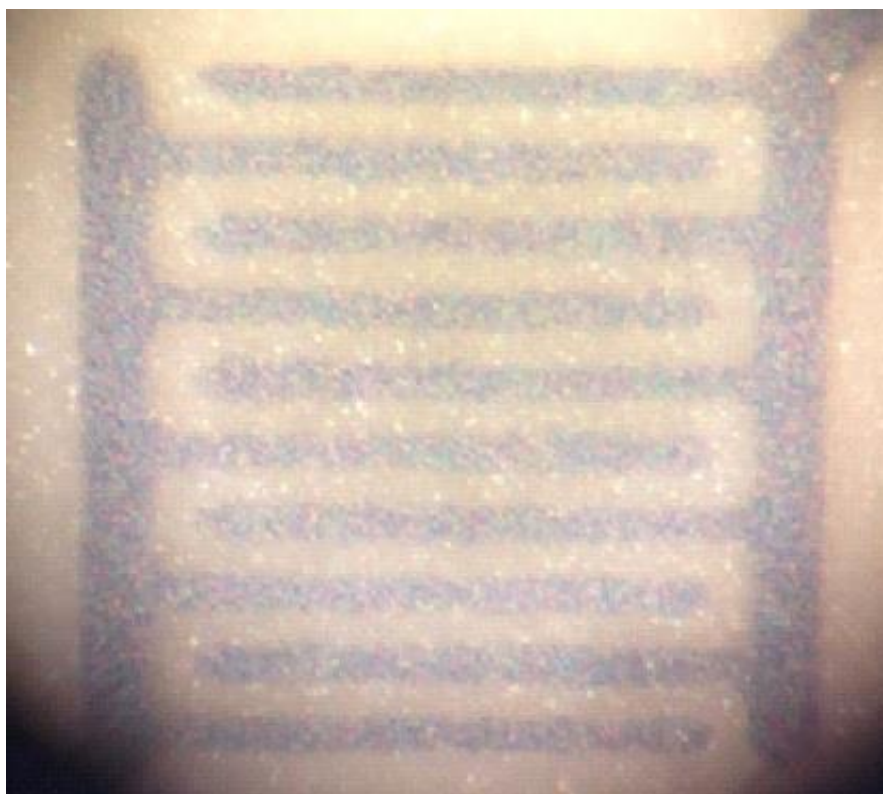


Figure 5.4: Optical microscope image of IDE Pt fingers prior to Cu deposition.

Cyclic voltammogram measurements were also completed for the IDE sample as to study differences between Pt foil and the IDE. A preliminary 2 nm Cu deposition was carried out, and deposition thickness was verified with XPS measurements. With the deposition technique tested, a second IDE sample was prepared with a thicker layer of deposited Cu.

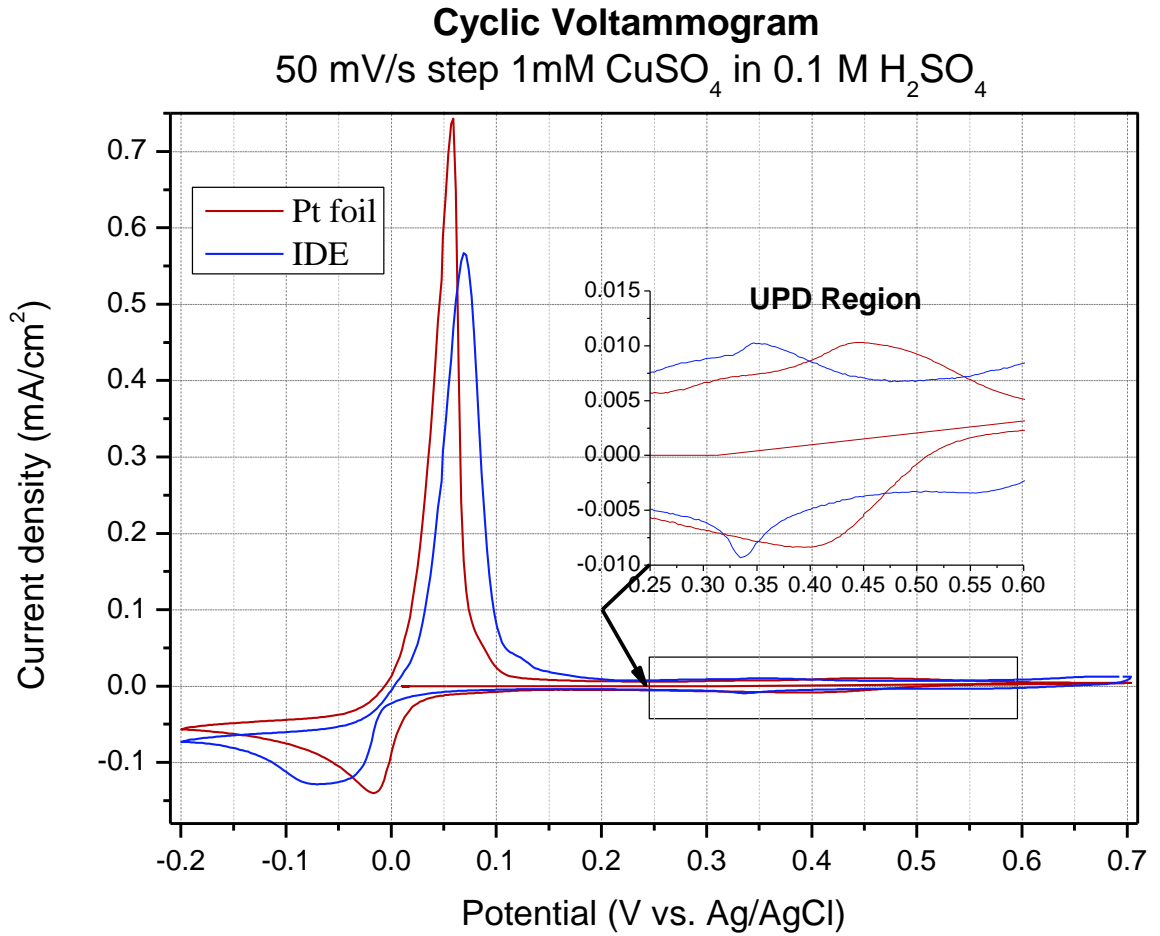


Figure 5.5: Cyclic voltammetry results for Pt foil reference and IDE sample.

The voltammetry results above show distinct curves for the Pt foil and the IDE electrode, due to differences in the Pt surface structures and possibly influenced by irregularities in the reference electrode. Based on Faraday's laws of electrolysis, deposition can be estimated by multiplying current by time; according to the equation [32]:

$$m = QA/nF \quad (5.1)$$

where m is the deposited metal mass in grams, Q is the net charge that passes through the circuit in Coulombs, A is the atomic weight of the metal, n is the number of electrons, and F is Faraday's constant. The above equation may be rearranged to take into account the properties of the deposited species and the electrode surface [32]:

$$\zeta = \frac{ItM}{\delta Fa\rho} \quad (5.2)$$

where ζ is the deposition thickness, I is current in amps, t is time in seconds, M is molarity in grams per mol, δ is charge of species, F is Faraday's constant, a is electrode surface area in square centimeters, and ρ is density in grams per cubic centimeter. The calculations for the two IDE depositions can be seen in the appendices (Appendix D).

Constant current mode was used for Cu deposition on the IDE sample. Using the previous equations, current density of $-500 \mu\text{A}/\text{cm}^2$ was applied for 544 seconds so that 100 nm of copper would be deposited. With constant current mode, the measured potential was allowed to vary; at such high current the voltage fluctuated around -0.25 V for the deposition period, which would be located directly left of the potential range displayed in the plotted voltammogram. The visible appearance of the copper deposition was concurrent with this thickness, as seen in the figure below.

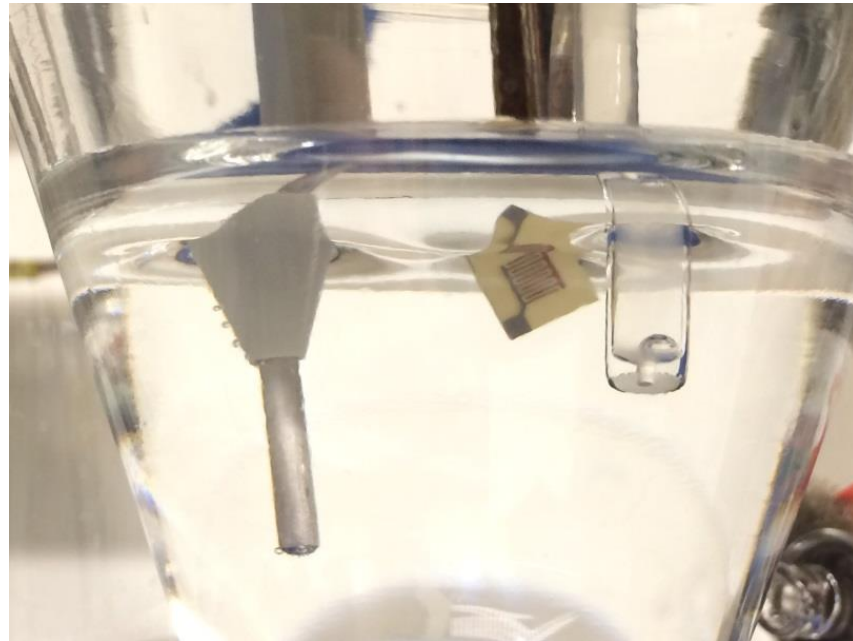


Figure 5.6: IDE Cu deposition; voltage is applied to one contact pad such that Cu is deposited to a single set of fingers.

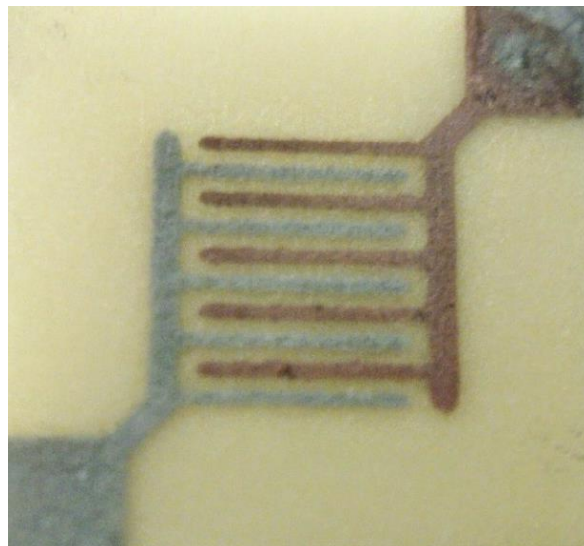


Figure 5.7: Photograph showing 100 nm Cu deposition on the IDE sample.

The above image depicts the results of Cu deposition, which appears to be uniformly deposited when viewed under an optical microscope. However, higher magnification SEM images are necessary to see the deposition results.

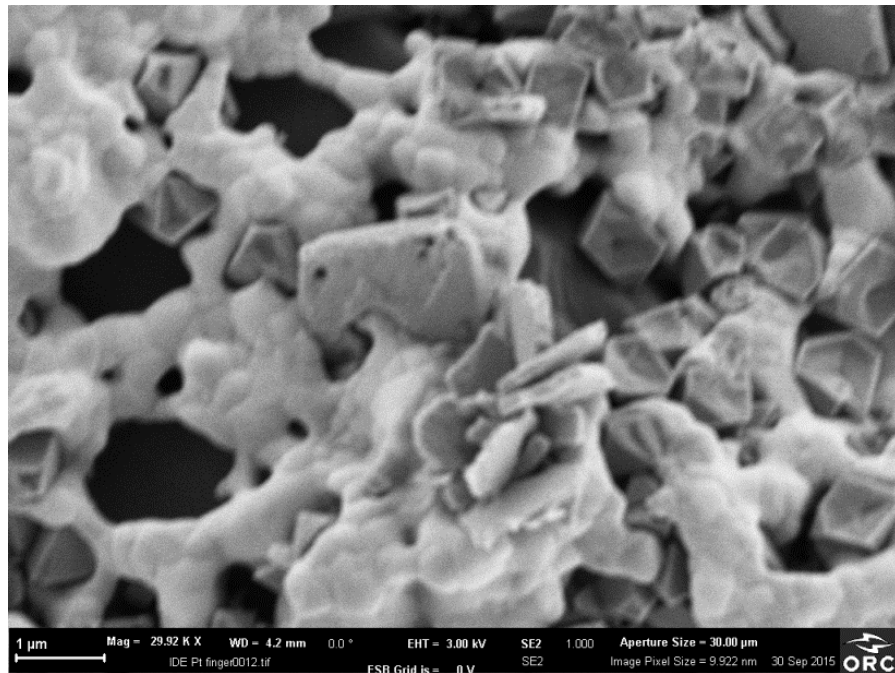


Figure 5.8: SEM image of a Pt electrode finger.

SEM measurements of the platinum electrode display semi-porous heterogeneous Pt.

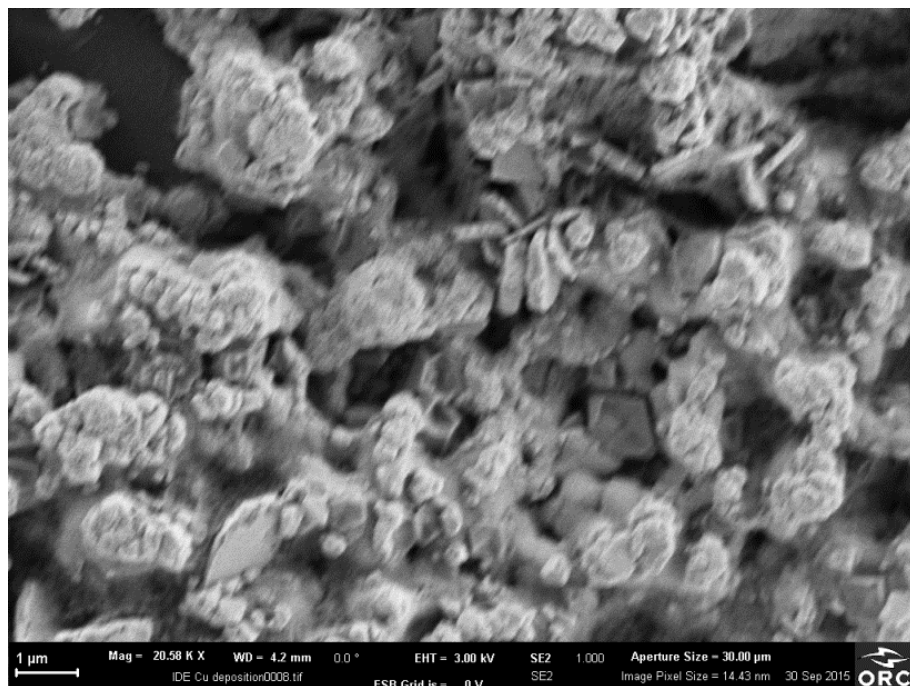


Figure 5.9: SEM image of Cu deposited on a Pt electrode finger.

The SEM image of an electrode finger covered with Cu deposition shows porous Cu deposition over the Pt electrode finger.

5.3 Sample Mounting

In order to introduce samples to the analysis system, they must be mounted to a standardized sample holder so that they can be moved through the system securely.

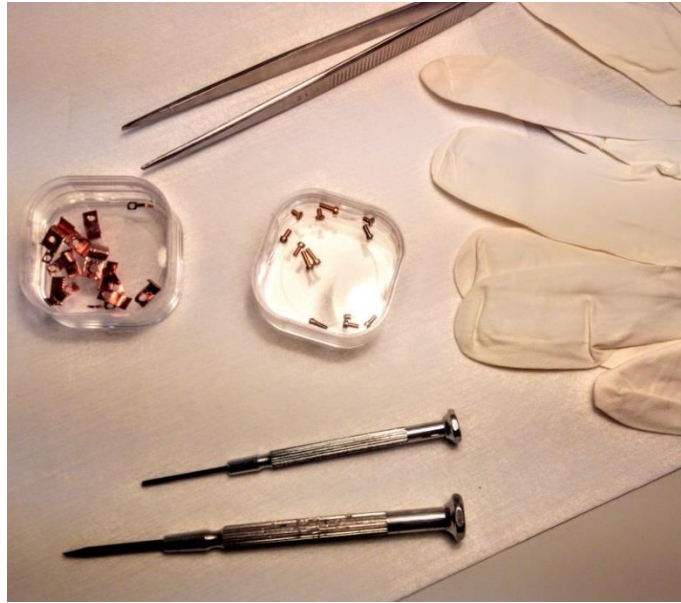


Figure 5.10: Sample mounting equipment; clips, screws, tweezers, screwdrivers, and nitrile gloves.

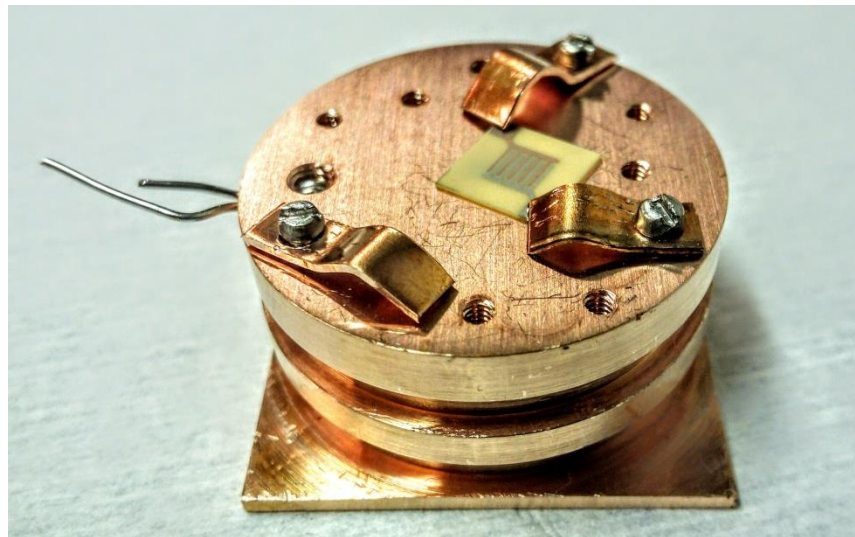


Figure 5: IDE sample mounted to a copper sample holder.

Moreover, clips must be attached to the sample such that current is able to pass through the sample, sample holder, and thermocouple wires to prevent sample charging.

5.4 Sample Loading

Prior to opening the microchamber flange and loading the sample, protocol must be followed to avoid pressurization of other chambers and prevent damage to the system. This protocol is subject to frequent modifications, as alterations are made to the system. This procedure is described in depth in the appendices (Appendix A).

5.5 Sample Transfer within the System

The analysis system contains multiple chambers which are separated from each other by gate valves. There are three mechanisms for movement of the samples within the system: wobble sticks, carousel, and cart. Wobble sticks are manipulated by the operator and used to transfer the sample from the cart to a stationary position: in the microchamber, Fast Entry Air Lock (FEAL), preparation chamber, STM chamber elevator, or analysis chamber manipulator. The cart is moved along rails which allow for transfer between chambers, and the rail track can be shifted in the preparation chamber by rotating the carousel.

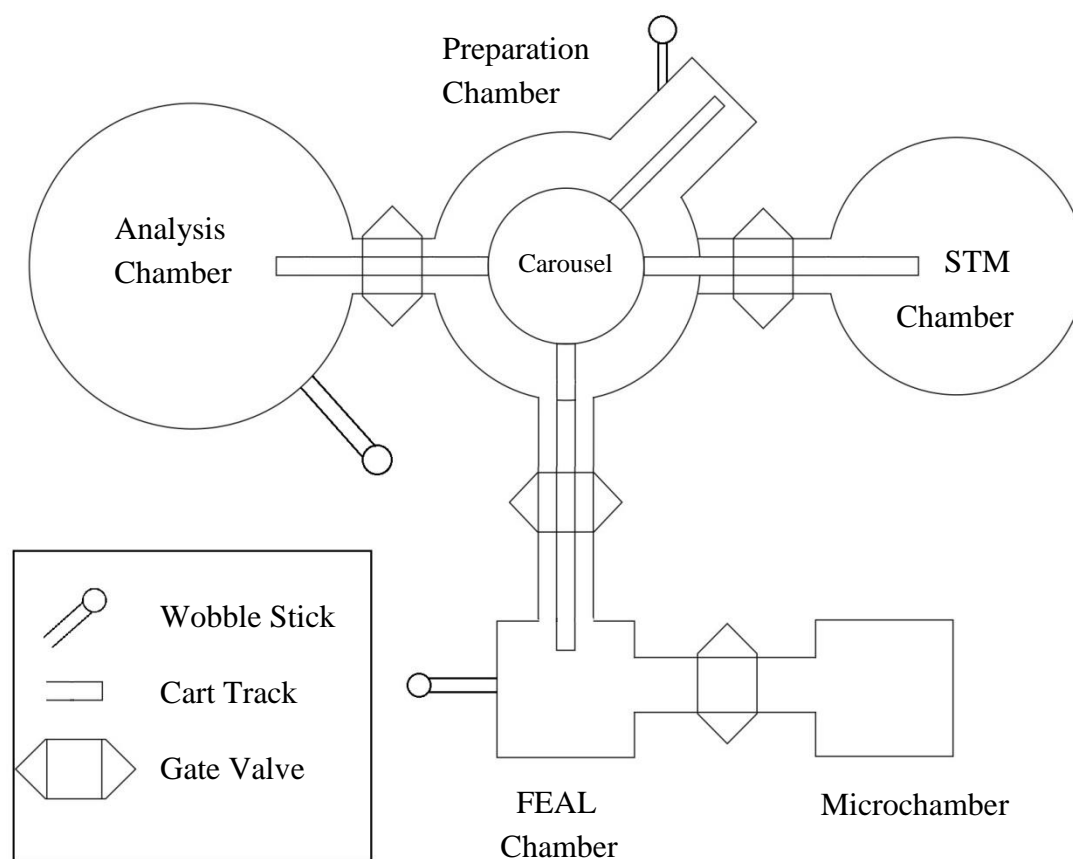


Figure 5.12: System schematic diagram depicting sample transfer within the system.

The above figure displays a schematic representation of how a sample is moved within the system. To move from the microchamber to the analysis position, the sample is first transferred via the FEAL wobble stick to the FEAL chamber. It is then transferred from the FEAL wobble stick to the cart, which is drawn into the preparation chamber. The carousel is then rotated 90 degrees and the cart is transferred to the analysis chamber. Finally, the analysis chamber wobble stick transfers the sample from the cart to the sample manipulator. The manipulator is then moved to the analysis position.

5.6 Spectral Measurements

XPS measurements are controlled via MATRIX software, which was provided with the Omicron system. Spectral measurements are the first type of measurement that will be discussed.

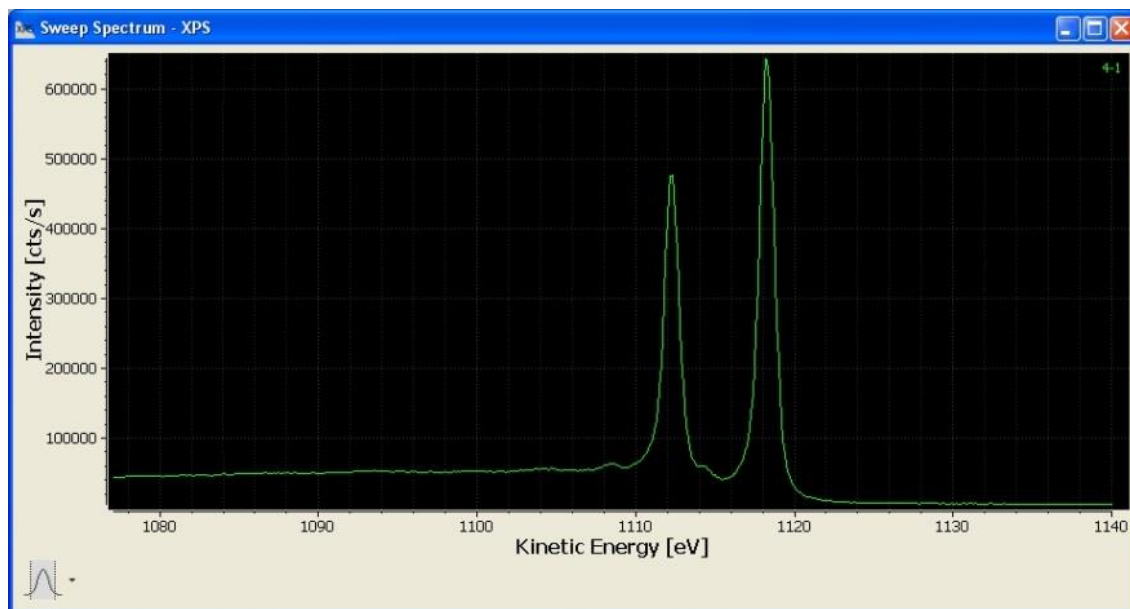


Figure 5.13: Sweep Spectrum visible in MATRIX Software [33].

Sweep spectra are measured by defining an energy range, step size, and dwell time for each step. Multiple sweeps increase the signal to noise ratio, and are often necessary for measurements with lower peak intensity and/or a high background. This is the most useful measurement mode for quantitative XPS measurements; however, it is also the most time consuming. The time required for sweep spectra is significant because the analyzer cycles through the studied energy interval step by step. This is the only option for measuring larger energy ranges. Sweep spectra were measured for metal foil samples, and also for survey spectra of the IDE and Pt foil samples.

The other available option for measuring spectra is the snapshot mode. Snapshot mode is more efficient (in terms of measurement time) when measuring a single transition, since it assigns a discrete energy to each channel, and thus measures the entire energy window simultaneously. The size of the interval is dependent on the E_p used; for measurements of the IDE sample, maximum E_p (200 eV) was utilized.

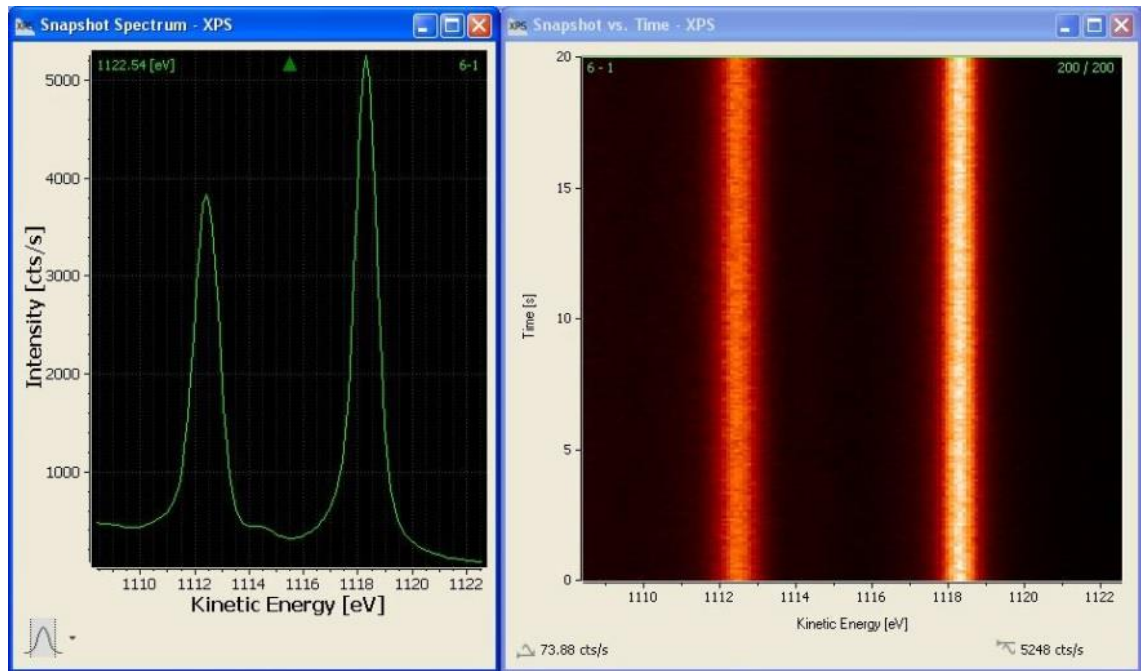


Figure 5.14: Snapshot spectrum mode as visible in MATRIX software. The spectrum on the left shows the sum of all snapshots, while the right image shows a plot of all the snapshots, with intensity indicated by color [33].

Images and line scans are composed of snapshots, with one snapshot measured at each pixel or point. Thus, the information contained at one pixel in an image or one point in a line scan is equivalent to the spectrum in the above figure.

5.7 Imaging

Imaging using MATRIX software is carried out by defining the energy snapshot to be measured, then setting the measurement area and number of points to be used in the X and Y directions. Imaging can be very time consuming if a longer dwell time is used and many points are measured, as the lens system moves the analysis spot and measures a snapshot spectrum for each pixel individually. Maximum dwell time is 15 seconds for each snapshot, and a maximum of 200 points in each direction is permitted. This would correspond to 7 days of continuous measurement.

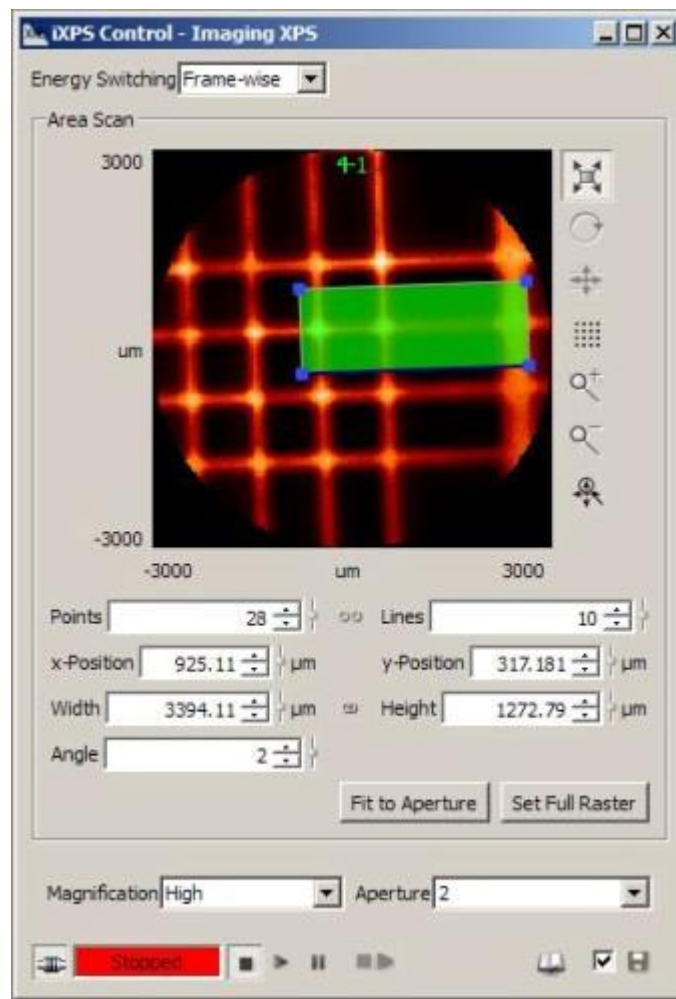


Figure 5.15: Imaging control as viewed in MATRIX software [33].

Once an image has been recorded, a smaller region corresponding to a particular feature from the image can be imaged separately. The figure above shows this option. Thus, images were obtained by measuring a quick image of a large area, then selecting a smaller area for a higher quality measurement of the surface of interest.

5.8 Line Scan Measurements

Once an image has been recorded, a line scan can be measured. A linear path is selected between pixels from the imaging measurement, and the number of points is defined. The lens system moves the analysis spot along the path measuring a snapshot spectrum for each consecutive point.

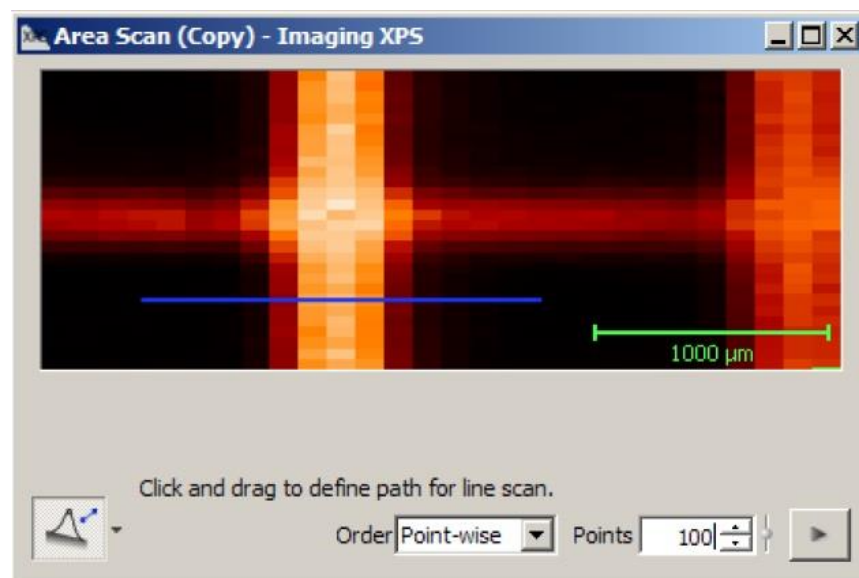


Figure 5.16: Line Scan control as viewed in MATRIX software [33].

The same MATRIX window used for line scans also allows individual pixels to be selected for multipoint spectroscopy, where snapshots or sweep spectra are measured for each selected point.

5.9 Data Processing

MATRIX does not allow results to be viewed or analyzed. Vernissage software opens MATRIX result files and exports them so that they can be processed with CasaXPS. Using CasaXPS software, spectra (including sweep spectra, images and line scans), were processed to fit regions and components [34].

6. RESULTS AND DISCUSSION

This section will present the results of measurements and the analysis thereof.

6.1 Studies of the Analyzer

Measurements of metal foil reference and knife edge samples were used to study the analyzer. The results and discussion of these results will be presented in this section.

6.1.1 Comparison of Silver 3d Measurements

Silver foil was studied under different measurement settings to investigate the behavior of the analyzer. Results of studying the Ag 3d transition using different apertures and pass energies are shown below.

Comparison of A4High Results for Ag 3d_{5/2} Spectra, CAE = 10 eV, 50 eV, 200 eV

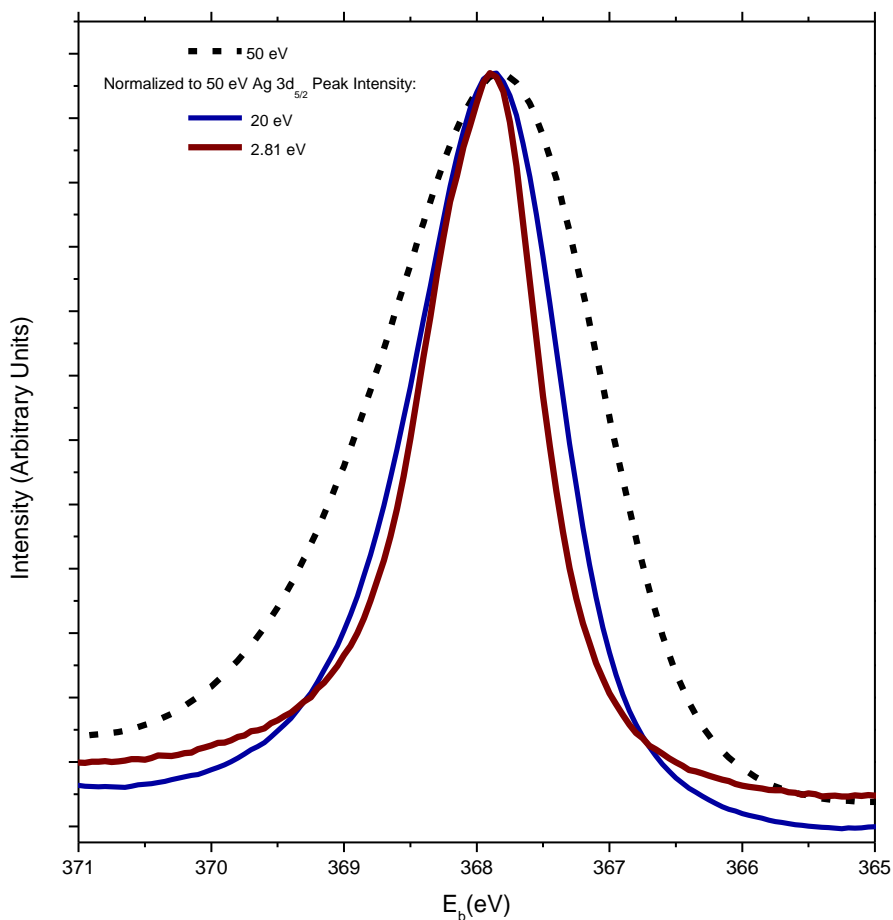


Figure 6.1: Ag 3d_{5/2} XPS peak, measured with different pass energies.

In the previous figure, spectra measured at 2.81 eV and 20 eV were normalized to the peak intensity of the 50 eV spectrum so that their peak shapes could be visually compared. Increasing E_p has the effect of broadening peaks (increasing the FWHM). This effect is quantified in the figure below.

Ag 3d FWHM vs. CAE, High Magnification, A3, A4, A5, A6

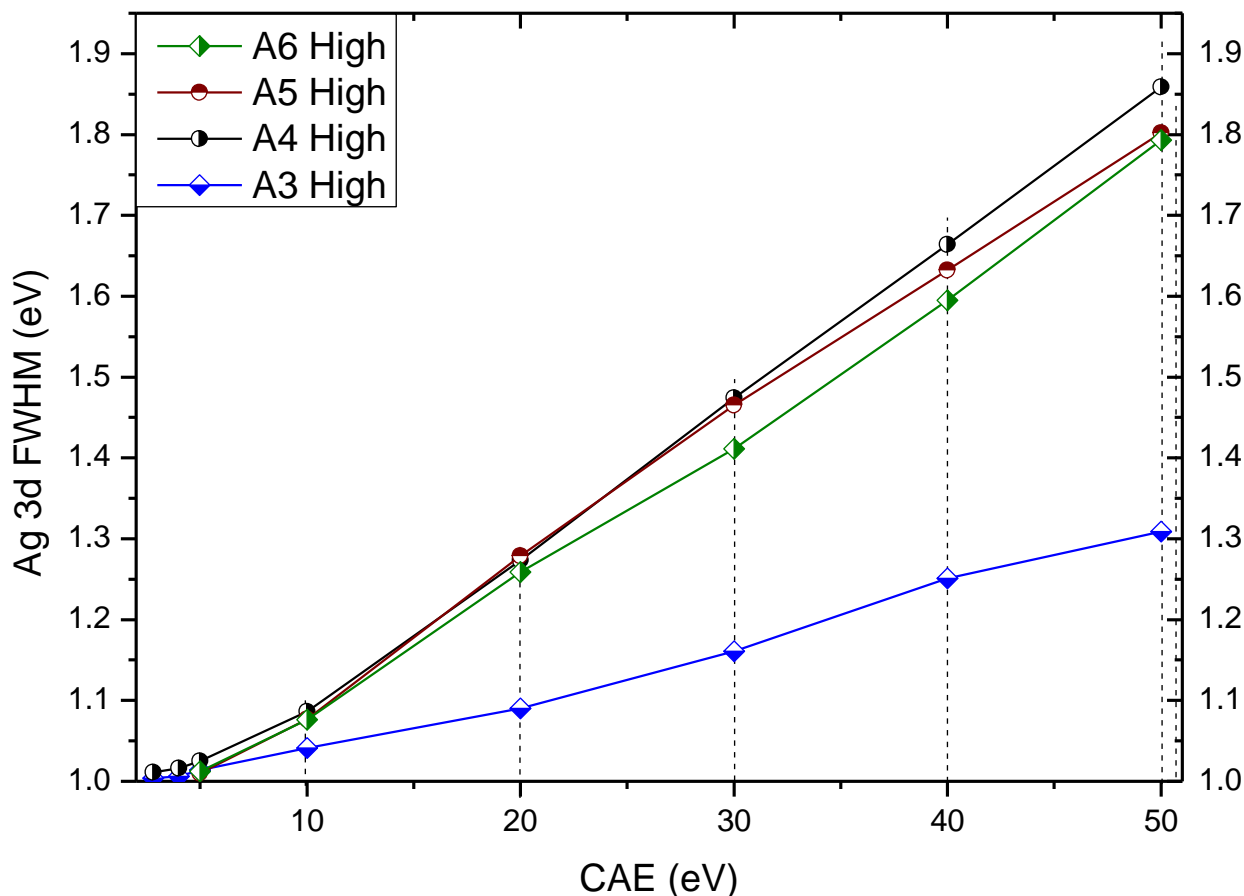


Figure 6.2: FWHM of Ag 3d_{5/2} of XPS spectra vs. pass energy. This figure plots results for quantitative aperture settings: A3, A4, A5, and A6.

The above figure shows that while A4, A5 and A6 apertures show a large increase in FWHM as E_p increases, while A3 aperture shows a slower increase. This indicates that A3 aperture is the ideal setting for higher resolution quantitative measurements.

Ag 3d Intensity, High Magnification, Apertures 3, 4, 5, 6

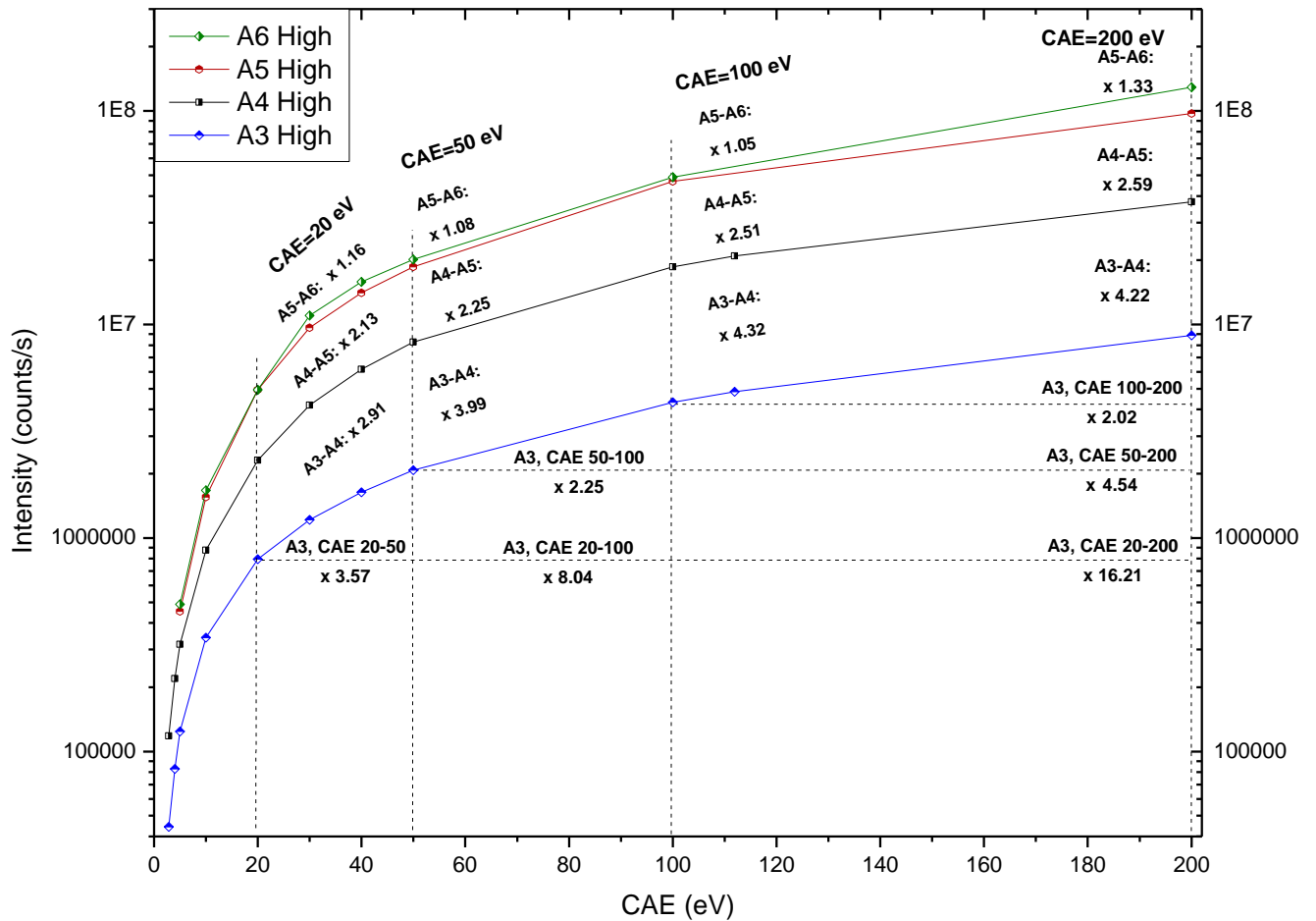


Figure 6.3: Intensity vs pass energy. The increase when shifting between characteristic pass energies is notated with a factor of intensity increase.

The figure above shows how intensity increases as E_p is increased. Larger apertures record higher intensities; the factor increase for characteristic pass energies is labeled in the figure.

6.1.2 Measurements to Study the Analyzer's Transmission Function

In order to compare the transmission function of the analyzer to the expected results, spectra were measured using Al $K\alpha$ radiation for silver, copper and tantalum reference samples. The spectra were analyzed and the results were compared to those presented in the analyzer manual. The measured results and data from the manual are shown side by side in the following figure.

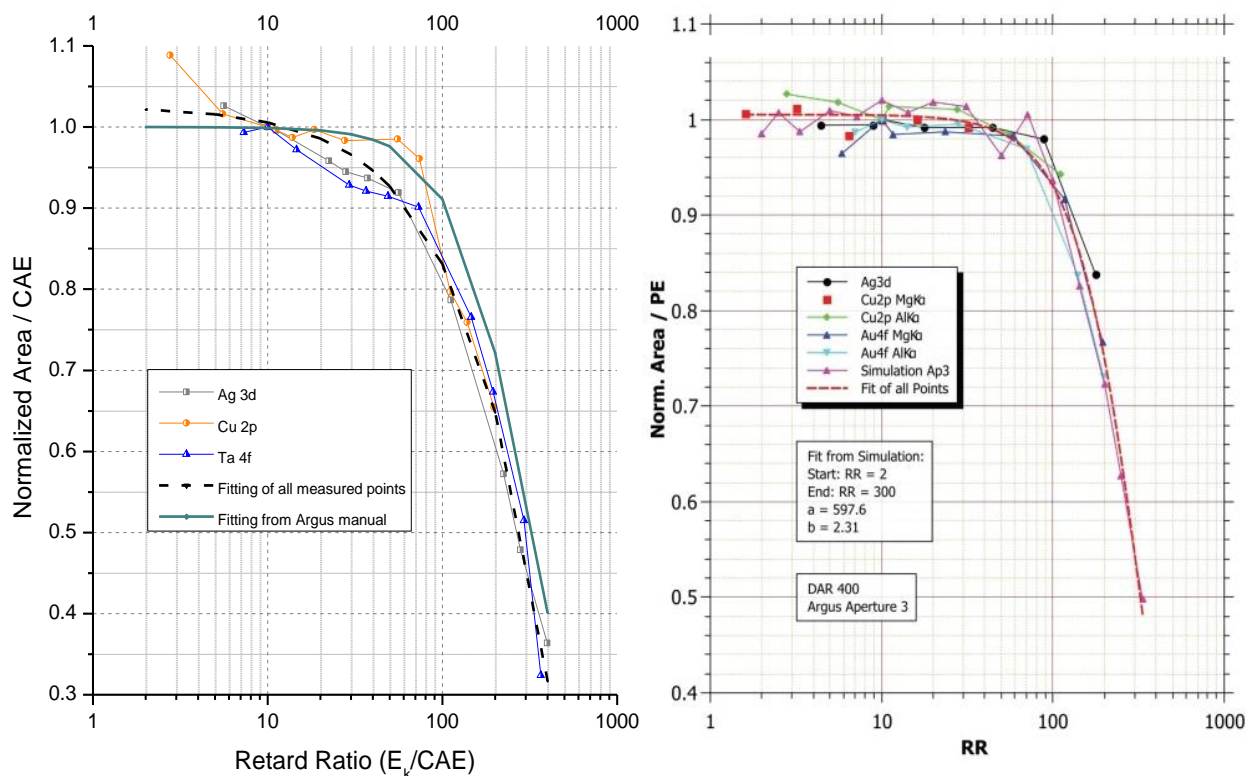


Figure 34. $I(\text{RR})$ vs. $\log\text{RR}$ plot for Argus analyser using aperture 3.

Figure 6.4: Normalized area divided by pass energy vs. retard ratio. The left figure presents recorded measurements of metal reference samples, while the figure at right is provided in the analyzer manual [1].

The comparison of the two figures shows similar behavior, but the difference between the experimental results and the manual simulation can be seen in the left figure (with the dashed black line representing experimental data and the green line representing the manual's fitting). Additional measurements of more reference samples, including both Mg and Al anodes would allow a customized transmission function to be applied to future measurements.

6.1.3 Knife Edge Measurements to Study the Analyzer's Lateral Resolution

Line scans were taken over the knife edge with the sample centered below the analyzer. Snapshot spectra recorded at each point were processed to obtain component fittings for the Ta $4f_{7/2}$ XPS peak. The data points, containing the point distance coordinate and the component intensity were analyzed using ImageJ software to obtain a 16%-84% intensity Fermi function fitting. Line scans over a knife edge are the most reliable technique to quantify the spatial resolution of the analyzer. When taking a line scan across a knife edge, the spatial distance between points of 16% and 84% intensity (when a line scan is measured across a sharp feature) is indicative of the system's ability to resolve small surface features.

Examples of fittings from the Ta 4f transition can be seen in the following plots.

Comparison of Measured Ta 4f Transition for A2, All Magnifications

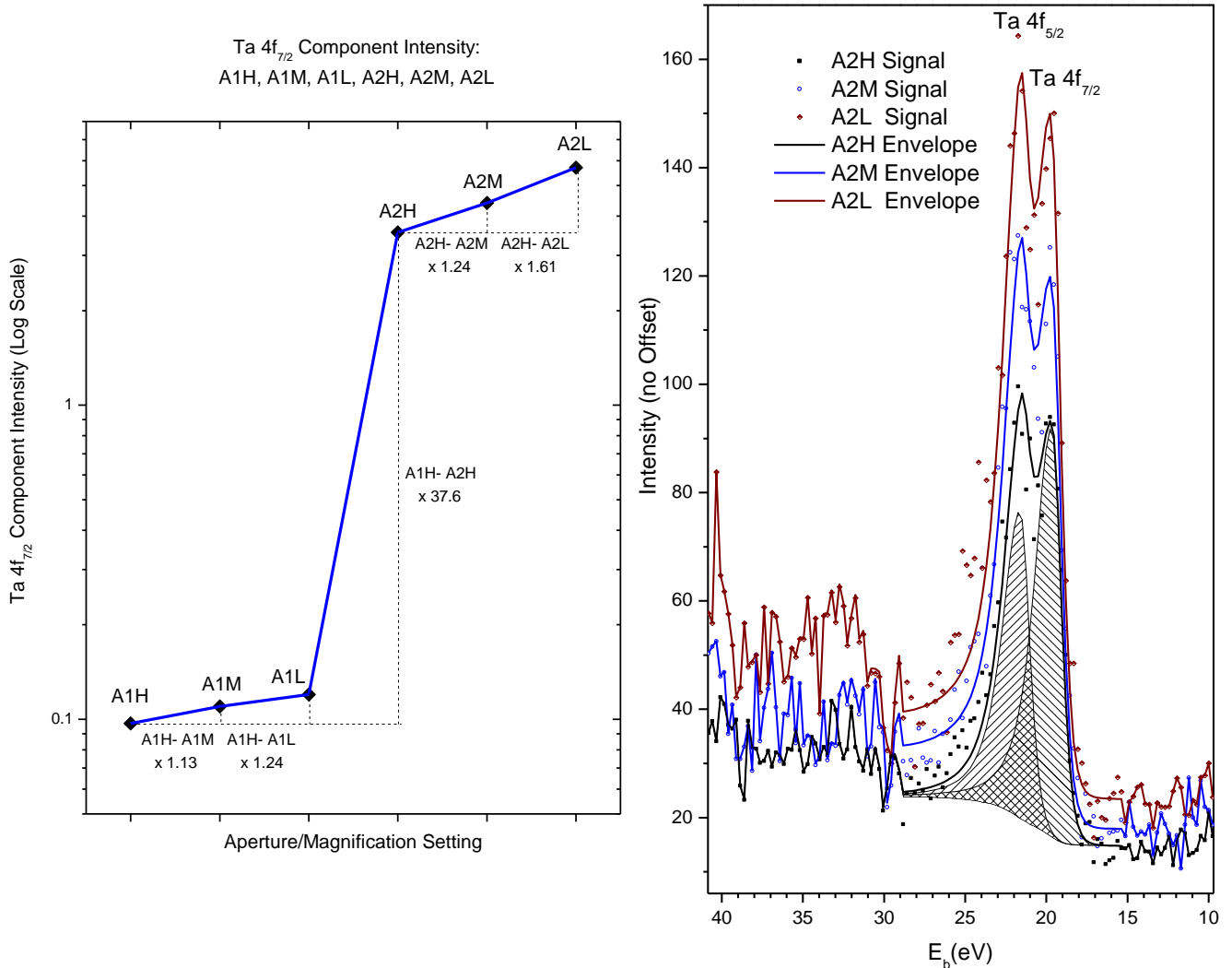


Figure 6.5: Change in Ta 4f_{7/2} component intensity when shifting between magnifications and apertures A1 and A2. The figure at left graphs the factor increase in intensity, while the figure at right plots A2H, A2M, and A2L snapshots with no offset.

Example snapshot spectra from each magnification setting (measured with A2 aperture) are shown in the figure at right. The spectra have no offset, so the higher peak intensity for medium and low magnification settings are representative of the larger analysis spot area. The figure at left shows the signal intensity increase quantified based on the factor of increase when shifting between magnifications for A1 and A2 apertures. This is always a relevant consideration for imaging and line scans, as quality component fittings are very difficult; the remaining response is to increase dwell time to make the data from lower intensity spectra more reliable.

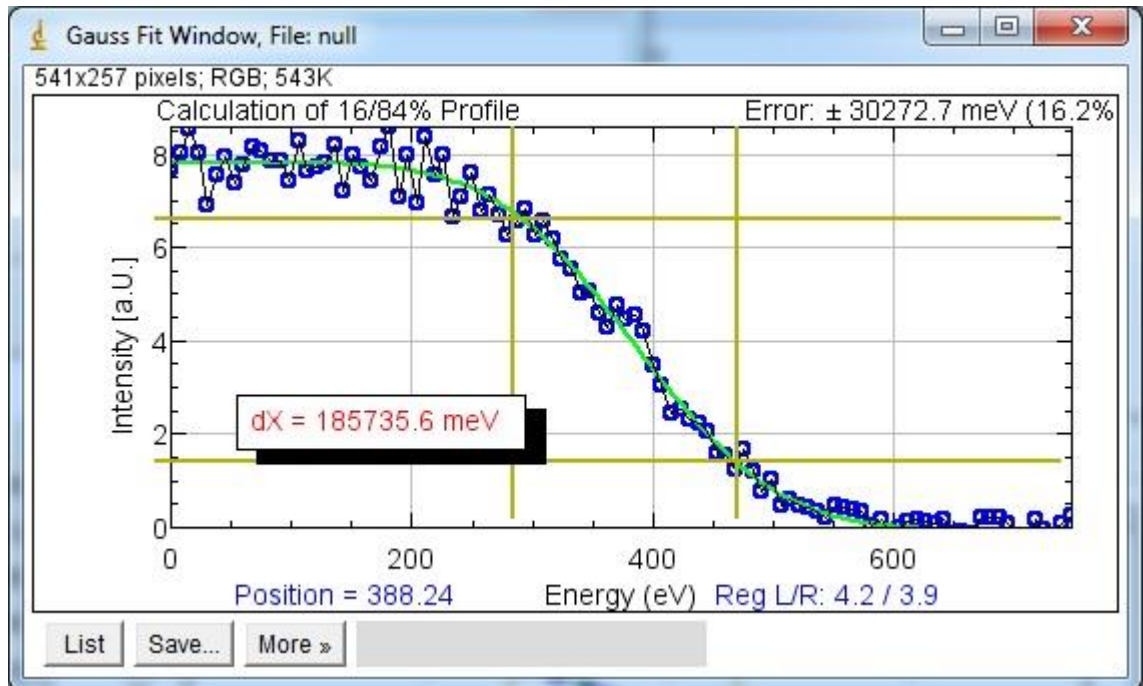


Figure 6.6: Fermi Fit calculation of knife edge results as seen in ImageJ software

The figure above shows an example of the calculation of the 16%-84% intensity. The following figure depicts the best obtained spatial resolution results for A1 aperture with each magnification setting.

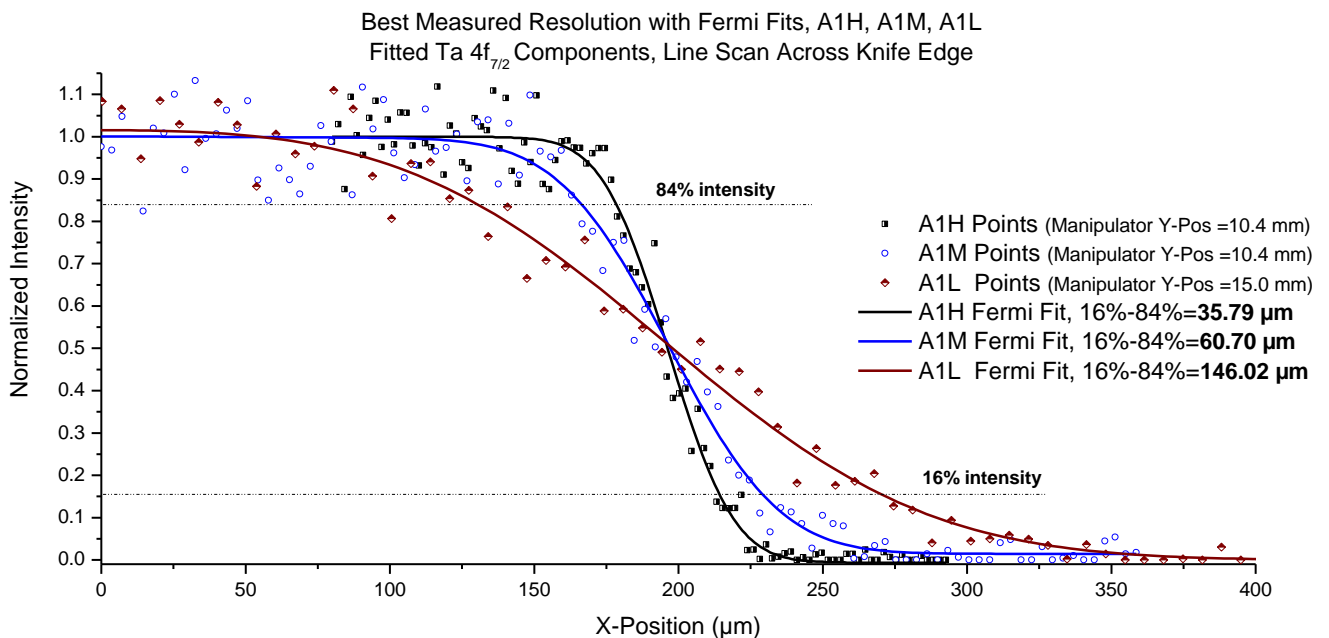


Figure 6.7: A1 line scans across the knife edge including Fermi Fit 16-84% intensity measurements.

As seen in the previous figure, higher magnification settings give better resolution. The calculated resolution values are an improvement over those listed in the manual.

6.2 Interdigitated Electrode with Copper Deposition

This section will present the results of measurements of the IDE sample.

6.2.1 Spectra and Images

The IDE was first analyzed with spectra at specific locations using A2 aperture.

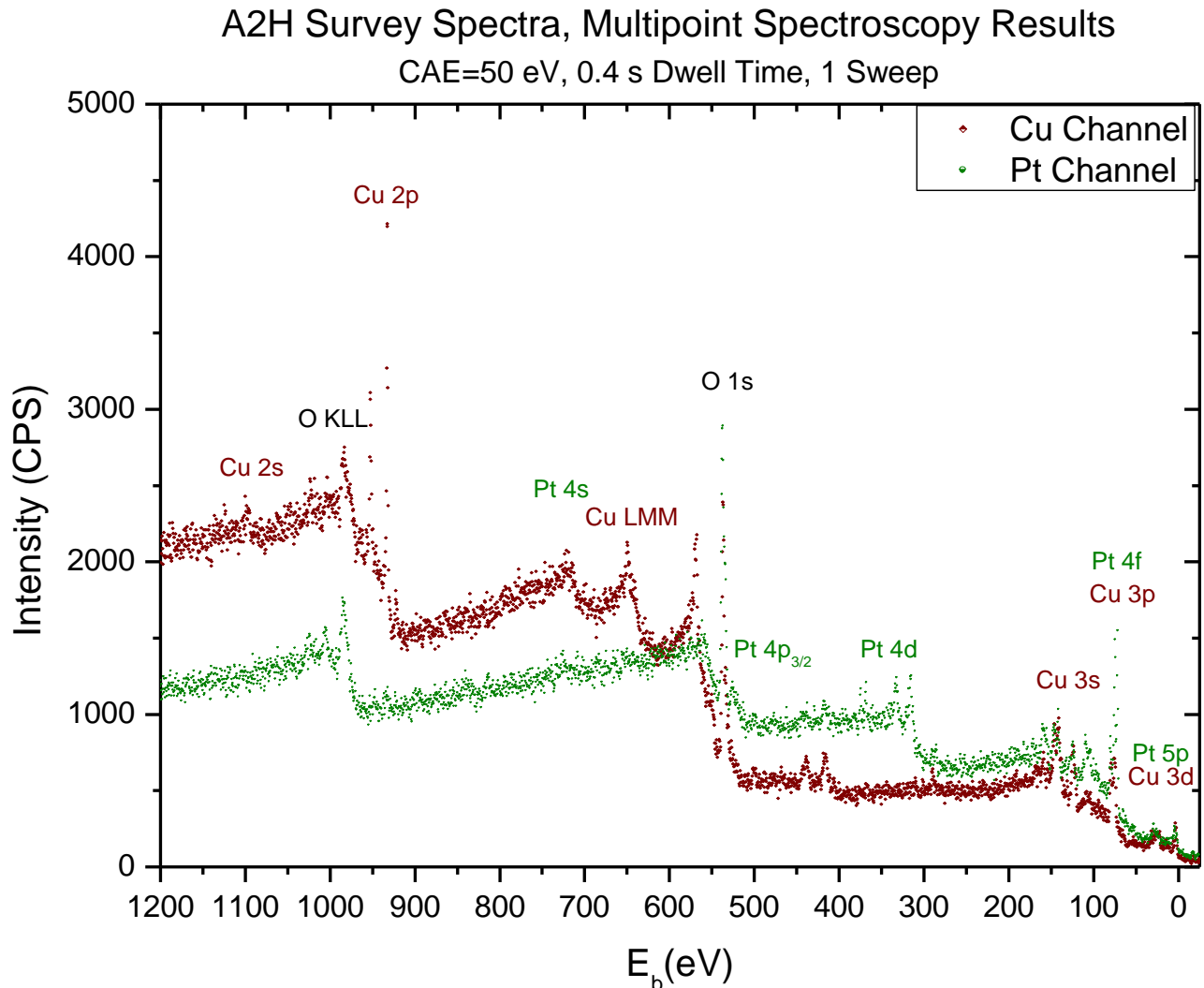


Figure 6.8: XPS survey spectra taken with A2H at opposite corners of the IDE sample.

The above survey spectra were measured at opposite corners of the sample, one on the Cu deposited electrode and the other on the Pt electrode. Noticeable transitions in the spectra are labeled with Pt features in green and Cu in red; O signal is present in both spectra. Based on the intensity and overlap of these survey spectra, Pt 4f, O 1s, and Cu 2p were chosen as the measured transitions for imaging. The locations of measurements are indicated on an image of the sample below in red and green.

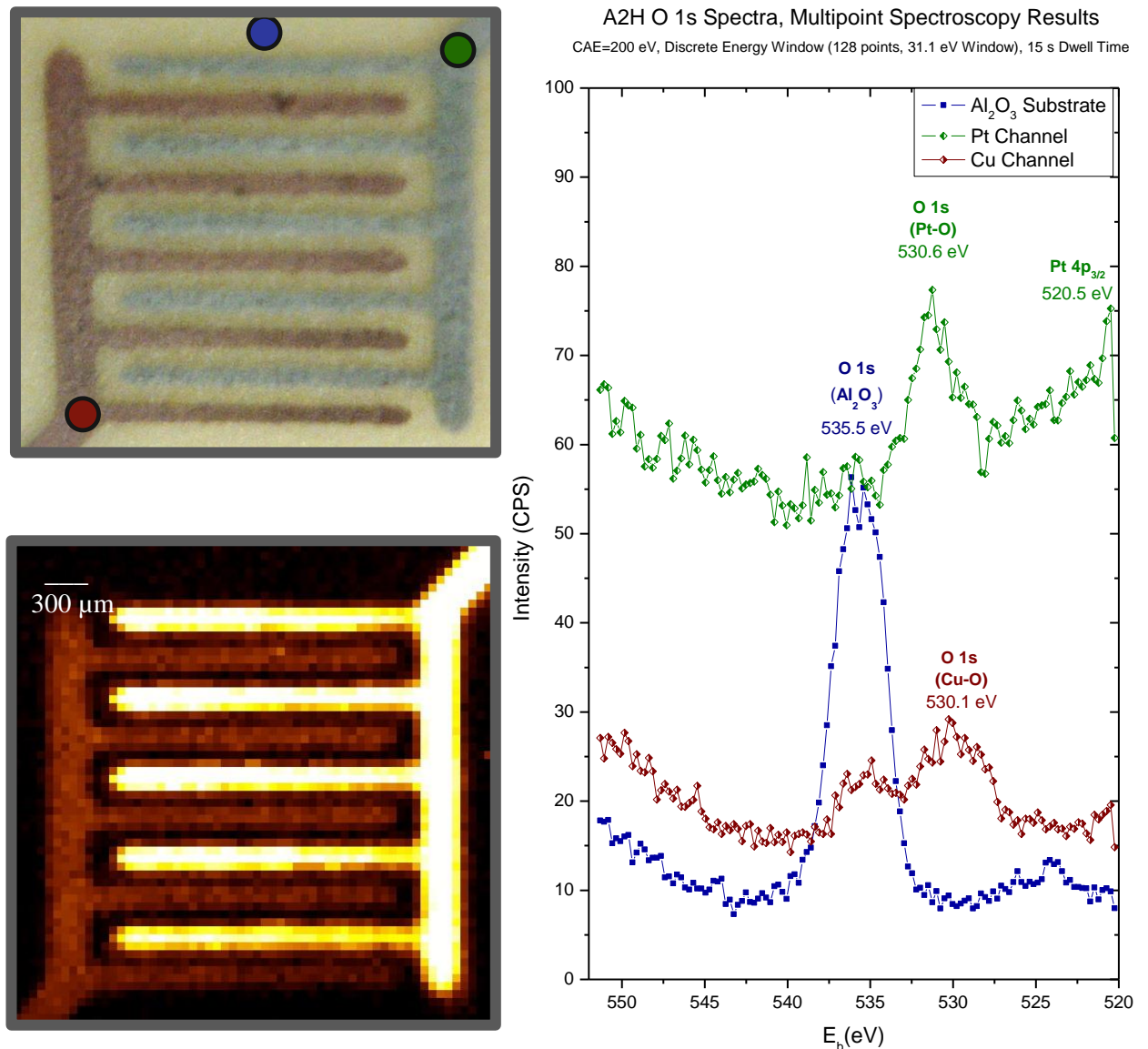


Figure 6.9: Comparison of A2H Multipoint Spectroscopy O 1s Snapshot Spectra measured at different points. Locations of measurement points are indicated on an image of the IDE fingers at the top left. The bottom left image shows the raw data obtained for the image measured with snapshots taken for the O 1s transition.

The above figure shows the locations of multipoint spectroscopy labeled on an image of the IDE sample. At the top left, the locations of the overlaid spectra recorded with multipoint spectroscopy are labeled. At the bottom left, raw data from a 60×60 point image of the O 1s transition is presented. Since the raw data depicts integrated counts for the whole region, it can be inferred from the overlaid spectra that Pt will have the highest intensity, then Cu, then Al₂O₃. Pt background is particularly high at the O 1s energy because of the presence of the Pt 4p_{3/2} transition just right of the O 1s peak. Since Al₂O₃ is an insulator and not grounded via the thermocouple, this material experiences charging due to the X-ray source. The consequence is that the Al₂O₃ oxide peak is shifted left on the spectrum by 5 eV. However, the energy shift between oxide species is not large enough to allow Cu-O and Pt-O to be distinguished from each other.

Sum Spectrum of O 1s Transition with Fitted Components

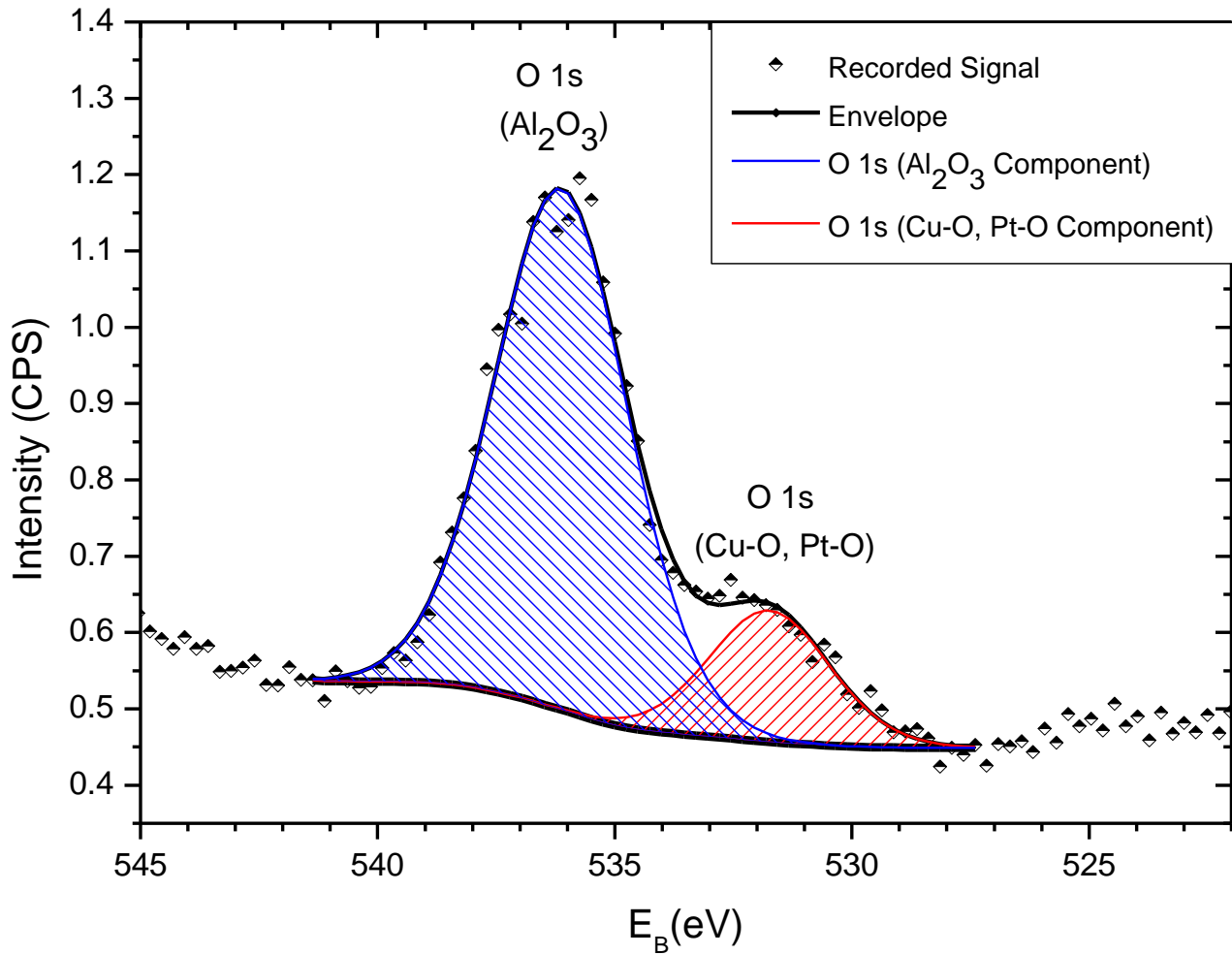


Figure 6.10: Sum spectrum from all image pixels for measurement of the O 1s transition with component fittings.

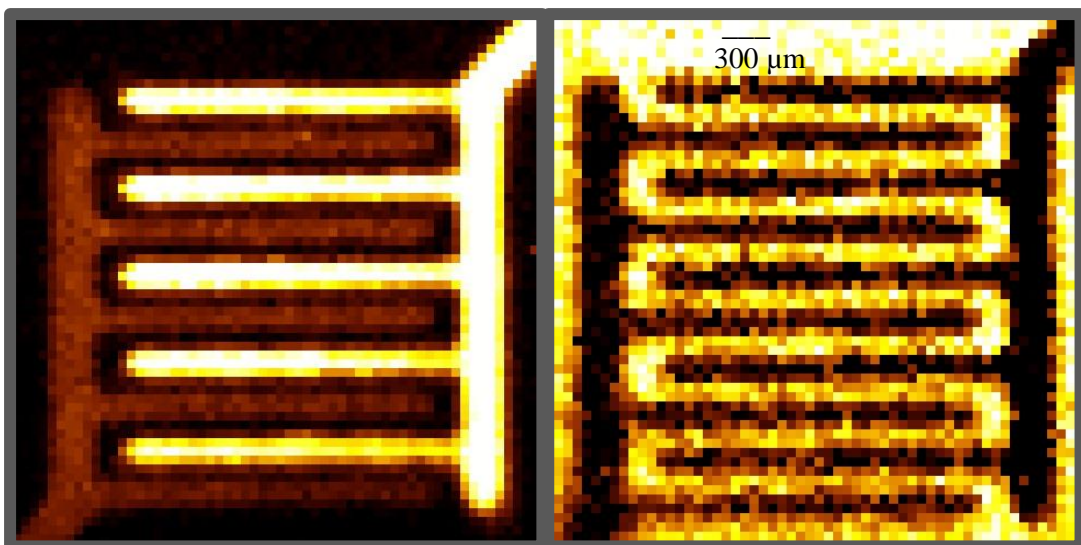


Figure 6.11: Unprocessed image vs. component fitted image, O 1s transition.

As seen in the previous O 1s spectrum, the shift due to charging makes the Al_2O_3 component easy to distinguish from other oxygen species.

The previous figure presents two images, the raw data, or unprocessed image on the left, and the component fitted image on right. This is an excellent example showing the importance of component fitting and background subtraction for data processing; the pixels with the lowest intensity in the unprocessed image become the most intense when a component fitting is applied and background is subtracted.

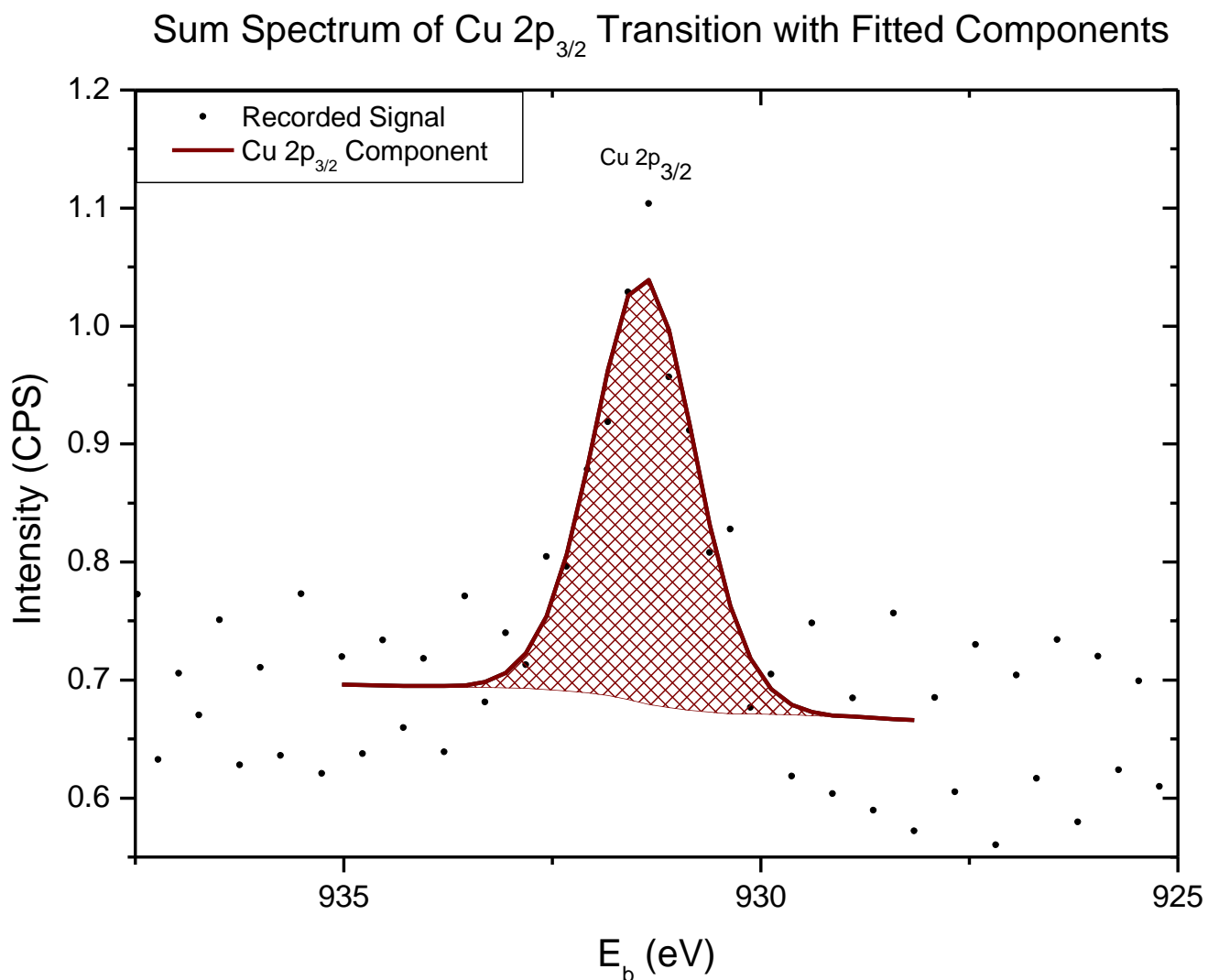


Figure 6.12: Sum spectrum from all image pixels for measurement of the Cu $2p_{3/2}$ transition with the component fitted.

The spectra originating from the Cu 2p transition image were the most simple to analyze, as the snapshot region only contained a single peak and survey spectra showed low background for the other elements on the sample.

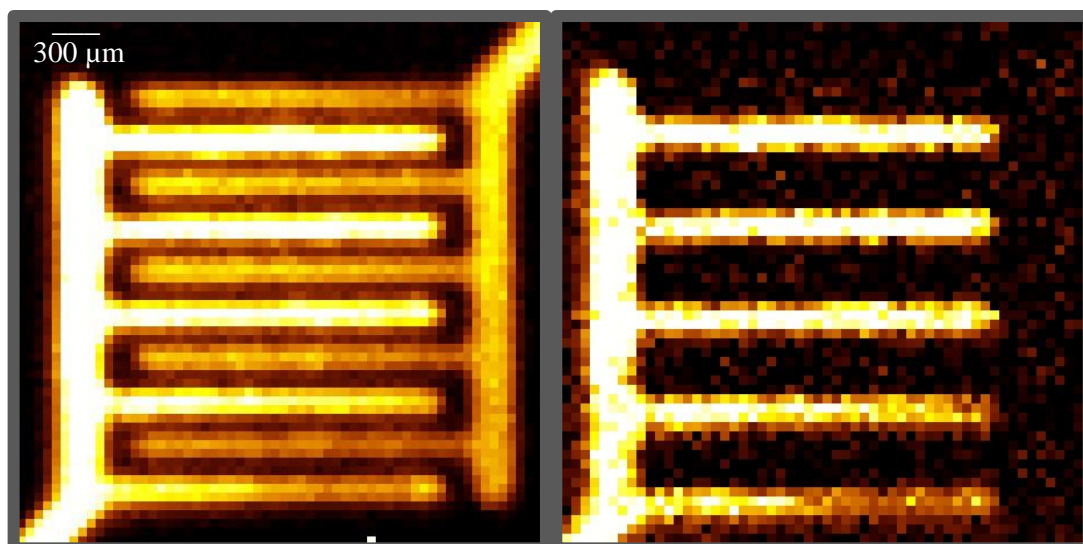


Figure 6.13: Unprocessed image vs component fitted image for Cu 2p transition.

The figure above shows the unprocessed image on the left and the Cu 2p component fitted image on the right. Autoscaling colors the pixel with the lowest integrated spectral area black, and the highest integrated spectral area white. Thus, in the raw image, the lowest intensity is present for the Al_2O_3 substrate, with an intermediate contrast present for the Pt electrode fingers. Fitting the Cu 2p component to all spectra and subtracting background prevents the Pt fingers from appearing. However, some lower intensity pixels at locations along the Pt fingers (colored dark orange) appear due to random noise occurring at the same energy of the Cu 2p component, resulting in small erroneous components being fitted.

Moreover, in this image we see a less intense Cu signal originating from the lower two fingers when compared to the upper three fingers. This is best explained by the differential flux from the X-ray source; since the sample is tilted to face the analyzer, the sample is tilted away from the sample

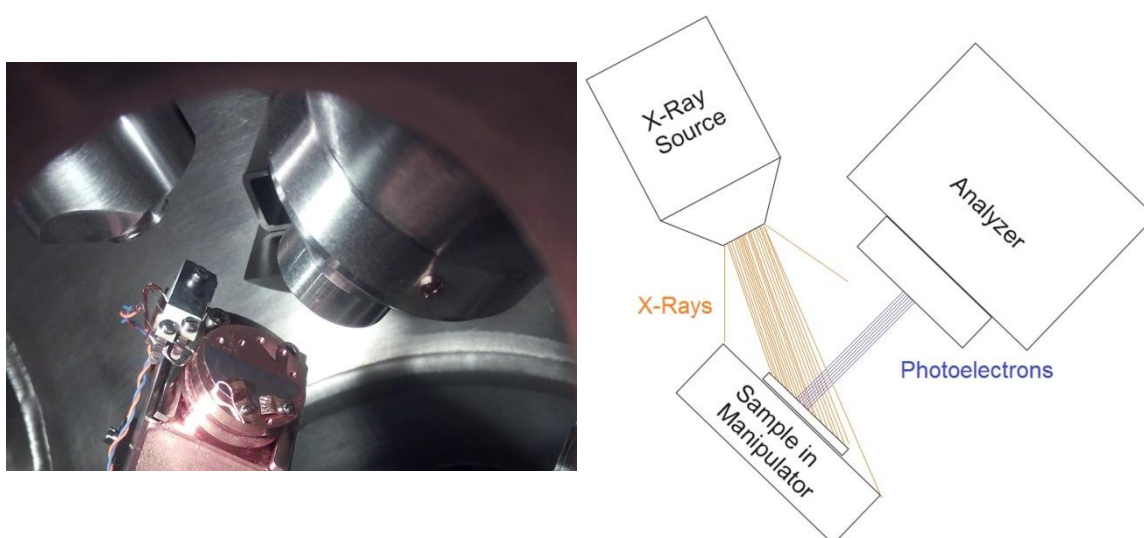


Figure 6.14: Image depicting the orientation of the X-ray source, analyzer, and sample during measurement (image of the Ta knife edge during measurement is on the left, schematic diagram on the right).

As we can see in the above schematic diagram, the X-ray flux, which is inversely proportional to the distance from the source, is lower at the bottom of the sample. This provides an explanation for the lower intensity seen in the image for the lower electrode fingers.

Sum Spectrum of Pt $4f_{7/2}$ Transition with Fitted Components

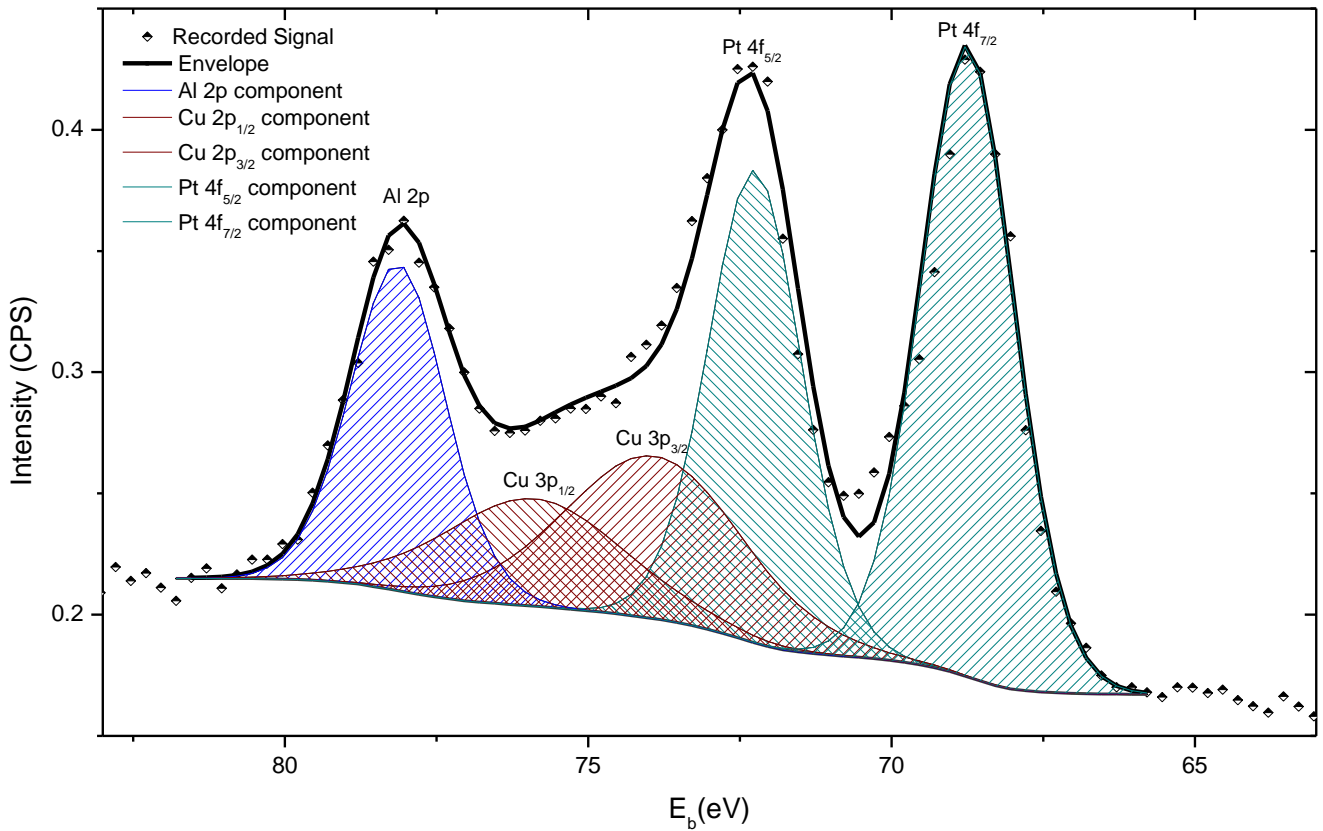


Figure 6.15: Sum spectrum from all image pixels for measurement of the Pt 4f transition, which also includes Cu 3p and Al 2p transitions. Components are fitted for these transitions.

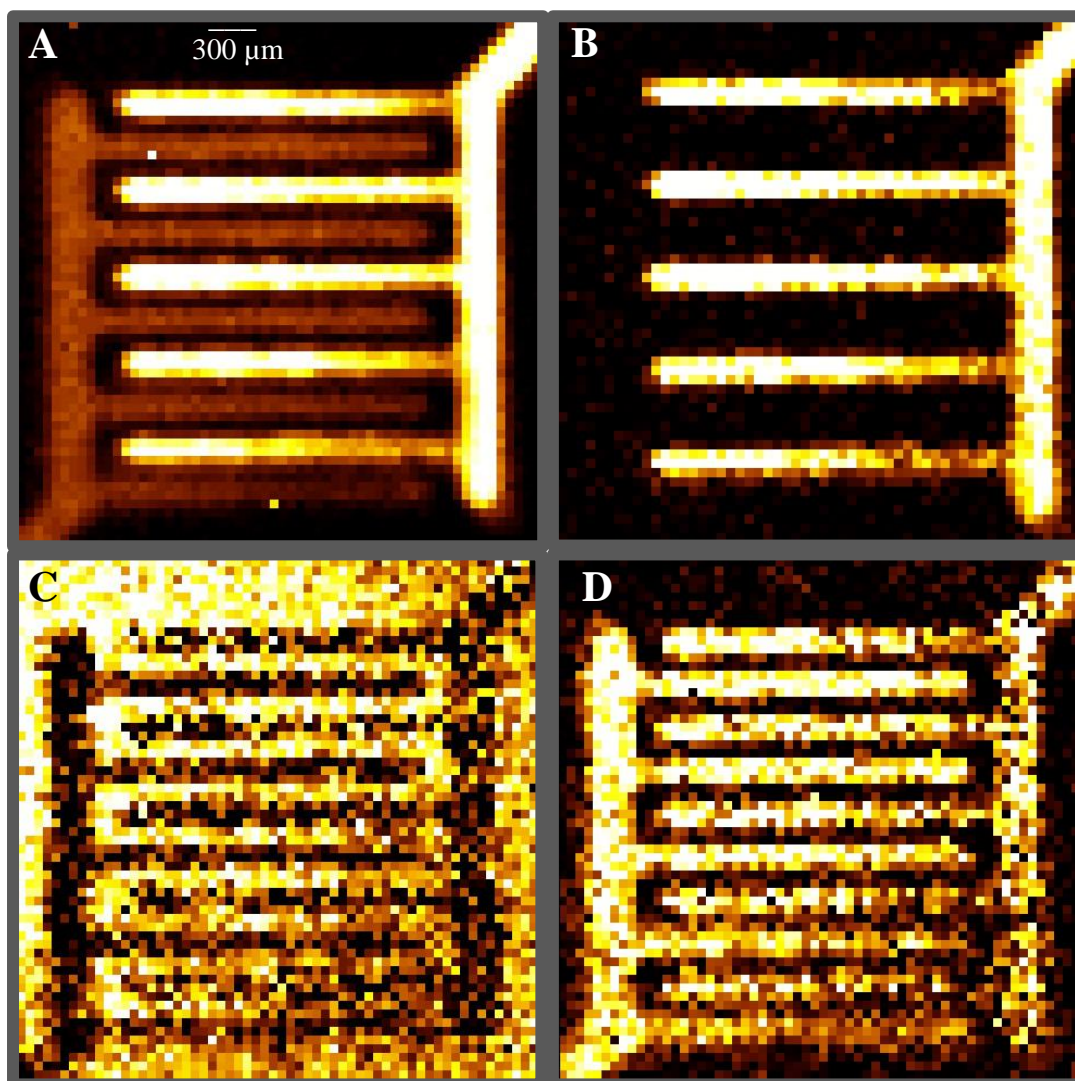


Figure 6.16: Images generated from Pt 4f image measurement. **A** represents the raw data without background subtraction, **B** represents the Pt 4f_{7/2} component, **C** represents the Al 2p component, and **D** represents the Cu 3p_{3/2} component. Component fittings all utilize background subtraction.

The spectra from image taken at the Pt 4f transition are more complicated for component fittings, as they contain overlapping transitions. However, the Pt 4f_{7/2} component contains very little overlap, and is thus fairly easy to fit. Similarly, the charging that occurs in the Al₂O₃ shifts the Al 2p peak 5 eV to the left, making it easier to resolve from the Cu 3p and Pt 4f_{5/2} peaks. Three components were fitted to generate images from this measurement, representing each element found in the spectrum above. Doublet peaks are fixed to each other, so it is only necessary to generate one image for Cu 3p and Pt 4f. This energy region is unique because it contains transitions from all the elements of interest. The Pt image allows for the electrode fingers to be clearly seen, and the Al image resolves the substrate fairly well. However, the Cu image erroneously displays high intensity on the Pt fingers as well as the Cu fingers. This occurs due to problems with component fittings for the overlapping components (Pt 4f_{5/2}, Cu 3p_{3/2}, Cu 3p_{1/2}) in the center of the spectrum.

The Pt component fitted image is evidence of the surface sensitivity of the system. Based on the deposition calculations and investigation of the sample with SEM, it is known that 100 nm below the Cu deposition there are Pt electrode fingers. However, no Pt signal is measured through the Cu deposition layer.

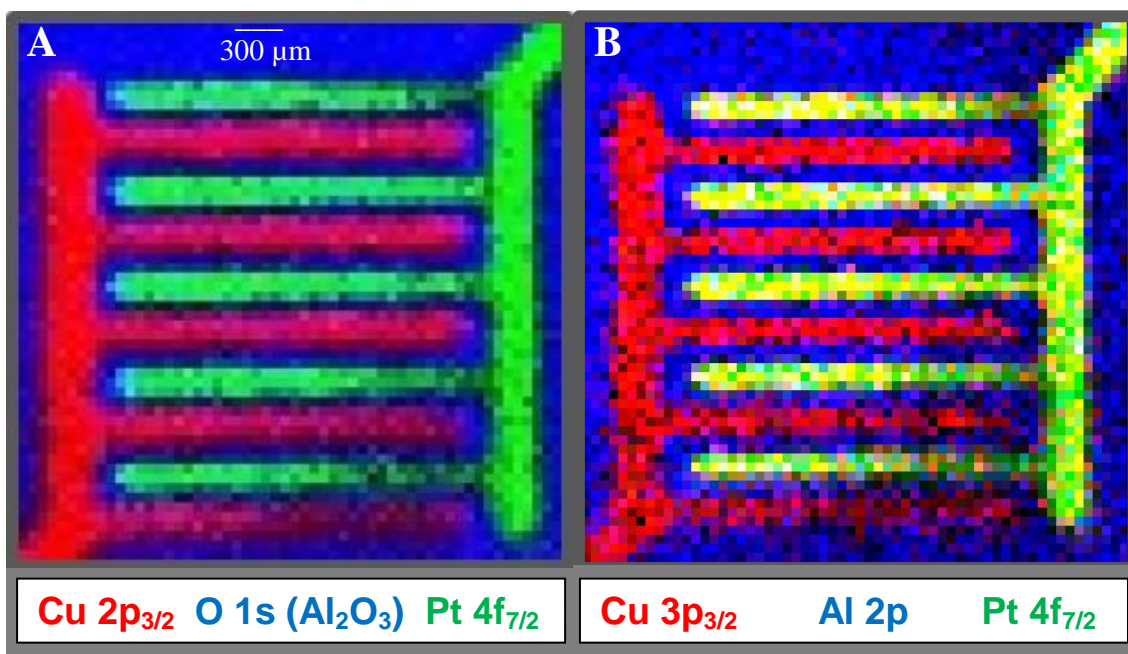


Figure 6.17: Images generated by overlaying component fittings. Image A represents the Pt 4f_{7/2}, Cu 2p_{3/2}, and O 1s (Al₂O₃) components recorded in separate measurements. Image B represents the components from the Pt 4f image measurement: Al 2p, Cu 3p_{3/2}, and Pt 4f_{7/2} components were overlaid.

The images above show the results of overlaying individual components to form a colored image, with red, green and blue representing separate components. The best result is obtained by overlaying one component from each measurement, as visible in the image at left. However, as seen in the previous sum spectrum, three elements can be obtained in a single measurement and their components can be overlaid to achieve a similar result. However, due to the poor component fitting for the Cu 3p transition, pixels corresponding to the platinum fingers in the right image contain both Cu 3p and Pt 4f, causing them to appear yellow.

6.2.2 Line Scans

Since the IDE sample contains regular features in the horizontal direction, vertical line scans are a useful way to study the surface features of the sample and the analyzer's ability to resolve them.

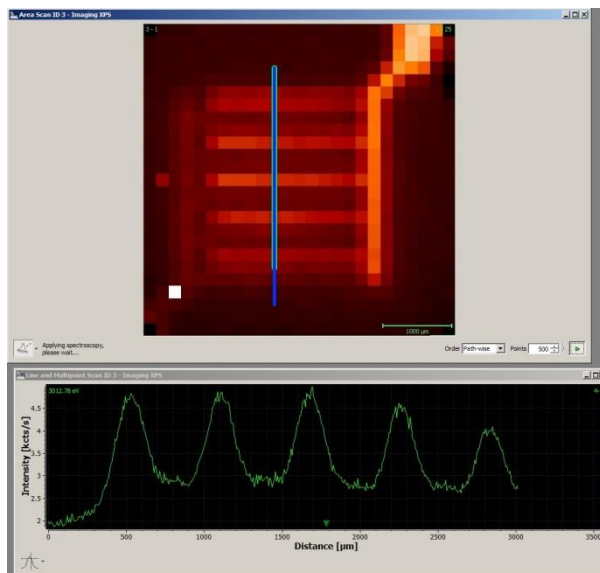


Figure 6.18: Location of line scans across the sample, as viewed in MATRIX software.

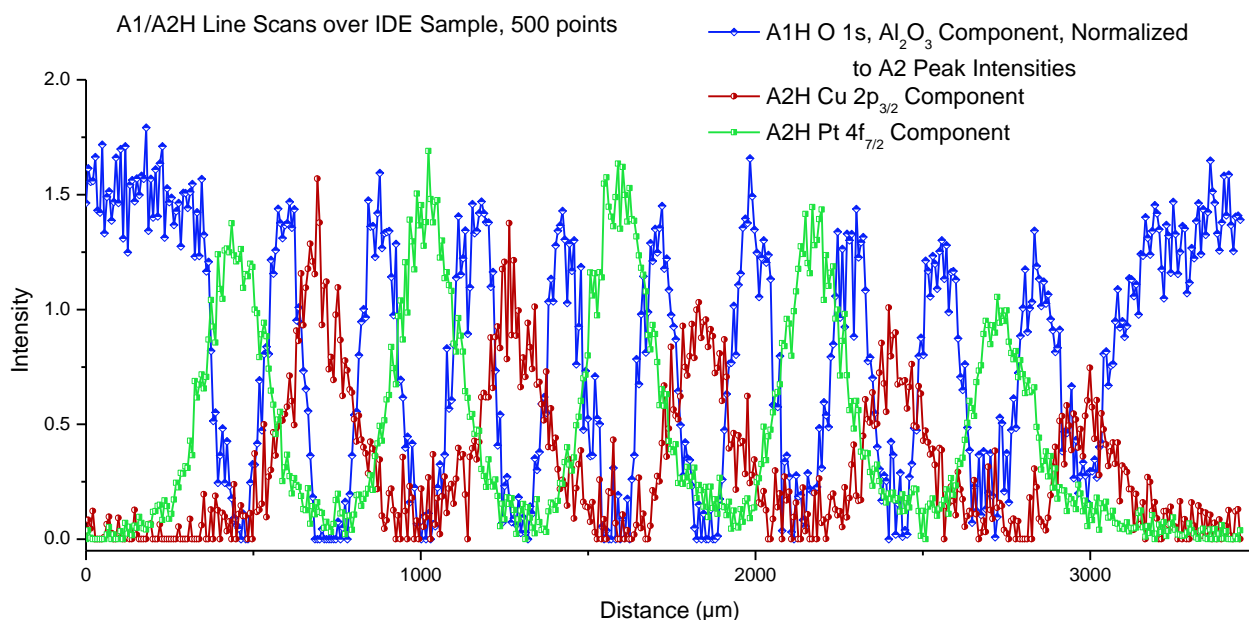


Figure 6: Line scan measurements, with Pt 4f_{7/2}, Cu 2p_{3/2}, and O 1s (Al₂O₃) component fittings overlaid.

This line scan series was taken vertically across the entire sample, with 500 points measured across a 3500 µm distance for Pt 4f, Cu 2p, and O 1s transitions. When measuring Cu 2p and Pt 4f transitions, the lateral resolution of the A2H aperture setting was sufficient because of the large distance between alternating fingers. However, A1H

setting was preferable for the O 1s (Al_2O_3) measurement, as there is a shorter distance between substrates occurring between electrode fingers. Once again, as seen in the images, there is a lower component intensity measured for the electrode fingers located at the bottom of the sample due to a lower amount of received X-ray flux.

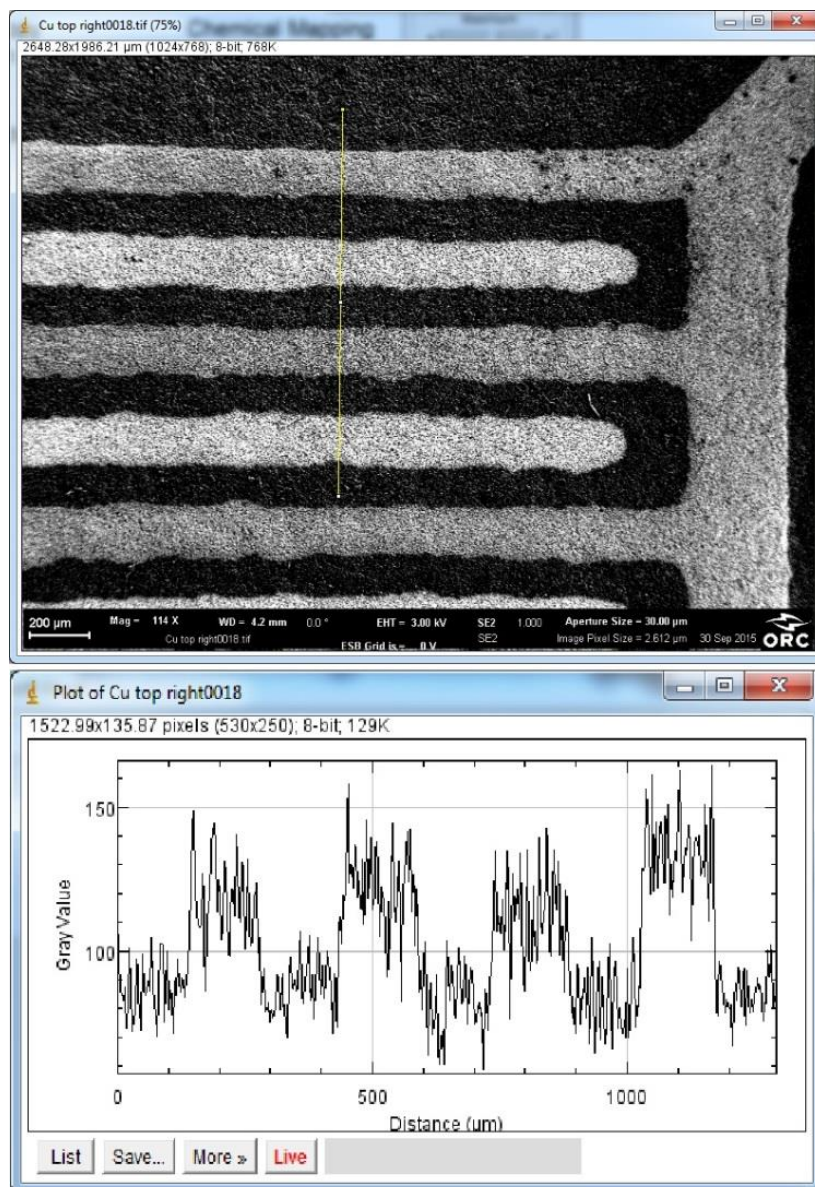


Figure 6.20: SEM Image with the profile plotted in ImageJ software.

Further line scan studies of a shorter region allowed the profiles from XPS line scans to be compared with SEM images of the electrode fingers.

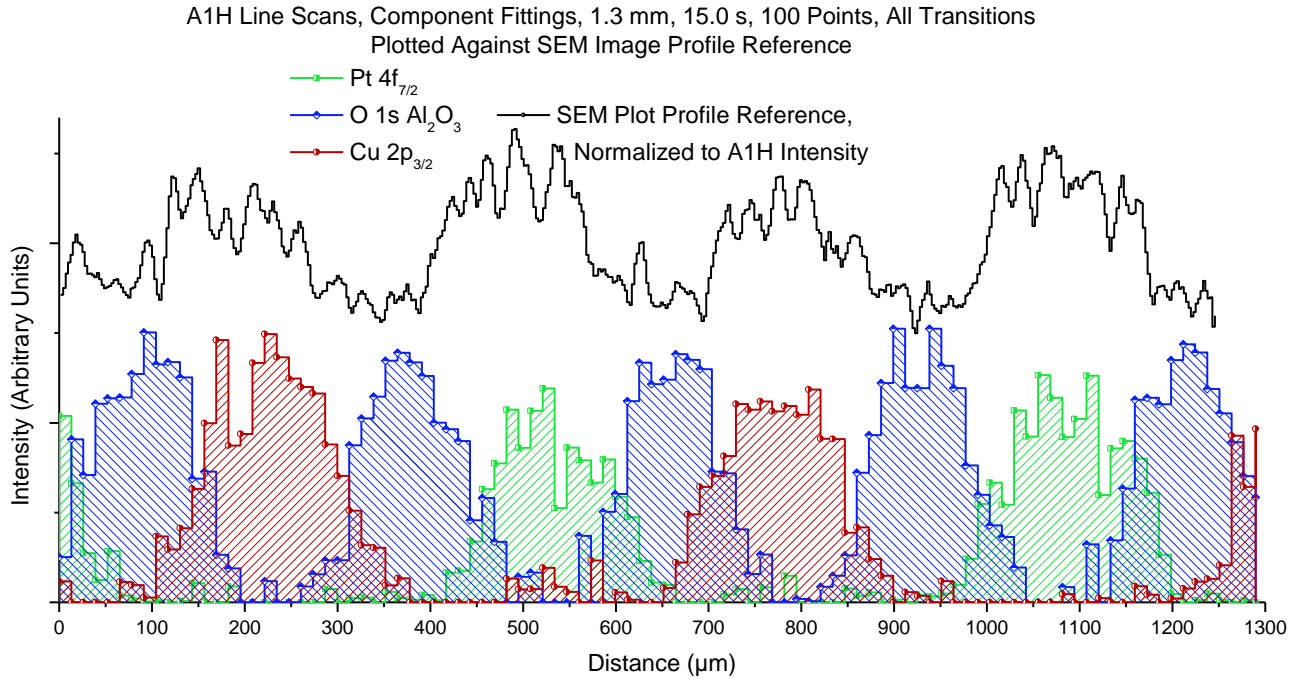


Figure 6.7: *Pt 4f_{7/2}, Cu 2p_{3/2}, and O 1s (Al₂O₃) component fitted line scans plotted against an SEM image profile plot.*

The shorter line scan contains four electrode fingers. When compared to the SEM profile plot, the Pt and Cu line scan peaks are congruent with the SEM image. Thus, the line scans are accurate in their scale while also providing chemical mapping of the surface.

6.2.3 Future Studies of Interdigitated Electrodes

Were more measurements taken of this sample, it would be useful to repeat measurements of the O 1s and Pt 4f transitions, applying a bias voltage to the electrodes. Applying a set voltage would shift peaks away by the determined energy amount, so it could be possible to distinguish the two metal oxides from each other, and also separate the overlapping Cu 3p and Pt 4f transitions. Either of these measurements would allow a quality image of the sample to be generated from a single image measurement.

6.3 Imaging Parameter Optimization

When discussing imaging parameters, it becomes useful to define a term that's relevant to selecting the imaging area and the points to be used. In this discussion, the term Lateral Resolution: Pixel Side Length Ratio (LRPSLR) will be used.

When the dwell time for the imaging measurement has been found sufficiently reliable, it is best to use at least an LRPSLR of 1. LRPSLRs lower than 1 will result in large percentages of the surface not being analyzed. Thus, using A2 aperture is often preferable to using A1 with an LRPSLR lower than 1. Further description of imaging parameter optimization is presented with examples in the appendices (Appendix E).

6.4 Line Scan Parameter Optimization

As with LRPSLR for images, an equivalent term for line scans is Lateral Resolution: Point-to-Point Ratio (LRPPR). As with imaging, when defining parameters for a line scan, it's first important to use a dwell time that is sufficiently long to generate reproducible snapshot spectra. After that, the LRPPR may be increased depending on the dimensions of the surface and the measurement time that can be invested. For A1H line scans, LRPPR of 4-8 is a good measure, while for A2 a higher LRPPR may be desirable. A2 aperture images and line scans can be orders of magnitude less time consuming, so it's best to begin with A2 then use A1 aperture as necessary. Examples of line scans can be viewed in the appendices (Appendix F).

6.5 Quantification of Minuscule Surface Features

With some understanding of the analysis spot and LRPSLR, then some geometrical inferences, it is possible to estimate the size of features which are smaller than the resolution limit of the analyzer. Specifically, if the surface is homogenous with occasional defects or island structures, it may be possible to detect them and estimate their size. This technique is described with images in the appendices (Appendix G).

7. CONCLUSIONS

The first objective of this work was to assess the capabilities of the analysis system quantitatively. Measurements of silver foil references were conducted using the different aperture and magnification options, and also measured with different pass energies. The FWHM calculations are particularly interesting for the quantification of analysis parameters, because they are indicative of the energy resolution. Results showed that increasing pass energy increased signal intensity at the expense of energy resolution. This trend is less pronounced in the smaller apertures.

Secondly, a knife-edge sample, prepared by mounting tantalum foil to the surface of a copper sample holder, was measured to quantify the resolution of the analyzer's deflector lens system. When measuring a line scan across the knife edge, calculation of the 16%-84% intensity lateral distance defines both the lateral resolution and the analysis spot size. Measured resolutions were found to be an improvement upon those presented in the analyzer manual.

The IDE sample was chosen as a case study for evaluation of the analyzer's imaging mode. Electrochemical methods were used to deposit copper of a known thickness to one electrode of the IDE. The sample was then studied with XPS. Images and line scans showed no platinum signal on the electrode fingers with thin Cu deposition layer, providing evidence for the surface sensitivity of the system. Component images from three separate measurements were overlaid to create a high quality image representing one element with each color. Dimensions of the images and line scans were compared to SEM images and showed high spatial accuracy. Efficiency and energy resolution for spectra obtained through imaging was demonstrated by fitting three separate elemental components from a single measurement to create a high quality image of the sample.

In the future, measurements of IDE samples could be made more efficient and accurate by utilizing a bias voltage on the electrodes to shift peaks of studied species away on the spectra, where they could be analyzed without interference from signals originating from other species. Planning such a measurement carefully would allow a measurement of multiple elemental transitions in a single measurement cycle.

While the IDE was a useful sample to demonstrate the capabilities of the analyzer, it was also vital to draw conclusions from these measurements regarding future measurements. Parameter optimization of images and line scans was presented. Furthermore, a theoretical technique was devised to detect and quantify surface features whose dimensions are below the resolution limit of the analyzer.

REFERENCES

- [1] Nanomaterials Imaging Techniques, Surface Studies, and Applications By Olena Fesenko, Leonid Yatsenko, Mikhaylo Brodin
- [2] Lecture Notes on Surface Science. Hofmann, P. Århus University. October 5, 2005.
- [3] The Handbook of Surface Imaging and Visualization. Hubbard, A.T. University of Cincinnati. 1995.
- [4] Mass Spectrometry Imaging under Ambient Conditions. Wu, C. Dill, A.L., Eberlin, L.S., Cooks, R.G., Ifa, D.R. *Mass Spectrum Rev.* 2013 May; 32(3): 218-243.
- [5] Surface Science: Foundations of Catalysis and Nanoscience. Kolasinski, K.W. 2nd Ed. 2008. John Wiley & Sons Ltd.: U.K.
- [6] Mass Spectrometry Imaging with High Resolution in Mass and Space. Römpp, A. Spengler, B. *Histochem Chem Biol.* 2013 139:759-783.
- [7] High-Resolution Near-Field Raman Microscopy of Single-Walled Carbon Nanotubes. Hartschuh, A., Sanchez, E.J., Xie, X.S., Novotny, L. *Physical Review Letters.* 4 March 2003. 90, 095503.
- [8] Understanding amyloid aggregation by statistical analysis of atomic force microscopy images. Adamcik, J., Jung, J.M., Flakowski, J., De Los Rios, P., Dietler, G., Mezzenga, R. *Nature Nanotechnology Letters.* 11 April 2010. 10.1038/NNANO.2010.59.
- [9] Images of Adsorbates with the Scanning Tunneling Microscope: Theoretical Approaches to the Contrast Mechanism. Sautet, P. *Chemical Review.* 1997. 97, 1097-1116.
- [10] Local density of states from spectroscopic scanning-tunneling-microscope images: Ag(111). Li, J., Schneider, W.D., Berndt, R. *Physical Review B.* 15 September 1997. Volume 56, Number 12.
- [11] Molecular beam epitaxy of organic films investigated by high resolution low energy electron diffraction (SPA-LEED): 3,4,9,10-perylenetetracarboxylicacid-dianhydride (PTCDA) on Ag(1 1 1). Kilian, L., Umbach, E., Sokolowski, M. *Surface Science.* Volume 573, Issue 3, 20 December 2004. Pages 359-378.
- [12] Morphological and chemical properties of black carbon in physical soil fractions as revealed by scanning electron microscopy and energy-dispersive X-ray spec-

- troscopy. Brodowski, S., Amelung, W., Haumaier, L., Abetz, C., Zech, W. *Geoderma*. Volume 128, Issues 1–2, September 2005, Pages 116–129.
- [13] Auger Electron Spectroscopy (AES) and Scanning Auger Microscopy (SAM). Scudiero, L. Washington State University.
- [14] Scanning Electron Microscopy: Physics of Image Formation and Microanalysis. Reimer, L. 1985. Springer-Verlag: Germany.
- [15] Transmission Electron Microscopy: Physics of Image Formation and Microanalysis. Reimer, L. 4th ed. 1997. Springer-Verlag: Germany.
- [16] Compensation of charging in X-PEEM: a successful test on mineral inclusions in 4.4 Ga old zircon. De Stasio, G. Frazer, B., Gilbert, B., Richter, K.L., Valley, J.W. *Ultramicroscopy*. Volume 98, Issue 1, December 2003, Page 57-62.
- [17] Sea urchin shaped carbon nanostructured materials: carbon nanotubes immobilized on hollow carbon spheres. Piao, Y., An, K., Kim, J., Yu, T., Hyeon, T. *Journal of Materials Chemistry*. Issue 29, 2006.
- [18] Hertz, H. *Annalen der Physik* 267, 983–1000 (1887)
- [19] Einstein, A. *Annalen der Physik* 17, 132–148 (1905)
- [20] The XPS and AES Methods for Surface Analysis in Material Science. Chorkendorff, I. 1994. Technical University of Denmark.
- [21] Surface Analysis by Auger and X-ray Photoelectron Spectroscopy. Briggs, D., Grant, J.T. 2003. IM Publications and SurfaceSpectra Limited: U.K.
- [22] Handbook of X-ray Photoelectron Spectroscopy. Moulder, J.F., Stickle, W.F., Sobol, P.E., Bomben, K.D. 1992. Pelkin-Elmer Corporation: USA.
- [23] ARGUS Spectrometer User Guide. Version 1.1. Omicron NanoTechnology. Taunusstein, Germany. 23 January 2013.
- [24] DAR400/400HP with X-ray 558 Control. Version 1.0. Oxford Instruments. Abingdon, Oxfordshire, England. 21 May 2014.
- [25] nXSA Scroll Pump Instruction Manual. A735-01-880 Issue B Original. © Edwards Limited. 2013.
- [26] Turbo-V 81-M. Varian Vacuum Technologies. 87-900-983-01(A). 2006.
- [27] Titan™ Ion Pumps. Gamma Vacuum. Available:
<http://www.gammavacuum.com/index.php/theory-of-operation/>

- [28] Pump Classifications Technical Notes. Kurt J. Lesker Company. Available: http://www.lesker.com/newweb/vacuum_pumps/vacuumpumps_technicalnotes_1.cfm
- [29] Ion Bombardment Gun Model 981-2043 Instruction Manual. Intevac MBE Equipment Division.
- [30] Diagram explaining the sputtering process. Available: http://www.oxford-vacuum.com/background/thin_film/sputtering.htm
- [31] Planar Interdigitated Electrodes Data Sheet. Synkera Technologies, Inc. 2011. United States: Colorado.
- [32] Theory and Practice of Metal Electrodeposition. Gamburg, Y.D., Zangari, G. Springer Science & Business Media. 2011.
- [33] MATRIX Application Manual for XPS. Version 1.0. Omicron NanoTechnology. 26 October 2012.
- [34] Vernissage Result File Access & Export. Version 2.2. Omicron NanoTechnology. 31 October 2014.

APPENDIX A: SAMPLE LOADING PROTOCOL

Prior to opening the microchamber flange and loading the sample, protocol must be followed to avoid pressurization of other chambers and prevent damage to the system. This protocol is subject to frequent modifications, as alterations are made to the system. A schematic diagram of the gas lines in the system, and the step-by-step instructions for loading a sample are shown below.

- Close V20 valve
- Close intermediate valve
- Close N₂, Ar valves
- Open EX05
- Close V7
- Check microchamber wobble stick to make sure it has not caught/stuck
- Close safety valve located before N₂
- Open N₂ regulator outlet valve to release N₂ in lines and check for N₂ gauge response, close it
- Open N₂ main cylinder valve a half turn
- Open N₂ regulator control valve until gauge reads just over 0.5
- Open N₂ stop valve, to pressurize lines up to V5
- Slowly open N₂ valve, pressurizing microchamber to 7.4 (hundreds of torrs). This should take a few minutes otherwise it's pressurizing too quickly.
- Close N₂ valve
- Close EX05
- Check rear microchamber wobble stick, to make sure it's properly situated
- Equip nitrile gloves
- Clean wrench, torque wrench, and needle nose pliers with ethanol
- Clean top surface of flange with ethanol to prevent particles from entering the microchamber when it is opened
- Unbolt microchamber flange using wrench. Set aside bolts with washers and plate nuts. (Plate nuts can be dropped if care is not taken during this step)
- Place flange and copper gasket in aluminum foil to limit particle accumulation; cover microchamber flange with aluminum foil.
- If unloading a sample, use needle nose pliers to rotate the sample and grip it from the bottom right flat corner, guiding the sample holder out of the fork, moving the sample to the left. Lift the sample above the fork and bring it over the fork and out of the chamber. Set aside

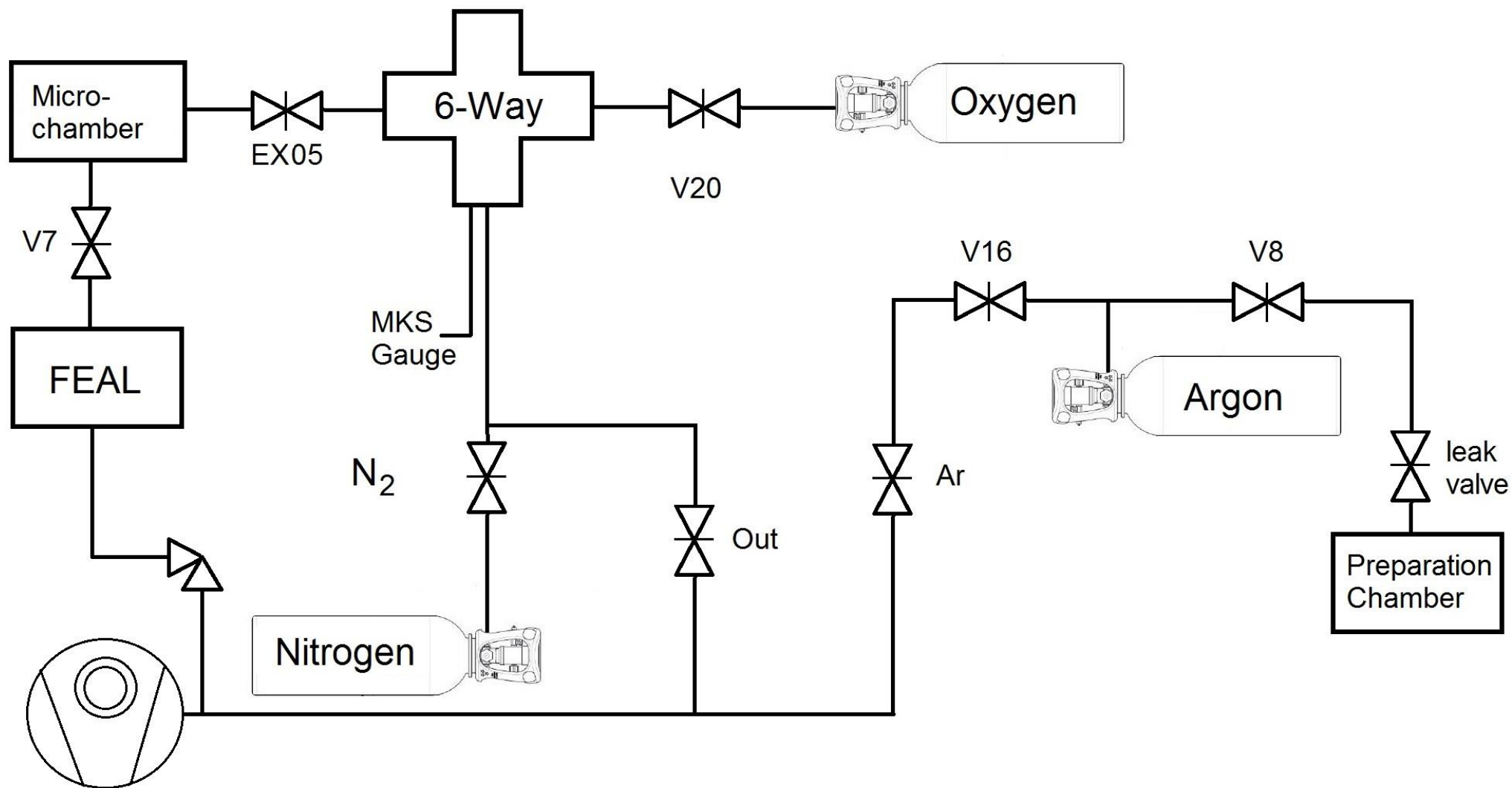


Figure A1: Labeled schematic diagram depicting gas lines.

- If loading a sample, use needle nose pliers to grip the sample holder securely from the right flat corner, with the sample held diagonally. Guide the sample holder through the flange and over the fork, then moving it left and sliding it onto the fork at the sample holder's upper groove. This allows the sample to be moved into the FEAL chamber later, engaging the sample holder with the FEAL wobble stick at the lower groove. Rotate the sample so that the thermocouple faces left to prevent thermocouple wires from being bent when moved to the FEAL chamber (it is usually bent at the Cu gasket of the gate valve)
- If copper gasket is worn, clean a new gasket with ethanol. Install curved surface towards the microchamber (this side is less likely to become stuck, so always faces the more valuable component), with the flat surface facing the flange window.
- Attach the flange back onto the microchamber, hand tighten bolts individually with plate nuts in place. Ensure the copper gasket has not fallen from its correct position during this step
- Use the torque wrench to tighten the bolts. Begin with 8 N·m, and tighten all bolts, using a sequence of tightening opposite bolts as to not unequally stress the copper gasket. Increase the torque wrench setting by increments of 2 N·m, until 14 N·m is reached for a new copper gasket. If the gasket has been used once, increase to 15 N·m. If used twice, increase to 16 N·m. If the gasket has been used three times, it can be replaced with a new gasket as it is no longer able to maintain a quality vacuum in the microchamber.
- Open EX05 valve
- Close turbo backline valve
- Turn off turbo-molecular pump
- Open center valve to allow pressure to flow into the turbo-molecular pump and slow its rotation. This should be done very slowly, while listening to the frequency of the turbo-molecular pump rotation. If done too quickly, a jarring sound will alert you that it has been pressurized too quickly; this can cause damage to the turbo-molecular pump hardware.
- When turbo-molecular pump has stopped, find a position so that the rear microchamber wobble stick can be held during evacuation, while viewing through the front microchamber flange that has just been opened. Hold it in place in a center position, so that it's not touching the sides of the chamber. If not restrained, depressurization can propel the wobble stick into the sample holder, damaging the microchamber fork or the wobble stick.
- Turn on the turbo-molecular pump, allowing it to depressurize the microchamber by opening the backline valve.
- Close N₂: first close the side valve, then the N₂ tank, then leave the N₂ dial loose.
- Allow half an hour for microchamber pressure to pump back to normal.

- Open the gate to the FEAL chamber
- Move the sample to the FEAL chamber using the FEAL wobble stick carefully as to not drop the sample.
- Close gate to FEAL chamber, checking to ensure the wobble stick has not been left under the gate.
- Pump N₂ lines by opening them slowly, without allowing pressure to exceed 6 – 1
- After a few hours, open V20 and Ar valve.

APPENDIX B: SAMPLE CLEANING VIA ION BOMBARDMENT

When uniform samples contain surface contamination and a clean surface is critical, ion sputtering is used. Clean Ar gas is pumped to the ion bombardment gun where it is ionized. The Ar atoms are accelerated to bombard the sample. This removes surface oxides and other contaminants, yet leaves the surface pitted with some Ar contamination.

- Move sample to sputtering place
- Check thermocouple connections using the thermocouple feedthrough pins located beneath the preparation chamber; resistance should measure ∞ when connected to ground, 10-30 Ω
- Attach clips underneath pins to connect to the Ion Gun controller. This allows target current to be monitored via thermocouple wires
- Remove screw from ion bombardment gun, fix magnet, align and mount with the screw
- Close Out valve as to not pressurize the microchamber with Ar
- Flush Ar lines, pumping away residual gas
- Monitor backing pressure, turbo-molecular pump may react to pressure increase
- Close V16, open Ar main cylinder valve, Ar should flow up to V8, open V8 to flush final portion of lines
- Flush lines 2-3 times to ensure uncontaminated Ar
- Check all valves and gates; gate valves to preparation chamber should be closed
- Lower multi-gauge current from 4.00 mA to 0.10 mA
- Carefully dial Ar regulator control valve so that pressure reads $\sim 3 \times 10^{-6}$ mbar
- Make sure beam energy knob is turned to zero before turning on gun control
- Turn on ISE5 Gun Control, tune beam energy (generally 0.70 or 1.00 keV)
- Monitor target current, which depends on the sample; to calculate appropriate current, lower Ar to maximize the target current. Appropriate sputtering current should be 80% of maximum current.
- Sputter sample for desired time, 5-20 minutes, check focus and position (ion beam is visible in the darkness)
- Tune down beam energy, shut off gun control
- Return Ar leak valve to original position, do not over rotate
- Close Ar: regulator outlet valve, then main cylinder valve, leave regulator control valve as is
- Open gate valves once pressure has dropped to 3×10^{-9} mbar

APPENDIX C: SAMPLE CLEANING VIA ANNEALING

Annealing is sometimes used to prepare a sample, and it is also used in sample cleaning. After sputtering a surface to remove surface contamination, the sample surface is left pitted and contaminated with some amounts of Ar. An annealing cycle often follows a sputtering cycle, to smooth the surface and remove Ar contamination. Annealing can be achieved at low temperatures using radiative heating, and at high temperatures using an electron beam. More specific instructions regarding electron beam heating are listed below:

- High annealing temperatures (up to 1100°K) are achieved using an electron beam; lower temperatures can be achieved through radiative heating
- With the sample in the manipulator, lift tungsten annealing filament so that it rises from the manipulator to fit underneath the sample holder
- To minimize degassing of the filament, a low filament current should be used with a high accelerating voltage
- attach high voltage connections: filament connected to negative connection, sample and ground attached to positive connection
- With the bias to the filament, electrons are accelerated towards the sample at 500-700 V
- Monitor annealing temperature using a Pyrometer, use correct emissivity factor to ensure correct temperature reading
- Anneal for the desired time (5-10 minutes)
- Allow heat to dissipate from the sample through the manipulator before sample transfer or measurement

APPENDIX D: COPPER DEPOSITION CALCULATIONS

Calculations of IDE Cu deposition thickness proceed according to equation 5.2:

$$\zeta = \frac{ItM}{\delta Fa\rho} \quad 5.2$$

Calculation of 2 nm Cu deposition on IDE sample:

$$\begin{aligned} &= \frac{2.7 \mu A \times 109 s \times 63.546 \frac{g}{mol}}{2 \times 96485.309 \frac{C}{mol} \times 0.054 cm^2 \times 8.96 \frac{g}{cm^3}} \times \frac{1 A}{10^6 \mu A} \times \frac{10^7 nm}{1 cm} \\ &= 2 nm \end{aligned}$$

Calculation of 100 nm Cu deposition on IDE sample (time and current are changed):

$$\begin{aligned} &= \frac{27.0 \mu A \times 544 s \times 63.546 \frac{g}{mol}}{2 \times 96485.309 \frac{C}{mol} \times 0.054 cm^2 \times 8.96 \frac{g}{cm^3}} \times \frac{1 A}{10^6 \mu A} \times \frac{10^7 nm}{1 cm} \\ &= 100 nm \end{aligned}$$

APPENDIX E: OPTIMIZING IMAGING PARAMETERS

When discussing imaging parameters, it becomes useful to define a term that's relevant to selecting the imaging area and the points to be used. In this discussion, the term Lateral Resolution: Pixel Side Length Ratio (LRPSLR) will be used.

When the dwell time for the imaging measurement has been found sufficiently reliable, it is best to use at least an LRPSLR of 1. LRPSLRs lower than 1 will result in large percentages of the surface not being analyzed. Thus, using A2 aperture is often preferable to using A1 with an LRPSLR lower than 1.

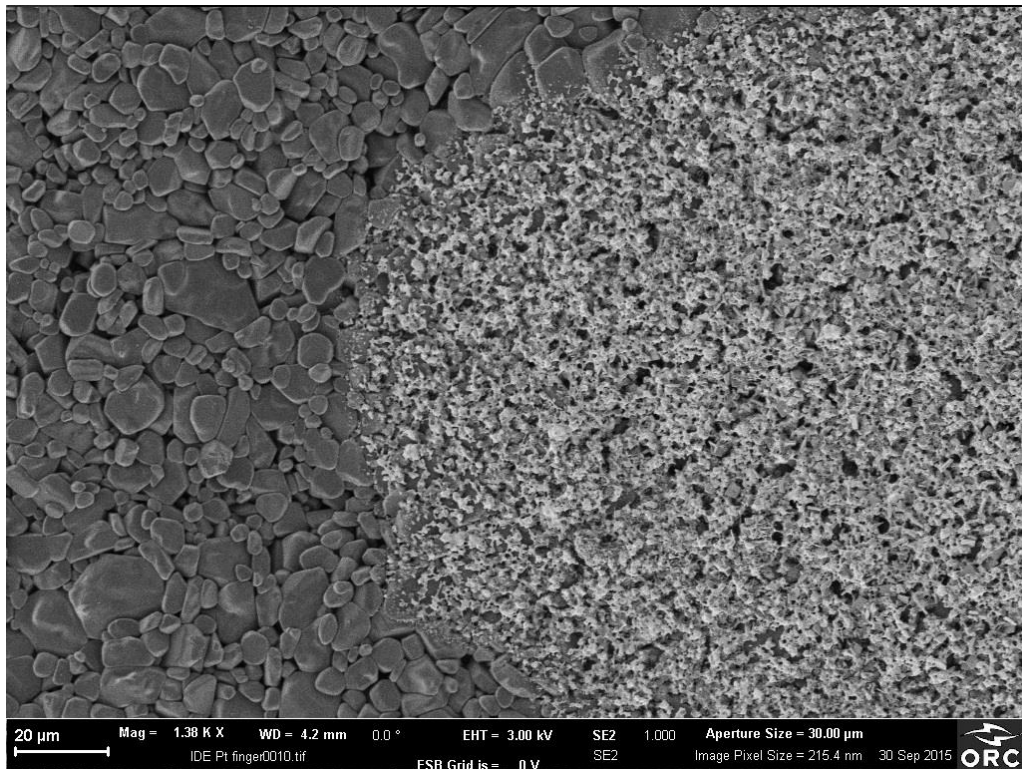


Figure E1: SEM image showing a platinum finger at high resolution. This is the feature which is measured in this section.

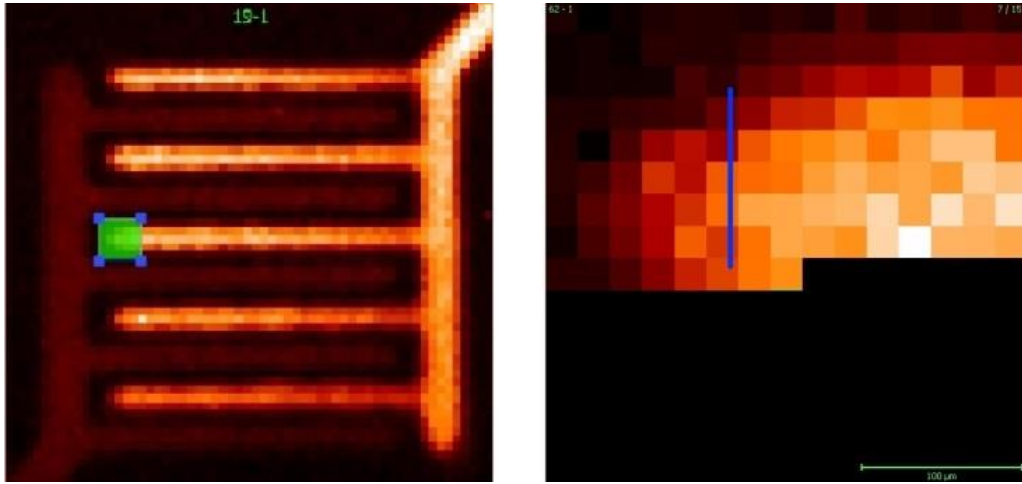


Figure E2: Measurement location of feature as viewed in MATRIX software.

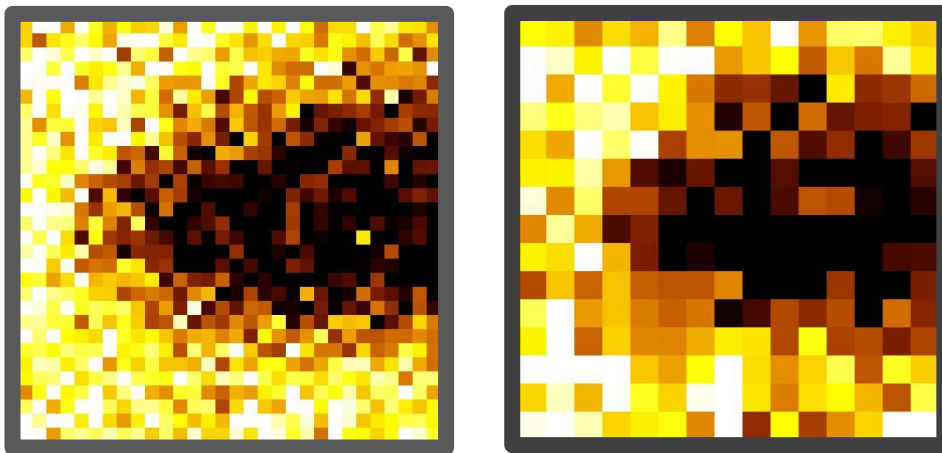


Figure E38: Images from AIH measurements of the O 1s transition with Al_2O_3 component fitting, with a dwell time of 3.0s. The left image was measured with 15x15 points (LRPSLR=2), while the right image was measured with 30x30 points (LRPSLR=4).

The above example shows that while there is some visible improvement when LRPSLR was increased from 2 to 4, but the same feature is very similarly recognizable. For high quality images, 2-4 is a good LRPSLR if the surface contains irregular features.

APPENDIX F: OPTIMIZING LINESCAN PARAMETERS

As with LRPSLR for images, an equivalent term for line scans is Lateral Resolution: Point-to-Point Ratio (LRPPR). As with imaging, when defining parameters for a line scan, it's first important to use a dwell time that is sufficiently long to generate reproducible snapshot spectra. After that, the LRPPR may be increased depending on the dimensions of the surface and the measurement time that can be invested. For A1H line scans, LRPPR of 4-8 is a good measure, while for A2 a higher LRPPR may be desirable. A2 aperture images and line scans can be orders of magnitude less time consuming, so it's best to begin with A2 then use A1 aperture as necessary.

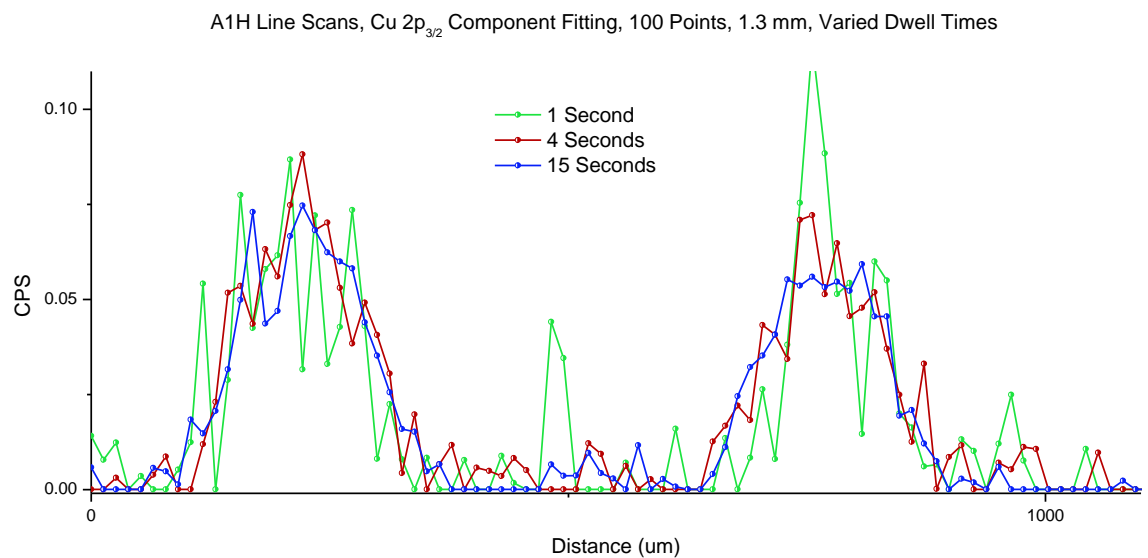


Figure F1: Effect of varying dwell time for A1H line scans. Reducing dwell time when counts are low significantly reduces reproducibility of measured data. Photoemission is a random process, so longer dwell time reduces the effect of the randomness of the physical phenomenon.

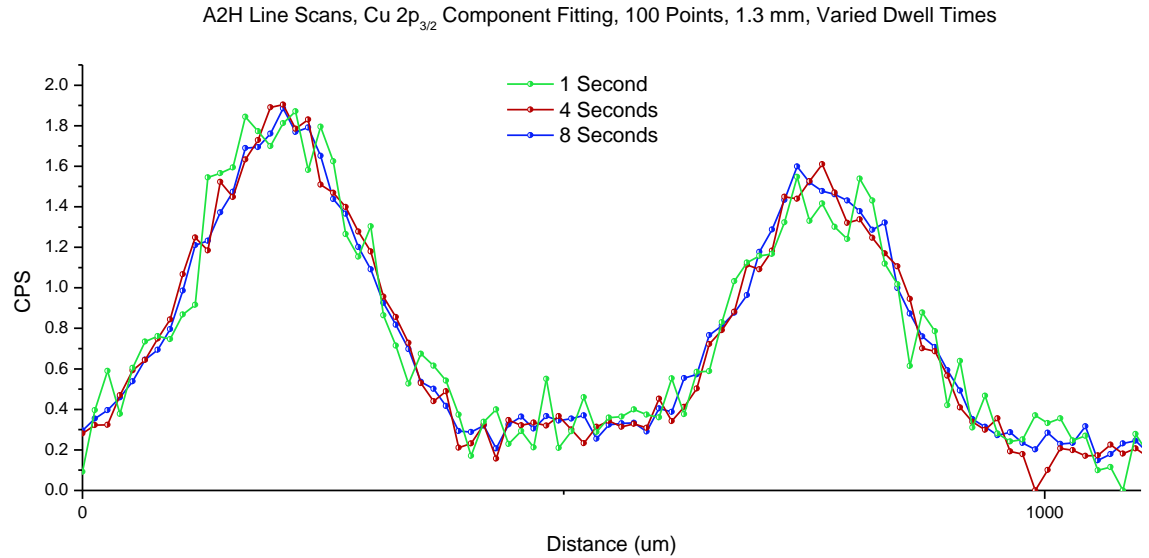


Figure F2: Effect of varying dwell time for A2H line scans. With the significantly higher count rates at A2H, longer dwell times have limited improvement over short ones.

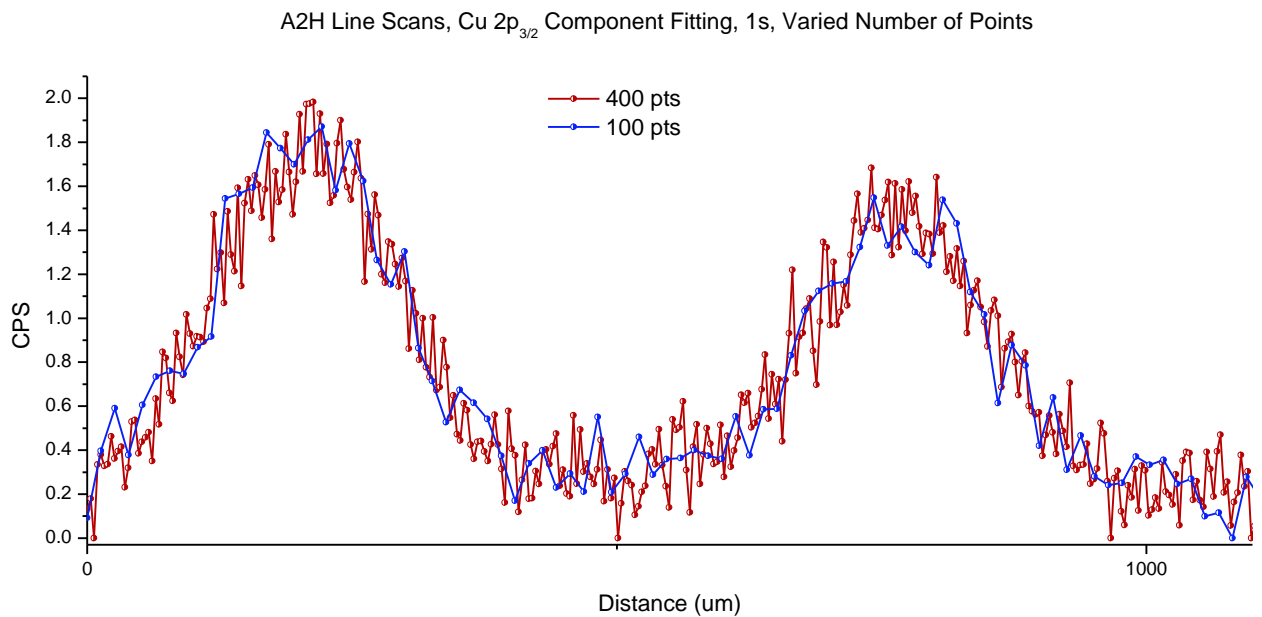


Figure F3: Effect of varying the number of points for A2H line scans. Since LRPPR is already so high for this measurement, there is only moderate improvement when increasing the number of points.

APPENDIX G: QUANTIFICATION OF MINUSCULE SURFACE FEATURES

With some understanding of the analysis spot and LRPSLR, then some geometrical inferences, it is possible to estimate the size of features which are smaller than the resolution limit of the analyzer. Specifically, if the surface is homogenous with occasional defects or island structures, it may be possible to detect them and estimate their size.

The figure on the following page explains how the analysis spots overlap to form pixel images with different LRPSLRs. LRPSLRs of 0.5, 1, 2, and 3 are depicted as examples, but there are many possibilities depending on the size of the imaged region and the number of points chosen.

For LRPSLRs of less than 1, much of the surface is not actually covered by analysis spot, since too few pixels have been chosen. Thus, if searching for smaller surface features such as islands, a LRPSLR of 1 or greater is necessary.

When increasing LRPSLR to ratios greater than 1, analysis spots start to overlap. Thus, when increasing LRPSLR past 1, it becomes impossible to detect an island in only a single pixel; it must also appear in other nearby pixels as well.

The following table indicates some of the possible pixel manifestations of islands and inferences about their size that can be made from them.

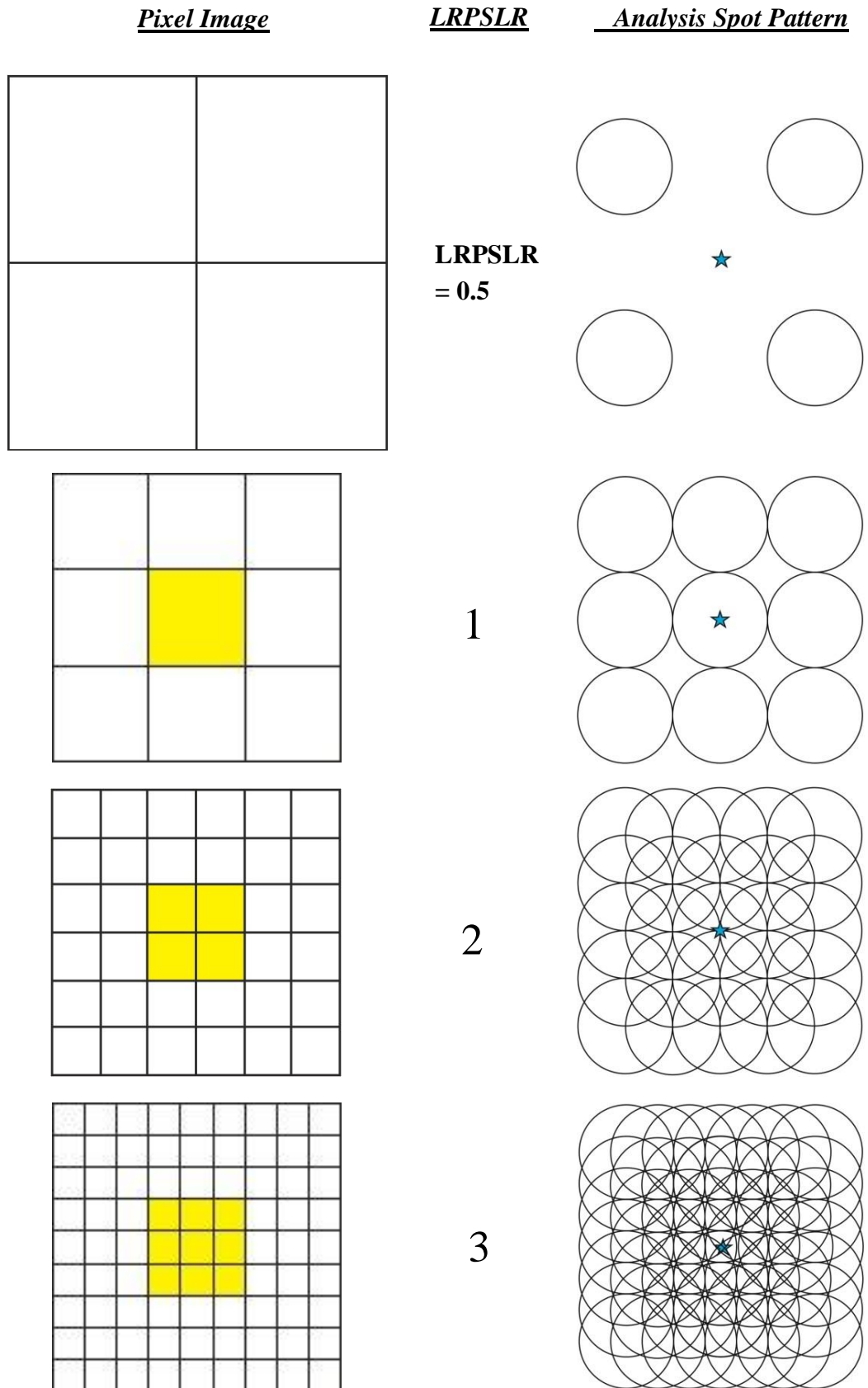
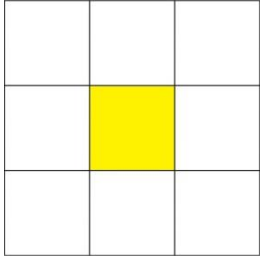
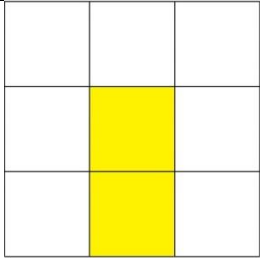
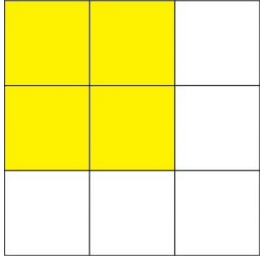
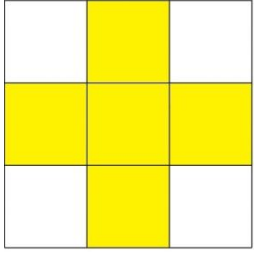
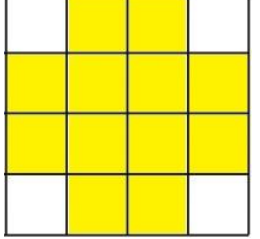


Figure G1: Pixel images compared with analysis spots for varied LRPSLRs.

Table G1: Estimated Sizes of Features based on LRPSLR and Pixel Pattern, for AIH measurements where lateral resolution = 40 μm .

Image	LRPSLR 1	LRPSLR 2	LRPSLR 3
	< 30 μm	<i>Not possible</i>	<i>Not possible</i>
	20 – 60 μm	<i>Not possible</i>	<i>Not possible</i>
	30 – 60 μm	< 10 μm	< 5 μm
	80 – 90 μm	< 20 μm	<i>Not possible</i>
	100 – 120 μm	80 – 90 μm	< 15 μm